1949

Nanoscale structural characteristics of polyvinyl alcohol – borosilicate hybrid aerogels and calcium alginate aerogels for potential biomedical applications

Thesis for the Degree of Doctor of Philosophy (PhD)

by **Zoltán Balogh**

Supervisors:
Dr. József Kalmár, Associate Professor
(University of Debrecen)
Dr. Zoltán Imre Dudás, Senior Research Fellow
(HUN-REN Centre for Energy Research)

UNIVERSITY OF DEBRECEN
Doctoral Council of Natural Sciences and Information Technology
Doctoral School of Chemistry
Debrecen, 2024.

Hereby I declare that I prepared this thesis within the Doctoral Council of Natural Sciences and Information Technology, ***Doctoral School of Chemistry****,* ***University of Debrecen*** *in order to obtain a PhD Degree in Natural Sciences at Debrecen University.*
The results published in the thesis are not reported in any other PhD theses.

Debrecen, 20. . . . . . ……

Zoltán Balogh

Hereby I confirm that ***Zoltán Balogh*** *conducted his studies with my supervision within the* ***K/2*** *Doctoral Program of the* ***Doctoral School of Chemistry between 2021 and 2024****. The independent studies and research work of the candidate significantly contributed to the results published in the thesis.*
I also declare that the results published in the thesis are not reported in any other theses.
I support the acceptance of the thesis.

Debrecen, 20.. . . . . . ……

Dr. József Kalmár

Hereby I confirm that ***Zoltán Balogh*** *conducted his studies with my supervision within the* ***K/2*** *Doctoral Program of the* ***Doctoral School of Chemistry between 2021 and 2024****. The independent studies and research work of the candidate significantly contributed to the results published in the thesis.*
I also declare that the results published in the thesis are not reported in any other theses.
I support the acceptance of the thesis.

Debrecen, 20.. . . . . . ……

Dr. Zoltán Imre Dudás

Nanoscale structural characteristics of polyvinyl alcohol – borosilicate hybrid aerogels and calcium alginate aerogels for potential biomedical applications

Dissertation submitted in partial fulfilment of the requirements for the doctoral (PhD) degree in Chemistry

Written by **Zoltán Balogh,** certified Chemical Engineer

Prepared in the framework of the Doctoral School of Chemistry of the University of Debrecen
(Coordination and Analytical Chemistry, program K/2)

Dissertation advisors: **Dr. József Kalmár**, Associate Professor
(University of Debrecen)

Dr. Zoltán Imre Dudás, Senior Research Fellow
(HUN-REN Centre for Energy Research)

The official opponents of the dissertation:

Dr. ....
Dr. ....

The evaluation committee:

chairperson:	Dr.	.....	.....
members:	Dr.	.....	.....
	Dr.	.....	.....
	Dr.	.....	.....
	Dr.	.....	.....

The date of the dissertation defense: …… 20…

Acknowledgements

I would like to extend my thanks to my supervisor, *Dr. József Kalmár*, for his guidance, professional help, and support throughout my university years.

I also wish to express my sincere gratitude to my other supervisor, *Dr. Zoltán Imre Dudás*, for his professional assistance, and support during my PhD studies. I am particularly thankful for the opportunity he provided to conduct my doctoral research in cooperation with the Department of Neutron Spectroscopy at the HUN-REN Centre for Energy Research.

Additionally, I am grateful to *Dr. Ákos Horváth* for allowing me to work at the Centre for Energy Research during my doctoral training.

I would like to express my sincere thanks to *Dr. Adél Len* for introducing me to the intricacies of small-angle neutron scattering and for always being available to help.

I would also like to thank *Dr. Cedric J. Gommes* for his teachings and work on modeling small-angle scattering curves, as well as his always helpful attitude.

I would like to thank *Prof. Dr. Attila Gáspár*, head of the department, for providing the opportunity to conduct my doctoral research and dissertation at the Department of Inorganic and Analytical Chemistry.

I also extend my gratitude to *Prof. Dr. István Fábián* for allowing me to be a member of the HUN-REN-DE Mechanisms of Complex Homogeneous and Heterogeneous Chemical Reactions Research Group and for supporting my research.

I am grateful to *Dr. Petra Herman* for the support she provided during my work and for conducting the elemental analysis measurements.

I also extend my gratitude to *Dr. Attila Forgács* for his support during my university years as a colleague and former supervisor.

I am thankful to *Dr. Krisztián Moldován* and *Dániel Pércsi* for their significant help as colleagues and friends.

Additionally, I thank chemical technicians *Ágnes Molnárné Horváth* and *Balázs Bottó* for their assistance in my daily laboratory work.

I would also like to thank my former and current students, *dr. Eszter Vivien Veres* and *Marcell Tátrai*, for their help with the experimental work.

Furthermore, I extend my appreciation to the *members of the HUN-REN-DE Mechanisms of Complex Homogeneous and Heterogeneous Chemical Reactions Research Group* and the *Department of Neutron Spectroscopy at the HUN-REN Centre for Energy Research* for their professional help and for creating a friendly atmosphere.

I am sincerely grateful to *Dr. István Lázár* for his helpful advices, which made my work easier, especially regarding the use and maintenance of the porosimeter.

I also extend my gratitude to *Dr. Laura Juhász* for taking the SEM images and performing the XRD measurements, and to *Dr. Andraž Krajnc* for conducting the solid-state NMR measurements. I am sincerely thankful to *Dr. Gábor Szemán-Nagy* and *Viktória Baksa* for carrying out the biological tests, and to *Dr. Zsolt Czigány* for taking the TEM images.

Additionally, I would like to thank *Gizella Nagyné Dombi* and *Júlia Mónok* for their assistance in managing everyday administrative tasks.

I owe an indescribable debt of gratitude to *my family*, who have always supported me under all circumstances and provided everything I needed to achieve my goals. Their endless love and support helped me get back on my feet even in the most difficult times.

Last but not least, I would like to thank *my fiancée, Vanda Papp*, for supporting and motivating me throughout my journey and for standing by my side during the most challenging times.

The HUN-REN Centre for Energy Research internal research grant No. 131/2023, and the grant VEKOP-2.3.3-15-2016-00002 of the European Structural and Investment Funds have financially supported this research. The National Research, Development and Innovation Fund of Hungary also supported this study under grant numbers OTKA-124571 and OTKA-139140. I am also thankful for the CERIC proposal No. 20222035 for the financial support. Part of this work is based on work from AERoGELS COST Action (ref. CA18125) supported by COST (European Cooperation in Science and Technology), in particular my scientific mission in Liège, Belgium.

Table of Contents

Abbreviations

BET	Brunauer- Emmett-Teller theory
BJH	Barrett-Joyner-Halenda theory
BSP	Borosilicate – polyvinyl alcohol hybrid gel
DPSC	Dental Pulp Stem Cell
EDS	Energy Dispersive X-ray Spectroscopy
FT-IR	Fourier-Transform Infrared spectroscopy
HAp	Hydroxyapatite
ICP-OES	Inductively Coupled Plasma – Optical Emission Spectrometry
IUPAC	International Union of Pure and Applied Chemistry
MW	Molecular weight
NL-DFT	Non-Local Density Functional Theory
PVA	Polyvinyl alcohol
SANS	Small-Angle Neutron Scattering
SEM	Scanning Electron Microscopy
SLD	Scattering-length density
ssNMR	Solid-state Nuclear Magnetic Resonance
TEM	Transmission Electron Microscopy
TEOS	Tetraethyl orthosilicate
V/V%	Volume percent
w/w%	Weight percent
XRD	X-ray Diffraction

1. Introduction

Aerogels belong to the material family of solid gels, which are classified as coherent systems in the field of colloid chemistry. By definition, coherent systems contain submicroscopic or coarse discontinuities, where particles, micelles, or macromolecules are interconnected to form a three-dimensional network. In the case of gels, the discontinuities are in the colloidal range (1-1000 nm).[1] The synthesis of gels is generally performed in solution phase, with the dispersing fluid being the solvent. Aerogels are such solid gels where the solvent is replaced by air without significantly altering their original backbone, which is typically realized by supercritical drying.

Aerogels have open and interconnected mesoporous structures with high specific surface areas (400-1200 m^2/g) and low envelope densities (0.02-0.50 g/cm^3). There are several possibilities to form a gel from different types of precursors. The literature provides examples of aerogels made from inorganic, organic, or (bio)polymer precursors, or even from different types of precursors simultaneously in the form of hybrids.[2]

Due to the favorable morphological properties of aerogels, and the flexibility and potential in their synthesis routes to prepare materials with suitable properties for different applications, these materials are in the focus of intensive research nowadays. This is evidenced by the fact that aerogels were highlighted by IUPAC in the Top Ten Emerging Technologies in Chemistry in 2022.[3] Based on their chemical and morphological structures, aerogels have potential uses as thermal insulators, catalyst or drug carriers, sorbents, or in the field of tissue engineering.

Designing chemical and morphological features with the intention to benefit a chosen application is not trivial. However, exploring the structural properties of advanced materials that show promising results in the selected

field of application can provide information on the crucial factors that enable high performance. Unfortunately, there are only a few reports in the literature that give deep attention to exploring such structure-properties relationships.

In this thesis, two studies are presented that focus on the detailed investigation of the structures of aerogels and the structural changes that occur during their use. In the first study, we investigated the nanostructure of newly synthesized borosilicate – polyvinyl alcohol (PVA) hybrid aerogels with potential use in bone regeneration. We took special care to investigate the morphological changes that occur when the hybrid aerogels interact with water. In the other study, the focus is on the development of a mathematical model that sufficiently describes the hydration-induced morphological changes of a typical calcium alginate aerogel based on small-angle neutron scattering (SANS) measurements.

2. Research objectives

In the first project, our goal was to develop a new synthesis route to hybridize polyvinyl alcohol (PVA) with an inorganic matrix made of borosilicate. Previously, PVA – borosilicate hybrid glasses showed promising bioactivity in bone regeneration.[4] The hybridization of the inorganic and organic matrices in the nanometer scale can provide beneficial properties for the new material that do not exist in the individual components. The synthesis of the hybrid backbone is carried out using the sol-gel method. Supercritical drying provides a beneficial morphology to the aerogels for tissue engineering, as they have a porous network, which is advantageous for fluid permeability and drug loading.

Another goal was to carefully investigate the nanostructural features of the hybrid aerogels along with their chemical structures. PVAs of different molecular weights were used for the synthesis to explore the effect of the PVA chain length on the structure. To improve the bioactivity of the hybrid aerogels, calcium was incorporated into their backbone in the form of $CaCl_2$, β-$Ca_3(PO_4)_2$, and hydroxyapatite particles. The effects of these additional components were thoroughly studied.

Their morphological changes in the wet state were also studied since the intended application of the hybrid aerogels is in the field of bone regeneration. It is necessary to understand the characteristics of the material in its original form, but if they are altered during use, we must explore these changes to better understand the structure – application relationship.

It was also studied how the structure of a typical calcium alginate aerogel is altered when it interacts with water. The investigation of this phenomenon is crucial, because the focus of the application of these aerogels is in the fields of drug delivery and wound healing, where interactions with

water are inevitable. In a previous study, the wetting of a calcium alginate aerogel was investigated, and the qualitative description of this process was presented.[5] Along with other experiments, small-angle neutron scattering (SANS) measurements were performed. Our goal was to develop a specific model to fit these scattering curves, which can provide quantitative information on the hydration-induced structural changes. Although the development of this new model was aimed at quantitatively describing these scattering curves, the greater purpose of this project was to create a model that can be used to study the structural changes of hydrophilic polymer aerogels during their wetting.

3. Literature overview

3.1. The early history of aerogels

Gels are coherent systems in which the solid backbone is built up by interconnected particles, micelles, or macromolecules to form a three-dimensional network with discontinuities in the colloidal range (1-1000 nm) that are known as pores.[1] The synthesis of the gel backbone is generally achieved by the sol-gel method from a reactant solution and results in a two-phase system, namely the solid backbone and the pore-filling solvent. Replacing the solvent in the pores with air without destroying the original network is rather challenging, because during drying, the surface of the liquid decreases within the gel network, and the capillary forces are strongly present, which ultimately cause the original backbone to collapse. The term "aerogel" originates from its inventor, Samuel Stephens Kistler, who was the first researcher able to replace the pore-filling liquid with air in a gel network without significant shrinkage.[6] He recognized that if the solvent is held under a pressure greater than its vapor pressure and the temperature is increased, then the liquid will transform into gas at the critical temperature without forming two phases. In this way, the capillary forces are eliminated, and the pore-filling liquid can be replaced with air without collapsing the original backbone.[6, 7]

The first of the investigated gels was made of silica. Initially, he tried to dry the silica hydrogel under supercritical conditions, which resulted in failure, even though the assumption was correct. The reason for the failure was that water at its critical point (374.13 °C; 22.1 MPa) dissolves silica. By replacing water with alcohol, supercritical drying was performed successfully, resulting in a highly porous and transparent silica aerogel.[7] Nowadays, supercritical drying is typically done with carbon dioxide (critical point: 31.04 °C; 7.3 MPa), as it is much less dangerous and requires less energy investment

(ethanol critical point: 243.50 °C; 6.4 MPa).[8-11] After the successful synthesis of silica aerogel, Kistler produced several other aerogels from different materials, such as alumina, tungsten oxide, ferric oxide, tin oxide, nickel tartrate, cellulose, cellulose nitrate, gelatin, agar, egg albumin, and rubber.[7]

Although aerogels were introduced to science in 1931, their extensive investigation started only decades later. Silica aerogels were the most widely studied aerogels, because their synthesis was relatively easy from the inexpensive sodium silicate (Na_2SiO_3), also known as water glass in aqueous solution. However, the gelation is induced by acid addition, resulting in the formation of sodium salts that reduce the transparency of the gel. To obtain highly transparent aerogels, the formed hydrogels had to be solvent-exchanged multiple times in water baths to remove the Na-salts. The breakthrough in silica aerogel synthesis occurred in 1976 when Teichner and his colleagues found a better way to synthesize silica aerogels by using tetramethoxysilane (TMOS) as a precursor.[12] The hydrolysis of the precursor results in the formation of a silica sol and methanol as a by-product. Using this method, not only the unnecessary solvent exchange steps can be omitted, but it is also possible to change the proportion of water as a reagent, which can be used to control the degree of hydrolysis and thus the resulting structure. After the successful synthesis of silica aerogels, this method was extended to other metal oxide aerogels, such as alumina, zirconia, and titania.[12]

The manufacturing and application of silica aerogels on an industrial scale first emerged with the production of so-called Cherenkov detectors that are elementary particle detectors. Their potential use in this field is based on their unique properties, such as transparency, high porosity (90-99%), open network structure, and a refractive index much lower than that of silicate glasses.[13, 14]

The use of tetraethoxysilane (TEOS) instead of TMOS soon became widespread, leading to the formation of ethanol instead of methanol in the gelation reaction. Around this time, low-temperature supercritical drying technology also began to appear. This process used liquid or supercritical CO_2 to flush out the organic solvent, instead of achieving the supercritical state of the pure organic solvent.[11] The emergence of these two developments made aerogel production greener and cheaper.

Another breakthrough in aerogel production occurred in 1989 when Pekala developed a new type of aerogel made of resorcinol and formaldehyde, which is as light as silica aerogels but has even lower thermal conductivity.[15] However, the significant discovery was made when this aerogel was pyrolyzed under and inert atmosphere to produce carbon aerogel. The newly discovered aerogel is a very good electrical conductor and has better properties than carbon black, making it an ideal material for electrodes in batteries and supercapacitors.[16] This type of aerogel is still the focus of intensive research nowadays.[17]

The possibility of commercial application of aerogels was greatly hindered by the high cost of the supercritical drying process. In 1992, Jeff Brinker and Doug Smith developed a surface treatment process that allows supercritical drying to be omitted, enabling aerogel-like materials to be produced at atmospheric pressure.[18] This was achieved by attaching hydrophobic groups to the surface of the as-prepared silica gel using a trimethylchlorosilane reagent. During ambient pressure drying, the pore-filling liquid first evaporates, causing the gel to shrink, but as the surface methyl groups repel each other, the gel almost completely regains its original shape. This phenomenon is called the "springback" effect.[18] Soon, Brinker and his colleagues synthesized thin aerogel-like films based on this method.[19, 20] Another advantage of this process is the hydrophobization of the surface,

which helps to maintain the insulating properties by preventing moisture condensation in the hydrophilic porous network.

3.2. Aerogels today

Aerogels have advantageous properties, such as high surface area, low density, low dielectric constants, and low thermal conductivity. Thanks to these properties, they can potentially be used in many areas such as insulators, catalyst supports, low dielectric substrates, sensor platforms, materials for environmental remediation, drug delivery devices and tissue scaffolds.[2, 21, 22] However, the most studied, purely silica aerogels are very fragile, which makes their practical application difficult. Among the aerogels produced so far, those made of polymers have the best mechanical properties, far exceeding those of silica aerogels.[2, 23, 24] It is not surprising that organic and biopolymer-based aerogels have been in the focus of research in the last two decades.

The first polymer aerogels studied in detail were the previously mentioned resorcinol-formaldehyde gels along with melamine-formaldehyde aerogels.[15, 25] These aerogels have better thermal insulation properties than silica aerogels, but their mechanical properties are not superior. Carbon aerogels, which can be produced from them by pyrolysis, are particularly interesting materials, because they can be used as sorbents, hydrogen storage media, and most notably as electrodes in batteries and supercapacitors.[16, 26, 27]

Organic aerogels with high potential for industrial use are polyurea, polyamide, and polyimide-based aerogels that have exceptionally good mechanical and thermal insulation properties, and high temperature tolerance. Their lightweight nature and ability to withstand harsh environments make them ideal for various aerospace applications. By choosing the appropriate reactants, it is even possible to produce flexible polymer aerogels.[28-33]

In the case of biopolymer-based aerogels, two groups can be distinguished: polysaccharide-based and protein-based aerogels. Polysaccharide-based aerogels include cellulose, chitosan, alginates, starch, pectin, and carrageenan gels,[34-40] while the representatives of protein-based aerogels are made of egg-white, whey protein, silk fibroin and gelatin.[41-44] In 2001, Tan and co-workers successfully prepared a cellulose aerogel with exceptional mechanical properties.[37] This achievement has marked the beginning of extensive research into biopolymer-based aerogels. However, the main direction of the development of biopolymer-based aerogels is their potential application in the biomedical field, such as for tissue engineering and as drug carrier systems.[34, 36, 38, 39]

Alginate is one of the most intensively investigated biopolymers for aerogel production, because it is biocompatible, nontoxic, biodegradable, non-expensive and simple to produce. It is potentially useful in the food, chemical, and pharmaceutical industries. Alginate is an anionic polysaccharide composed of two monosaccharides: β-D-mannuronate (M) and α-L-guluronate (G). The gelation of alginate can be performed in the presence of multivalent cations such as Ca^{2+}, Sr^{2+}, Ba^{2+}, Al^{3+}, Fe^{3+}, and others by ionotropic crosslinking. The size and the shape of the gel are crucial for specific applications. These can be altered by using different preparation methods. Based on the diameter of the alginate gel particles, the material can be classified into three groups: (a) macrogels (> 1 mm), (b) microgels (between 0.2 and 1000 μm), and (c) nanogels (< 0.2 μm). The production of alginate macrogels is most commonly achieved by the simple dripping method, where the dropwise addition of the alginate solution to the (usually Ca^{2+}-containing) gelling bath is performed from a loaded syringe. Microgels can be produced using modified extrusion techniques, such as jet-cutting and pulverization, or by emulsification methods. Templating methods, in which nanovesicles or

emulsion droplets serve as templates, are used to formulate nanogels.[45-47] Regardless of the production technique, the aerogels are produced from the hydrogels by supercritical drying.[46, 47]

A new trend has appeared in aerogel research in the last decade, in addition to the investigation of polymer aerogels: the development of so-called hybrid aerogels. The idea behind the development of hybrid aerogels is that by combining two different materials, a final material with properties exceeding those of the individual starting materials can be produced. The most extensively investigated hybrid aerogels are the silica-(bio)polymer ones. Silica aerogels have poor mechanical properties and a limited range of surface chemistry features, but they possess attractive physical properties. Biopolymers offer flexibility, biocompatibility, surface reactivity, low density, and toughness, but their uses are limited by their flammability, compressibility, and inherent hygroscopic properties. By combining the two materials, the disadvantageous properties of the individual materials can be improved, and new specific properties can be achieved.[2, 48, 49]

Another example of combining two different materials is the cross-linked polymer systems, where a suitable polymer network conforms to the surface of the aerogel backbone, chemically linking the elementary building blocks, such as nanoparticles.[2] An example of this is was demonstrated by Paraskevopoulou and co-workers who successfully synthesized polyurea-crosslinked biopolymer (alginate and chitosan) aerogel beads that show much better mechanical properties than the native biopolymers.[50] Contrast variation small-angle neutron scattering measurements were used to highlight the different nanostructural properties of polyurea crosslinked calcium alginates that were produced using either aliphatic or aromatic triisocyanate reactants.[51]

3.3. Synthesis of sol-gel-based silica materials

The synthesis of silica aerogels is usually realized using the so-called sol-gel process. The term "sol" can be defined as a colloidal dispersion containing submicroscopic solid particles dispersed in a liquid medium, while "gel" can be defined as a coherent system containing discontinuities in the colloidal range, where particles, micelles, or macromolecules are interconnected to form a three-dimensional network.[1] According to the IUPAC definition, a colloidal system refers to "...a state of subdivision, implying that the molecules or polymolecular particles dispersed in a medium have at least in one direction a dimension roughly between 1 nm and 1 μm, or that in a system discontinuities are found at distances of that order."[52]

The sol-gel transition is the processes during which a starting sol turns into a gel state. In general, the transition from sol to gel can occur through physical gelation, involving the formation of entanglements (e.g., cooling of a heated gelatin solution), or chemical gelation, involving the formation of chemical bonds (e.g., hydrolysis and polycondensation of alkoxysilanes).

Alkoxysilanes [$Si(OR)_4$] are the most commonly used precursors for synthesizing sol-gel-based silica materials. They are hydrophobic and immiscible in water but react with water molecules through hydrolysis. The rate of hydrolysis depends on the size of the alkoxy group; it is slower with larger alkoxy groups due to steric hindrance and hydrophobicity. Therefore, the hydrolysis is the fastest when TMOS is used. Alongside TMOS, TEOS is also frequently used, despite its hydrolysis rate being approximately six times slower. Larger alkoxy groups are not commonly used due to significantly slower hydrolysis rates.[2, 53]

During the reaction, the corresponding alcohol of the alkoxy group is formed as a by-product. If hydrolysis is complete, silicic acid [$Si(OH)_4$] is formed. However, polycondensation processes occur simultaneously, starting

before the hydrolysis is complete. Polycondensation reactions facilitate the formation of an extensive silicon oxide network, with its structure and growth dependent on various synthesis parameters.[2, 53] The reactions taking place can generally be written as follows.

$$\equiv \mathrm{Si} - \mathrm{OR} + \mathrm{H_2O} \rightleftharpoons \equiv \mathrm{Si} - \mathrm{OH} + \mathrm{ROH} \quad (1)$$

$$\equiv \mathrm{Si} - \mathrm{OR} + \equiv \mathrm{Si} - \mathrm{OH} \rightleftharpoons \equiv \mathrm{Si} - \mathrm{O} - \mathrm{Si} \equiv + \mathrm{ROH} \quad (2)$$

$$\equiv \mathrm{Si} - \mathrm{OH} + \equiv \mathrm{Si} - \mathrm{OH} \rightleftharpoons \equiv \mathrm{Si} - \mathrm{O} - \mathrm{Si} \equiv + \mathrm{H_2O} \quad (3)$$

Water alone can only slowly initiate the hydrolysis and condensation reactions without a catalyst. The selection of the catalyst is crucial, as it significantly influences the sol structure and the gelation time. The rate of hydrolysis and polycondensation can be adjusted by altering the pH, making the catalyst an acid or a base.[2, 53] The decision to use an acid or base catalyst directly affects the final gel structure; typically, an acidic route results in a more compact structure, while a basic route produces a more open and porous structure (**Fig. 1.**).

In addition to the nature of the alkoxy group and the effect of pH, several other factors influence the hydrolysis and condensation reactions and, ultimately, the resulting gel structure.[2, 23, 53] The molar ratio of water to alkoxysilane precursor, the choice of solvent, and the concentrations of the reactants play significant roles. Alkoxysilanes are not miscible with water but dissolve well in a water-alcohol mixture of the correct solvent ratio (usually with an excess of alcohol), making alcohol a common solvent for the reaction. By selecting the appropriate water-to-alkoxide ratio (R_w), complete hydrolysis of a tetravalent alkoxide can be achieved. In practice, using R_w less than 1 results in more ≡Si-OH than ≡Si-O-Si≡, while R_w greater than 1 can ensure complete hydrolysis, as water is a by-product of the condensation reaction.

Although increasing the amount of water can accelerate hydrolysis and condensation, it is important to note that excessive dilution can decrease the rate of gelation. Other important factors include temperature, and the presence of additives, such as surfactants, electrolytes, or, in the case of hybrid systems, the other material forming the backbone, such as polymers.[2, 53]

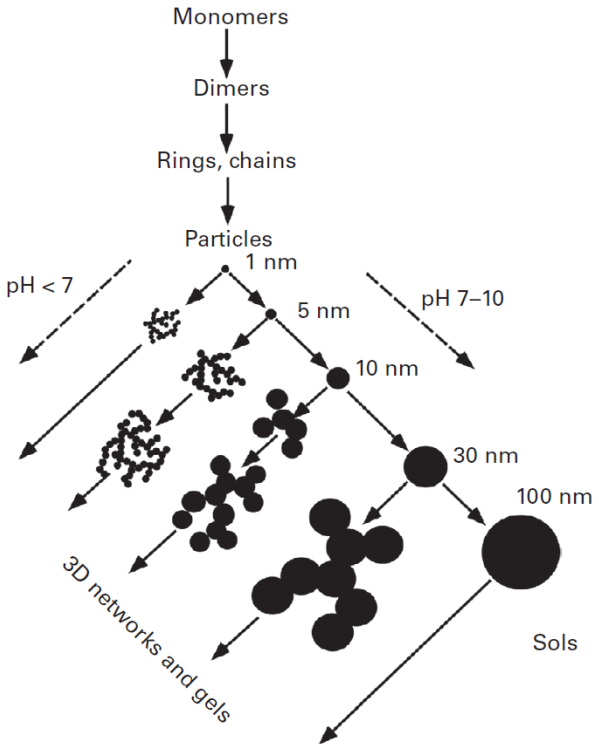

Figure 1. The scheme of the formation pathway of a silica gel backbone at different pH values. The reaction pathway under acidic conditions leads from monomers, such as silicic acid or silicon alkoxides, to oligomers, particles, and open networks of particles. Under basic conditions, the reactions produce larger particles that can also aggregate into open porous networks or form sols of very large particles, typically in the range of 100 nm and above.[53]

3.4. Hybrid and composite silica aerogels

Silica aerogels possess exceptional physical properties, including low density (0.1 g/cm^3), thermal conductivity (12–15 mW m^{-1}K^{-1}), high porosity (>95%), and a specific surface area of 800–1000 m^2/g. However, their poor mechanical properties, such as brittleness and dust release, hinder their widespread application due to their weak pearl-necklace-like nanostructure. These mechanical properties can be improved by reinforcing the backbone with polymers.[2]

The characteristics of the inorganic (silica) and the organic (polymer) interfaces, along with the types of interactions between them, significantly influence the properties of the final hybrid materials. Hybrid aerogels can be classified into two categories, based on the connectivity between the organic and inorganic components. Class I hybrid aerogels are formed by combining two separate organic and inorganic compounds through the sol–gel process, where the composite structure is maintained by physical interactions such as van der Waals forces, electrostatic forces, and hydrogen bonding. In contrast, Class II hybrid materials involve strong chemical interactions, such as covalent, ionic and coordination bonds between the organic and inorganic phases.[54]

Zhao and colleagues successfully synthesized mechanically robust hybrid pectin-silica aerogels with exceptional thermal insulation properties, while also maintaining good hydrophobic characteristics (contact angle >130°). The synthesis was conducted as a one-pot process, with variations in pH and biopolymer concentration. The best mechanical properties and the lowest dust release were observed in pectin-rich aerogels produced at pH 1.5, where the slowest gelation occurred. At pH 3, pectin gelation was faster, while at pH 5, silicic acid gelation was quicker, resulting in different microstructures.

At pH 1.5, both silicic acid and pectin gelation were slow, yielding a homogeneous hybrid with excellent superinsulating properties.[49]

In another study, silica-gelatin aerogels with varying biopolymer contents and surface modifications were successfully synthesized for drug delivery. Three drugs – ibuprofen, ketoprofen, and triflusal – were impregnated into the hybrid gels via a supercritical process. By altering the biopolymer content and modifying the surface properties, both fast and semi-retarded drug release profiles were achieved.[55] In a subsequent study, the structure-property relationships were investigated at the molecular level using NMR techniques and small-angle neutron scattering (SANS), focusing on the effects of varying gelatin content, particularly during wetting. Interestingly, below 11% gelatin content, the pore structure of the hybrid gel remained largely unchanged during wetting. However, at higher gelatin content (>18%), the open-porous structure collapsed, resulting in a hydrogel-like structure. This structural change explains the observed retardation in drug release for high gelatin content and rapid drug release for low gelatin content. Additionally, contrast variation SANS measurements confirmed the homogeneous hybrid structure of the silica-gelatin aerogels at the nanometer scale.[56]

Recently, another research group developed a different sol-gel synthesis route to produce silica-gelatin aerogels with high gelatin content (>15%), using a modified silica precursor, 3-glycidoxypropyl trimethoxysilane (GPTMS), as a coupling agent. The aim of using GPTMS was to strengthen the bond between the silica and gelatin components through chemical interactions. The resulting hybrid aerogels were tested for bone regeneration applications using *in vitro* bioactivity assays in simulated body fluid (SBF) and with osteoblasts. Positive results were obtained in both cases, with the observation of the beneficial effect of the increased gelatin content.[57]

Ilhan and co-workers developed a core-shell type silica-polystyrene composite aerogel with excellent mechanical and thermal insulation properties and hydrophobic characteristics (contact angle >120°). Unlike for previous methods, the starting mixture did not contain the polymer initially, but it was nanocasted onto an amino-functionalized silica gel. First, the amino-functionalized silica gel was produced using aminopropyl-trimethoxysilane (APTMS) along with TMOS. The dangling amino groups were then reacted with *p*-chloromethylstyrene to introduce surface styrene groups. Polymerization was subsequently carried out using styrene and AIBN (2,2'-azobis-isobutyronitrile) at 75°C. After polymerization, the unreacted reagents were washed out of the pores with acetone, and the polystyrene cross-linked gel was dried under supercritical conditions.[58]

3.5. Aerogels for biomedical applications

Aerogels can be utilized in many fields of industry due to their chemical and structural diversity provided by the versatile synthesis routes. Along with the appearance of (bio)polymer and hybrid aerogels, much research has been started recently on their biomedical applications, such as drug delivery and tissue engineering.[2, 40, 59-65]

The application of biopolymer aerogels in the biomedical field is evident due to their excellent biocompatibility and biodegradability. Extensive research focuses on utilizing polysaccharide aerogels, such as alginate-based aerogels as drug delivery vehicles.[47, 66, 67]

In a recent study, Duong et al. successfully synthesized calcium alginate aerogel beads with aerodynamic diameters of 1–5 μm using compressed air-assisted prilling gelation. These aerogel beads were impregnated with beclomethasone dipropionate (BDP), a poorly water-soluble anti-inflammatory drug for asthma treatment. The impregnation was

performed using a cosolvent-assisted supercritical CO_2 ($scCO_2$) method, which preserved the porous nanostructure of the alginate aerogels and provided high BDP loadings and ensured the amorphization of the drug. In vitro cytotoxicity tests confirmed the non-harmful nature of the aerogel. Ex vivo bronchial permeability tests indicated that BDP released from the aerogel carrier was effectively localized in the porcine bronchial tissues in higher concentrations compared to pure BDP without an excipient. The advantageous formulation of the aerogel beads and the high drug-loading efficiency using the $scCO_2$ method highlight the great potential of these aerogels for pulmonary drug delivery.[47]

Hybrid silica-polymer aerogels are also being explored for biomedical applications, such as the silica-gelatin aerogels mentioned in Section 3.4.[48, 55, 57] Recently, Groult et al. synthesized silica-pectin aerogels using a wide range of synthesis conditions. The silica precursors, TEOS and polyethoxydisiloxane (PEDS), were altered, and pectin was either crosslinked with Ca^{2+} ions or not. The pectin gel was prepared under acidic conditions and then impregnated with a silica sol derived from TEOS or PEDS. For crosslinked pectin gels, $CaCl_2$ was added to the acidic medium. All resulting gels were impregnated with a model drug, theophylline, and drug dissolution was tested in various media. Notably, drug dissolution in gastric fluid with enzymes and in simulated intestinal fluid without enzymes was slower for the crosslinked pectin gels. Furthermore, only the crosslinked aerogels remained stable in aqueous systems, while the others disintegrated immediately upon contact. Due to their ability to control drug release over time and their lack of cytotoxicity, these aerogels show good promise for biomedical applications.[68]

Autografts remain the gold standard for healing various bone defects, but their disadvantages, such as donor site morbidity and complications from additional surgeries, necessitate the development of new methods.[69, 70] Synthetically produced bone replacement materials offer a promising

alternative. These materials must meet several criteria, such as adequate biocompatibility, appropriate morphology, and suitable mechanical properties to effectively mimic natural bone tissue. Cancellous bone, for instance, has a highly porous structure (porosity 40-90%) with interconnected pores, composed of a mineralized organic matrix. This three-dimensional structure, with its large specific surface area, provides an optimal environment for bone cells while maintaining excellent mechanical properties.[71, 72]

The high porosity of aerogels, coupled with the nanostructured features of their skeletons facilitate cell attachment and provide interconnectivity for the supply of nutrients and oxygen to cells and the elimination of metabolic by-products. These characteristics make aerogels valuable for regenerative medicine. Additionally, aerogels can be designed in almost any shape and morphology needed for the scaffolds. However, aerogels typically lack the macroporosity required for bone ingrowth and vascularization, as well as the bioactivity to promote tissue growth. Furthermore, their mechanical properties are often insufficient to withstand the stresses needed for being bone scaffolds. Consequently, research is focused on developing advanced aerogels for tissue engineering by enhancing their mechanical stability, creating macroporous structures, and bio-functionalizing the materials.[59, 73] **Figure 2** illustrates the main potential aerogel-based bone substitute materials based on their chemical and structural properties.

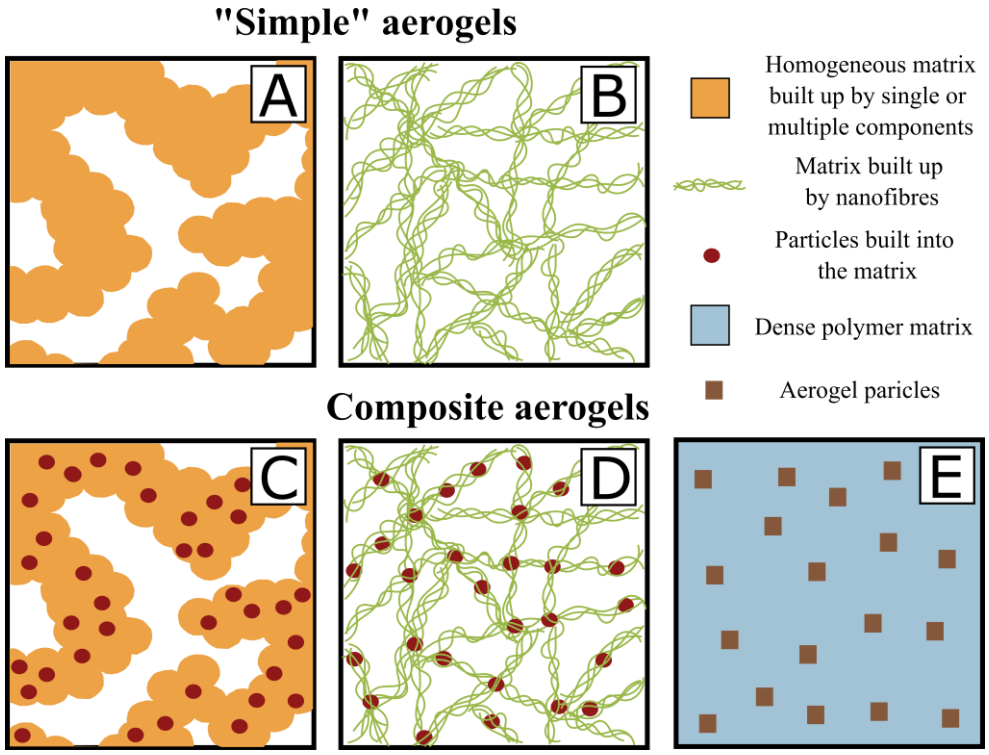

Figure 2. Schematic illustrations of the main aerogel-based synthetic bone substitutes according to their chemical and structural features. **Panel A:** Homogeneous aerogel matrix consisting of one or multiple components (hybrid structure). **Panel B:** Aerogel matrix built up by nanostructural fibers. **Panels C and D:** Aerogel matrix (either as in **Panel A** or **B**) with incorporated particles. **Panel E:** Dense polymer matrix with incorporated aerogel particles.

One group of representatives of potential aerogel-based bone substitutes is single-phase aerogels (**Fig. 2a**), in which the matrix can be built from one or multiple components. The term single-phase means that, in the case of multiple components, they are homogeneously dispersed within the gel matrix at the molecular level, such that the inorganic and organic parts cannot be distinguished.[73] A good example of this group is the silica-gelatin hybrid aerogels mentioned in Section 3.4.[57]

Another possible choice is (bio)polymer gels, in which the matrix is built from nanostructural fibers (**Fig. 2b**). In a recent study, Iglesias-Mejuto et al. successfully combined the benefits of 3D printing and aerogel preparation technologies to produce alginate aerogels with dual (meso- and macro-)

porosity as bone graft materials. Concentrated alginate solutions were used as bioinks for 3D printing, resulting in a three-dimensional dual-porous hydrogel. The as-prepared hydrogels were then immersed in $CaCl_2$ solutions to strengthen the polymer backbone. After multiple solvent exchange steps, supercritical drying was used to produce aerogels. The resulting aerogels showed promising results during experiments with cell cultures, making them ideal candidates for bone regeneration.[61] To improve the textural properties and potentially increase the bioactivity of the scaffolds, hydroxyapatite-containing alginate bioinks were also used. The preparation of these composite materials (**Fig. 2d**) followed the same process as for hydroxyapatite-free samples. The resulting samples had a rougher backbone surface and exhibited similar bioactivity. However, testing the volume shrinkage of the scaffolds revealed that composite gels with high hydroxyapatite content showed significantly smaller shrinkage in aqueous conditions, which is beneficial for this application.[61]

Silica aerogels incorporated with microcrystalline or nanocrystalline $Ca_3(PO_4)_2$ and/or hydroxyapatite (HAp) were synthesized (**Fig. 2c**) and systematically investigated for their potential as artificial bone substitutes in the studies.[73-77] The silica matrix was prepared via a sol–gel process under basic conditions, during which the Ca(II) sources, along with microcrystalline cellulose, were dispersed into the reaction mixture at the gelation stage. Various forms, including large monoliths, small cylinders, spheres, and irregularly shaped particles, were produced and dried using supercritical CO_2.[73-77] The biopolymer acted as a template and was burned out at 500°C. High-temperature treatment (500–1000°C) modified the dissolution profiles and mechanical properties of the composites while preserving their mesoporous structure and high specific surface area. Samples treated at higher temperatures exhibited increased shrinkage and compressive strength, with

values reaching up to 102 MPa. Materials annealed at 900°C and 1000°C were robust enough for load-bearing applications.[73-77] In vitro testing in simulated body fluid (SBF) confirmed the formation of a microcrystalline HAp layer on the composite surfaces.[74] Cellular studies using MG-63 and SaOS-2 cells assessed metabolism, proliferation, and gene expression.[75-77] Additionally, in vivo small-animal experiments were performed on rats.[76] Both in vitro and in vivo experiments demonstrated the bioactivity and bone regeneration potential of the composite silica aerogels. Notably, samples annealed at 800°C exhibited the highest bone regeneration potential.[73-77]

Poly(methyl-methacrylate) (PMMA)-based bone cements are commonly used in medical practice for filling bone cavities or securing metallic implants in place. While these bone cements are bioinert materials, they do not promote ossification on their surface. To address this limitation, Lázár and colleagues incorporated functionalized silica aerogels as guest particles into an in situ polymerized PMMA matrix (**Fig.2e**) and evaluated their bioactivity in SBF. The results demonstrated increased compressive strength compared to pure PMMA.[73, 78] When exposed to SBF, the hydrophilic silica aerogel dissolved from the polymeric matrix, leaving behind a highly porous surface. Unlike the smooth surfaces of traditional PMMA bone cements, this newly formed porous surface could offer significant advantages by enhancing bone tissue adherence.[73, 78]

Some previously studied bone scaffolds, such as inorganic silica gels and bioglasses are often used in their bulk forms as cavity fillers, because they exhibit only moderate biological responses. These bulk formulations, even when used as small particles, require improvement to facilitate mass transport of biological fluids. For the same reason, although $Ca_3(PO_4)_2$ bioceramics have excellent biocompatibility and long-term integration with living bones, they are not ideal for bone regeneration applications on their own. Consequently,

novel nanostructured porous formulations of these biomaterials are being extensively researched.[79, 80]

Additionally, the ability of such inorganic materials to interact with bone-forming cells can be enhanced by integrating biologically active polymers into them, creating organic-inorganic hybrid materials.[79, 80] Selecting the appropriate biocompatible and biodegradable polymer is crucial for the successful formation of new bone tissue. Among synthetic polymers, polylactic acid (PLA), polyglycolic acid (PGA), and their copolymers (PLGA) are commonly used in bone regeneration applications.[81-83] However, these poly(α-hydroxyesters) can degrade into acidic byproducts in a biological setup, which can trigger inflammatory responses.[84]

Polyvinyl alcohol (PVA) is a biocompatible, biodegradable, hydrophilic synthetic polymer that is chemically inert. It is widely used in pharmaceutical technology and has been tested in tissue engineering. Applications include soft contact lenses, artificial cartilage and wound dressing, while it has also been proposed for bone regeneration.[85-87] Recently, Pang et al. successfully synthesized PVA-borosilicate hybrid bioglasses, demonstrating promising bioactivity.[4] The chemical bonding between PVA chains and the borosilicate matrix allows for the slow, controlled release of boron compounds, which promotes cell proliferation and differentiation.[88, 89]

The fundamental concept behind synthesizing borosilicate–PVA hybrid aerogels in the present study is to utilize the beneficial properties of aerogels, such as their nanostructured surfaces and open mesoporous systems, to create materials with a chemical composition that promotes the stimulation and attachment of bone-forming cells.[90]

3.6. Small-angle scattering (SAS)

3.6.1. Fundamentals of SAS

Aerogels consist of two distinct phases: the solid backbone and the pore-filling phase. Each phase is defined by a set of basic parameters, such as phase fraction, characteristic dimensions, and connectivity. Additionally, the physical and chemical properties of the large interface (surface area) between these two phases are critical characteristics of aerogels. In order to fully understand the aerogel structure, various characterization techniques must be employed. Scattering techniques are particularly useful as they are quantitative, noninvasive, and nondestructive nanoscale characterization tools for structural analysis. They can be used to study the in situ nanoscale structural changes of solvated gels and aerogels during the sol–gel transition, aging, drying, sintering, application of mechanical stresses, or wetting.[2, 5, 51, 56, 91, 92]

Elastic scattering is sensitive to the relative structural arrangement of scatterers within a specimen. When an incident monochromatic wave front strikes the specimen, a spherical wave is formed by the interaction of neutrons/X-rays with the atomic nuclei/electron shell of the atoms constituting the studied material, as shown in **Fig. 3.** These spherical waves interfere, producing a scattering pattern. The scattered intensity is measured based on the difference between the incident $(\vec{k})$ and scattered $(\vec{k'})$ wavevectors. To capture the scattering pattern, neutron or X-ray detectors are used. [2, 93] It should be noted that interactions between neutrons and matter can result in the absorption of neutrons as well, but most neutrons in the beam pass through the sample without interaction due to the short-range nature of nuclear forces. Only a small portion of the neutrons in the beam interacts with the sample in a way that results in a scattering event.

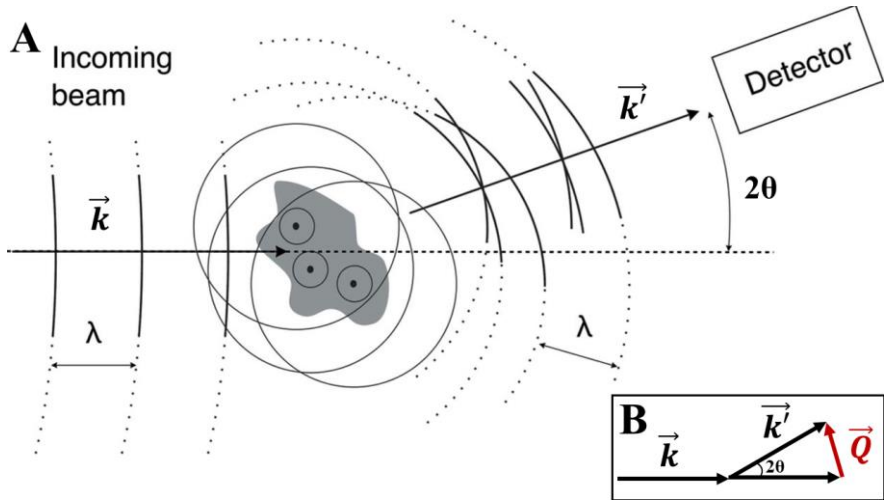

Figure 3. Panel A: An incoming beam of plane waves with wavelength λ creates an isotropic secondary wave of the same wavelength by interacting with the scattering centers of the material. The intensity detected at any given angle 2θ is the result of the interference of the secondary waves. **Panel B:** The scattering vector Q is defined by the difference of the incident $(\vec{k})$ and the scattered $(\vec{k'})$ wavevectors.[94]

In small-angle scattering (SAS) experiments, intensities are plotted against the magnitude of the scattering vector (or momentum transfer) Q, defined as,

$$Q = \frac{4\pi}{\lambda} sin(\theta) \quad (4)$$

where λ is the wavelength of the incident X-ray photons or neutrons, and θ is half of the scattering angle. Q is defined by the difference of the incident and the scattered wave vectors, where in case of elastic scattering $|\vec{k}| = |\vec{k'}| = 2\pi/\lambda$. Plotting the scattering intensity against Q has the advantage of being independent of the selected wavelength for the experiment, unlike plotting against 2θ.[2, 93, 94]

The wavelength of the incident beam or the sample-detector distance can be adjusted to alter the covered Q-range. SAS approximately covers 2θ scattering angles from 0.001° to 10°, with wavelengths typically ranging from a few Angstroms to a few nanometers. The corresponding Q-range extends

from about 5 nm^{-1} to 10^{-4} nm^{-1}, with the lower Q limit corresponding to ultra-small-angle X-ray and neutron scattering (USAXS and USANS, respectively). Since the Q value relates to a length scale of L given by $Q \approx 2\pi/L$, SAS can probe structural features in the scale from ca. 10 μm to a few Angstroms.[2, 94]

The strength of the interactions between X-rays and atoms in condensed matter is dependent on the number of orbital electrons, which corresponds to the number of protons in the atoms. For neutrons, the interaction strength depends on short-range nuclear interactions, and it is described by the scattering length, b. The magnitude of b indicates the "strength" of the scattering, while its sign shows whether the incident and outgoing waves are in phase or 180° out of phase. The scattering interaction represented by b is a complex number, it depends on the nucleus's composition and the orientation of its spin (if non-zero) relative to the incident neutron's spin. Consequently, scattering lengths are isotope-specific, can have different values for nuclei with non-zero spin, and do not vary with atomic number in a monotonous manner. For example, a proton has a scattering length of -0.374×10^{-14} m, while deuterium has a scattering length of 0.668×10^{-14} m.[93]

This characteristic allows devising contrast variation measurements in SANS. Contrast variation refers to the technique used to enhance or reduce the visibility of a specific component within a sample. This is achieved by altering the scattering length density (SLD) of a component, typically by filling the sample with a fluid containing different isotopes (such as D_2O and H_2O). By adjusting the contrast, particular parts of the sample can be selectively highlighted or obscured, allowing for detailed analysis of the internal structure (see **Fig 4.**). [93]

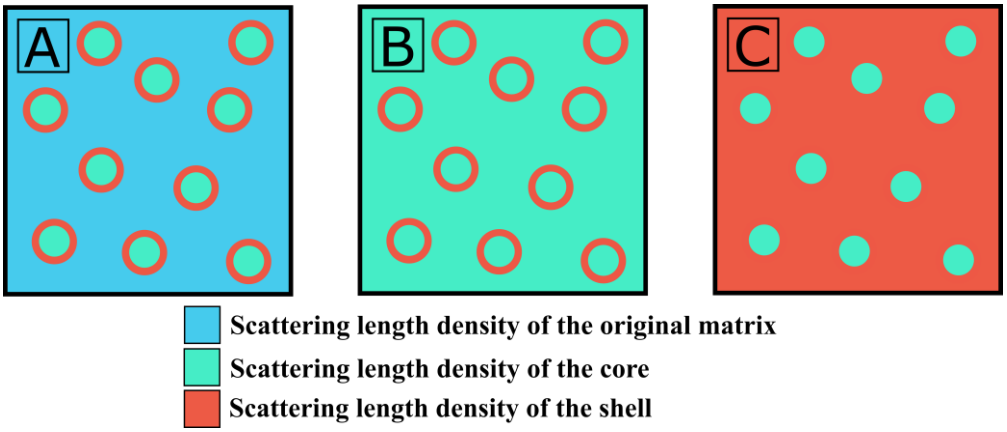

Figure 4. Schematic illustration of contrast variation on the measurable structure of a core-shell particle. The different scattering length densities (SLD) of the particles and the matrix are color-coded as indicated in the legend. **Panel A:** Core-shell particles in the original matrix. **Panel B:** Core-shell particles in a matrix which has an SLD equivalent to that of the core. **Panel C:** Core-shell particles in a matrix which has an SLD equivalent to that of the shell.

In the case of solid samples, contrast variation involves filling the sample with a mixture that has an SLD equivalent to one of the components of the sample, effectively matching it out and providing information on the other components.[2, 51, 93]

The measured scattering intensity is related to the square of the Fourier transform of the spatial distribution of SLD within the sample. Because of this squaring, the phase information, which is crucial for reconstructing the exact spatial arrangement of atoms, is lost in the transformation process. The interference pattern of the scattered neutron or X-ray waves measured on a detector is an intensity pattern that depends on the relative phases of the waves, but this pattern only provides information on the amplitude and not the phase differences directly. Therefore, SAS detectors measure the intensity of scattered neutrons/X-rays, which is related to the square of the amplitude of the scattered wave.[93]

If the scattered neutron waves originating from nuclei with identical scattering lengths interfere, coherent scattering occurs. However, if there is no

correlation in the scattering patterns produced by different nuclei, an incoherent contribution results. The incoherent contribution arises due to random variations in isotope and spin distribution. Structural information about inhomogeneities within the sample is provided only by coherent scattering.[93, 95]

The differential scattering cross-section is expressed per unit solid angle and gives the scattering intensity distribution as a function of the scattering angle. It can be expressed in terms of the experimentally determined intensity *I(Q)*, as follows:

$$\frac{d\sum}{d\Omega_{coh}}(Q) = I(Q)\frac{c}{I_0 \times T_S \times d_S \times A_S \times \Delta\Omega} \quad (5)$$

where I_0 is the normalized intensity of the incident beam; T_S, A_S, and d_S are the transmission, irradiated sample area, and thickness of the sample, respectively. $\Delta\Omega$ is the unit solid angle, and c is a calibration constant. To convert the detector counts per detector pixel area per time into a scattering differential cross-section in absolute units (cm^{-1}), the intensity must be calibrated using a sample with a known scattering differential cross-section. Common reference materials include those with a known differential cross-section over a large *Q*-regime or samples with negligible coherent scattering. Such samples are for example glassy carbon for small-angle X-ray scattering (SAXS) or vanadium with known incoherent scattering and adsorption cross-sections for SANS. Because the incoherent scattering of the vanadium is low, it is used for pre-calibrating a 1 mm thick water sample with high incoherent scattering. Water cannot be used without pre-calibration because of its inelastic scattering.[2, 93]

3.6.2. Mathematical models

The characteristic scattering pattern for a silica aerogel with a fractal, i.e. self-similar backbone structure reflects various structural features across different length scales, as illustrated in **Fig. 5**. In a double logarithmic plot, three distinct regions of power-law scattering can be recognized.[96]

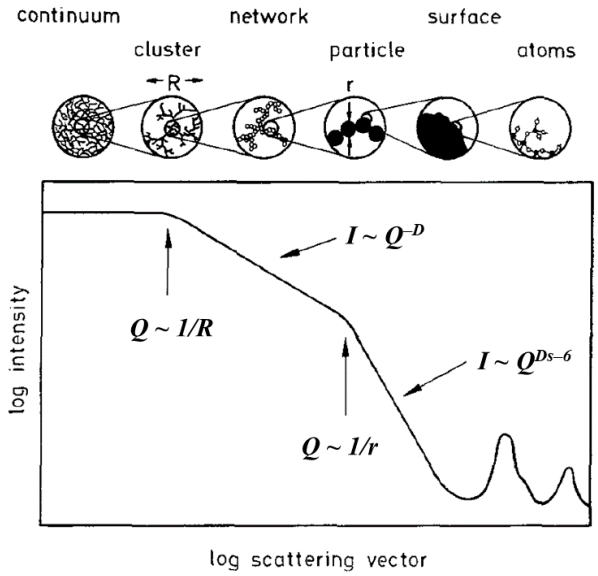

Figure 5. A typical small-angle scattering pattern of a silica aerogel with a fractal structure, plotted on a double logarithmic scale. The scattering pattern highlights all structural features at different length scales in the different *Q*-regions, as described in the text.[96]

At the smallest *Q*-values, the scattered intensity tends to remain constant, because at these large length scales, the scattering experiment cannot resolve smaller inhomogeneities within the sample. The intermediate *Q*-values show a dependence that can be attributed to the fractal nature of the solid skeleton built from clustered particles. Here, the intensity decreases as Q^{-D}, where D is the mass fractal dimension of the solid clusters, assuming monodispersed particles and clusters. If there is a distribution of cluster sizes, the relationship between the power-law exponent and fractal dimension holds

only if the cluster size distribution follows a power-law.[96] At large Q-values, the power-law behavior Q^{Ds-6} is attributed to the surface morphology of the solid particles. The surface fractal dimension D_s characterizes the surface roughness, with D_s=2 indicating a smooth surface and $2<D_s<3$ indicating a rough surface. Beyond Q-values of about 1 $Å^{-1}$, scattering becomes sensitive to the molecular structure (and it is out of the range of small-angle scattering). The positions of the two crossovers separating the power-law regions correspond to the average sizes of the particles and clusters, respectively.[96]

SAS can yield information on the shape, size, and orientation of scattering objects from the nanometer to the micrometer range. However, obtaining meaningful structural insights requires an appropriate mathematical model to analyze the scattering pattern.[94, 97]

Assuming that the scattered intensity originates from a single nanoparticle across the entire Q range, the measured intensity is proportional to the form factor of that nanoparticle, which is identical to its SAS fingerprint. In this case, the intensity can be expressed as:[94]

$$I(Q) = \Delta\rho^2 V^2 P(Q) \quad (6)$$

where $\Delta\rho$ is the SLD difference between the matrix and the nanoparticle; V is the particle volume, and $P(Q)$ is the form factor. In equation (6), $\Delta\rho$ corresponds to the electron density for X-ray scattering or the neutron scattering-length density for neutron scattering.[94, 97] In the literature, several form factors can be found to describe particles with specific shapes such as spheres, ellipsoids, cylinders, and plates.[97, 98] Particles with spherical shapes, for example, can be mathematically expressed as:[94, 97]

$$P(Q) = 3\left[\frac{sin(Qr) - Qrcos(Qr)}{(Qr)^3}\right]^2 \quad (7)$$

where *r* is the particle radius.

In reality, the measured scattered intensity originates from several particles. In most situations, the orientation of these particles within the sample is not independent, and the scattering contribution from a group of particles is represented by the structure factor. In this case, the modified version of equation (6) can be expressed as:[94, 97]

$$I(Q) = c\Delta\rho^2 V^2 P(Q) S(Q) \quad (8)$$

where *c* is the number of the particles in unit volume, and *S(Q)* is the structure factor. The structure factor represents the interference between scattering from different particles and provides insights into particle interactions. In very dilute systems the structure factor becomes unity (*S(Q)* = 1).[94, 97]

The Guinier and power-law approximations are fundamental tools for analyzing SAS data and extracting key structural parameters, especially when nanoparticles do not have well-defined geometrical shapes (as in the case of many solid gels) that can be described by the Fourier transform of their mathematical descriptions.[93-95]

The Guinier approximation provides information on the overall size of the scattering particles through the radius of gyration (R_g). This approximation is valid, when the condition $QR_g < 1$ is met, and can be expressed as:[93]

$$P(Q) \cong exp\left[-\left(QR_g\right)^2/3\right] \quad (9)$$

where R_g^2 is the average squared distance between any point of the particle and its center of mass.[94] The Guinier approximation offers a universal, model-independent method for determining particle sizes from SAS data. However, by assuming certain structural models, the radius of gyration (R_g) derived from this method can be related to specific particle shapes.[93-95] For example,

assuming spherical geometry, the mean diameter (d) of the scattering objects can be calculated from the gyration radius as:[94]

$$d = 2\sqrt{\frac{5}{3}}R_g \qquad (10)$$

It should be noted that if the scattering object has a well-defined shape, such as a sphere, the form factor specific to that shape (e.g., equation (7)) should be used to obtain accurate structural information. The Guinier approximation is a useful tool for determining an estimated size of a scattering object when it does not have a characteristic shape.

In the SAS region where the intensity decreases according to a power law with exponent α, the value of α can provide qualitative information on the structure. A specific case is when α equals 4, which is known as Porod's law. The Porod approximation offers insights into the surface area and surface roughness of the scattering particles. This approximation is typically valid only under the condition $QR_g > 1$, and is expressed as:

$$I(Q) \approx \frac{2\pi(\Delta\rho)^2 S}{Q^4} \qquad (11)$$

where S is the surface area of the scattering particles (or interfaces) within the sample. Porod derived this fourth power-law under the assumption of a distinct phase boundary between the particle and the surrounding medium, and it indicates a smooth surface.[93-95, 98, 99]

When α is between 3 and 4, it suggests a rough surface at the interface between the scattering object and the matrix, whereas α is higher than 4, it indicates a smooth or progressive transition. Conversely, a power exponent between 1 and 3 suggests a mass (volume) fractal structure, such as aggregates. In this way, the power-law approximation is a helpful tool for gaining insights into the qualitative nature of the nanoscale structure. [93-95, 98, 99]

The unified exponential/power-law model developed by Beaucage can simultaneously describe the structural features in both the Guinier and the power-law regions without introducing additional parameters beyond those that are used in the local fits. This unified approach can identify Guinier regimes that are hidden between two power-law regimes, and it is applicable to a wide range of systems, providing a good approximation for any morphology containing a random distribution of structural elements. Generally, this model can be used to examine hierarchical systems in which several structural levels appear, expressed as

$$I(Q) \cong \sum_{i=1}^{N} \left[G_i \exp\left(-\frac{Q^2 R_{gi}^2}{3}\right) + B_i exp\left(-\frac{Q^2 R_{g(i+1)}^2}{3}\right)\left(\frac{1}{Q_i^*}\right)^{p_i} \right] \quad (12)$$

where

$$Q_i^* = Q\left[\mathrm{erf}\left(\frac{Q R_{gi}^2}{\sqrt{6}}\right)\right]^{-3} \quad (13)$$

$G=c\Delta\rho^2V^2$ is the Guinier scaling factor, and B is the Porod scaling factor specific to the type of power-law scattering.[100, 101] The variable i represents the number of structural levels in the hierarchical system. This model, as explained before, provides information on the average size of the scattering objects, and on the fractal dimension at each structural level.[100, 101]

The disadvantage of SAS techniques are their indirect nature, because accurate structural information on the samples can only be obtained by fitting the scattering curves with a physically appropriate model. Choosing the correct model requires some prior knowledge of the sample, such as its chemical composition, concentration (in the case of colloidal particles in liquids), or, in the case of solid gels, information on their morphologies (e.g., SEM images).

This information on the investigated sample can give a hint about the potential scattering objects, and, in turn, the estimated structure. The shape of the scattering curves also provides valuable insights, as the α exponent of the power-law scattering indicates the qualitative nature of the structure in regions where the intensity decreases following that exponent.[94, 97]

The suitability of the chosen model can be assessed by the goodness of the fit results. Typically, least-squares methods are used to measure the deviation between the experimental data and the model. This deviation is described by the chi-squared function (χ^2), expressed as:[97]

$$\chi^2 = \sum_{i=1}^{N} \left(\frac{I_{exp}(Q_i) - I_{mod}(Q_i)}{\sigma_i} \right)^2 \qquad (14)$$

where $I_{exp}(Q_i)$/ $I_{mod}(Q_i)$ represents the measured/modelled intensity at the i^{th} data point of Q; N is the total number of data points; and σ_i is the uncertainty in $I_{exp}(Q_i)$.[97]

The value of $I_{mod}(Q_i)$ depends on the adjustable parameters (M) of the model. It is often useful to consider the reduced chi-squared (χ_r^2) value, which compares fits with different degrees of freedom and is expressed as:

$$\chi_r^2 = \frac{\chi^2}{N - M} \qquad (15)$$

where N-M is the number of degrees of freedom. A value of $\chi_r^2 \approx 1$ suggests a good fit, while values significantly larger or smaller than 1 indicate poor fitting or overfitting.[97]

It should be noted that a good fit alone is not necessarily sufficient to obtain accurate information on the investigated nanoscale structure. If the applied model does not accurately represent the physical characteristics of the sample, the fit results will be irrelevant.

4. Experimental methods

4.1. Materials

Polyvinyl alcohols (PVAs) MW 13 – 23 kDa (87 – 89% hydrolyzed) and MW 89 – 98 kDa (>99% hydrolyzed), β-tricalcium phosphate (unsintered, ≥98%), hydroxyapatite (HAp; 5 μm particles, surface area ≥ 100 m^2/g), D_2O (deuteration degree >99%) were purchased from Sigma-Aldrich. PVA MW 49 kDa was purchased from Fluka (degree of hydrolysis is not identified). Tetraethyl orthosilicate (TEOS) and ammonium fluoride were purchased from Merck. Ortho-boric acid, calcium chloride (anhydrous, powder, ≥93% purity), absolute ethanol, acetone (≥99.8%, Reag. Ph. Eur. analytical reagent with maximum 0.2% water content), and hydrochloric acid (37%) were obtained from VWR. The aqueous solutions were prepared with doubly-deionized and ultra-filtered water (ELGA PureLab classic system). Carbon dioxide cylinders (Biogon-C, 99.95%) equipped with dip tube were purchased from Linde Gáz Magyarország Zrt. (Debrecen, Hungary).

4.2. Synthesis of the borosilicate – PVA hybrid aerogels

The synthesis of borosilicate – PVA hybrid (BSP) gels was performed in three steps using a sol-gel method at room temperature.[90] First, 10.18 mL of TEOS was added to a mixture of 10.67 mL ethanol, 4.40 mL water and 100 μL 0.10 M HCl (water/TEOS molar ratio: 5.4/1). Acidic conditions were used to promote the hydrolysis of the silica precursor. After 1 h, 30.0 mL of 10 w/w% boric acid in ethanol and 30.0 mL of 5 w/w% aqueous PVA solution were added to the mixture under vigorous stirring to initiate the formation of the hybrid gel. Three types of different molecular weight PVAs (13 -23 kDa; 49 kDa and 89 -98 kDa) were used. To prepare Ca(II) containing gels, three different types of Ca(II) sources were used, namely $CaCl_2$, β-$Ca_3(PO_4)_2$ and

hydroxyapatite ($Ca_{10}(PO_4)_6(OH)_2$ – HAp). For $CaCl_2$ and β-$Ca_3(PO_4)_2$, the same molar amount of Ca^{2+} ions from the Ca(II) sources was used, specifically 0.0121 moles. In the case of HAp, the aim was to maximize the Ca(II) content; therefore, a much higher amount was used, 0.200 moles with respect to Ca^{2+}.

After 2 h, 1.0 mL of 1.0 M NH_4F (HCl/ NH_4F molar ratio: 1/100) was added to the final mixture as a catalyst to promote the gelation, then it was poured into a plastic mold. The gelation mechanism in the presence of NH_4F involves fluoride ions acting as nucleophilic catalysts to accelerate both hydrolysis and condensation of the silica precursor. This approach leads to rapid gel formation with controlled structural properties.[102] Because the β-$Ca_3(PO_4)_2$ and HAp do not dissolve, the stirring lasted until the Ca(II) source was no longer able to settle due to the increasing viscosity of the mixture. The gelation took place in the plastic mold at room temperature in 72 h. After it, the monolithic gels were placed into perforated aluminum containers and immersed into pure ethanol. In a multi-step solvent exchange process, ethanol was replaced by pure acetone. The volume ratio of the acetone was increased by 25% in each step, and finally the gels were soaked in pure acetone. Acetone was used as obtained (see. Section. 4.1.) without any further treatment. At least 24 hours elapsed between two steps. The gels were dried under supercritical conditions in an autoclave reactor following a previously published method.[9] First, the acetone was extracted with liquid CO_2 (48 bar, room temperature), then the gels were dried with supercritical CO_2 (100 bar, 80°C). The scheme of the synthesis, and photos of the hybrid aerogels are shown in **Fig. 6.**

The BSPXY code system is used to differentiate the as-prepared aerogels based on their compositions. The BSP refers to the borosilicate-PVA hybrid gel, X refers to the molecular weight of the PVA in kDa, and Y refers to the Ca(II) source. The theoretical compositions of the BSPXY aerogels with the code names are given in **Table 1.**

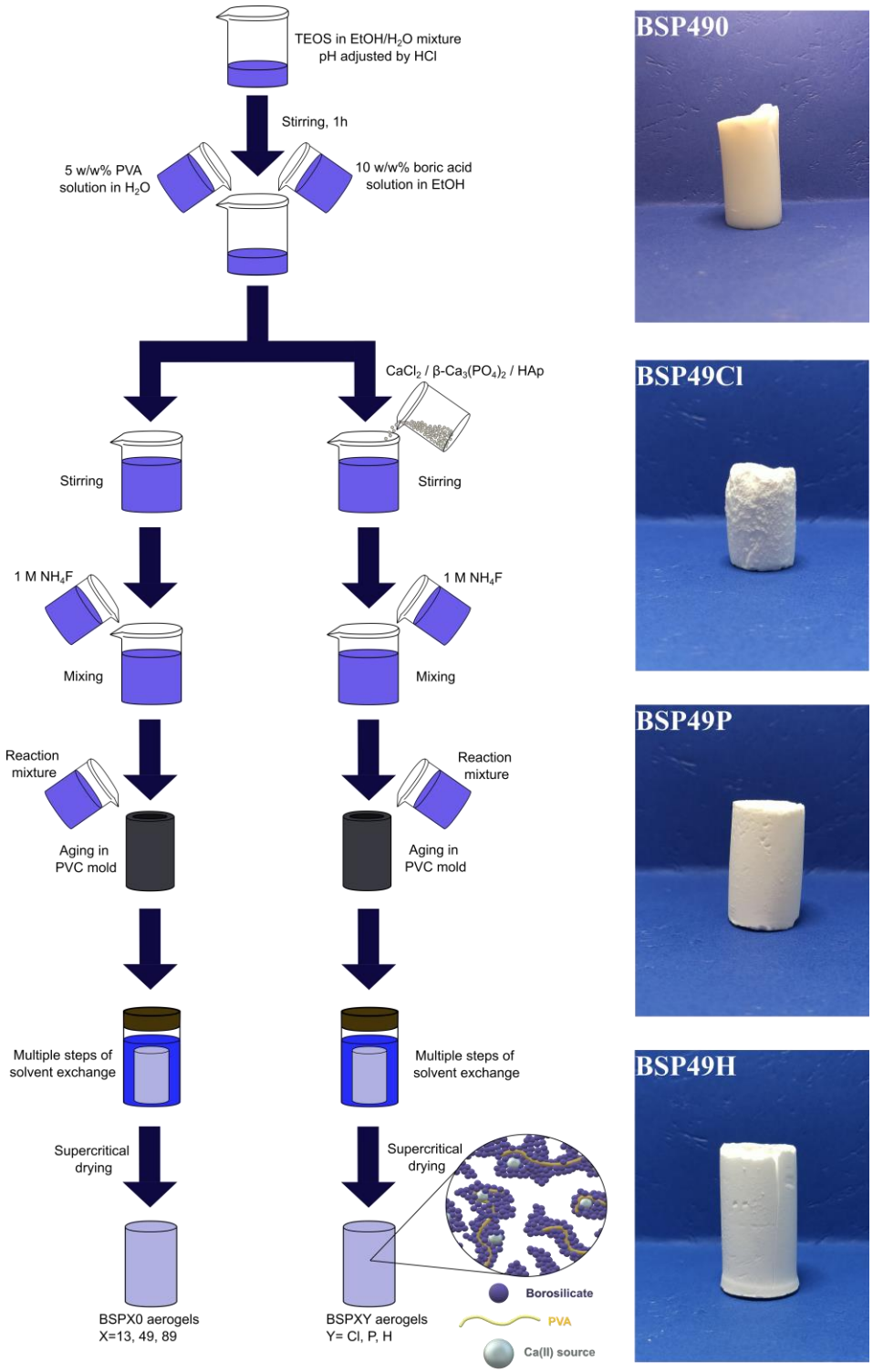

Figure 6. Synthetic scheme for the preparation of the BSPXY aerogels, and the photos of the as-prepared monolithic BSP49Y aerogels.

Table 1. The theoretical composition of the borosilicate – polyvinyl alcohol hybrid aerogels with their code names, and the molar ratios of the chemicals used during the synthesis.

Code name	MW of PVA (kDa)	Ca(II) source	Ca(II) : TEOS : H_3BO_3 molar ratio	Ca(II) source : SiO_2 : B_2O_3 : PVA (w/w)%
BSP130	13 – 23	–	0 : 1.1 : 1.0	0 : 47 : 26 : 27
BSP13Cl	13 – 23	$CaCl_2$	1.0 : 3.8 : 3.5	19 : 38 : 21 : 22
BSP13P	13 – 23	β-$Ca_3(PO_4)_2$	1.0 : 3.8 : 3.5	18 : 39 : 21 : 22
BSP13H	13 – 23	HAp	1.0 : 2.3 : 2.1	26 : 35 : 19 : 20
BSP490	49	–	0 : 1.1 : 1.0	0 : 47 : 26 : 27
BSP49Cl	49	$CaCl_2$	1.0 : 3.8 : 3.5	19 : 38 : 21 : 22
BSP49P	49	β-$Ca_3(PO_4)_2$	1.0 : 3.8 : 3.5	18 : 39 : 21 : 22
BSP49H	49	HAp	1.0 : 2.3 : 2.1	26 : 35 : 19 : 20
BSP890	89 – 98	–	0 : 1.1 : 1.0	0 : 47 : 26 : 27
BSP89Cl	89 – 98	$CaCl_2$	1.0 : 3.8 : 3.5	19 : 38 : 21 : 22
BSP89P	89 – 98	β-$Ca_3(PO_4)_2$	1.0 : 3.8 : 3.5	18 : 39 : 21 : 22
BSP89H	89 – 98	HAp	1.0 : 2.3 : 2.1	26 : 35 : 19 : 20

4.3. Characterization of the hybrid aerogels

4.3.1. Characterization strategy

Various characterization techniques were employed to obtain a comprehensive understanding of the structure of the newly synthesized BSPXY hybrid aerogels, as well as the structural changes that occur when the molecular weight of the PVA and/or the incorporated Ca(II) source are altered. The focus of these experiments is to identify the following key material characteristics related to the potential biomedical application of the aerogels.

- Chemical composition
- Morphology
- Homogeneity of the hybrid backbone
- Properties of the incorporated Ca(II) sources
- Potential morphological changes during wetting

- ζ-potential of suspended aerogel microparticles

The chemical composition of the aerogels was investigated using Fourier-transform infrared spectroscopy (FT-IR) and solid-state Nuclear Magnetic Resonance (ssNMR) spectroscopy. FT-IR spectroscopy provides qualitative information on the functional groups in the gel backbone, allowing the identification of the main functional groups.[103] Solid state NMR spectroscopy provides information on the chemical structure of the solid backbone and the three-dimensional arrangement of the structural elements.[104] The NMR transition frequencies are influenced by the surrounding electron distribution, which shields the nucleus from the external magnetic field, thereby revealing the chemical structure of the sample. The principles governing nuclear spin interactions, and the influence of magnetic fields and radiofrequency pulses are the same in both solid-state and liquid-state NMR. However, due to the orientation dependence of nuclear spin interactions in solids, most high-resolution solid-state NMR spectra are obtained using magic-angle spinning (MAS).[104] ssNMR spectroscopy offers both qualitative and quantitative insights into the chemical composition of the gel backbone. By applying specific excitation frequencies for selected nuclei, the different chemical environments of those nuclei can be explored.[104] In this study, ^{1}H, ^{11}B, and ^{29}Si MAS NMR measurements were performed to gather information on the chemical bonds associated with these nuclei. Quantitative ssNMR measurements were carried out for ^{11}B and ^{29}Si to determine the ratios of the various chemical bonds.

The morphology of the aerogels was investigated using scanning and transmission electron microscopy techniques (SEM and TEM) along with N_2 adsorption-desorption porosimetry. SEM images provide visual information on the 3D structure of the gel backbone at the nanometer scale, while TEM images offer insights into the substructure of the nanoparticles forming the

backbone, as well as any additional phases incorporated in them.[2] Energy-dispersive X-ray spectroscopy (EDS) elemental maps were also recorded using the TEM instrument in scanning mode to analyze the additional phases, such as the size and location of the incorporated calcium sources. N_2 adsorption-desorption porosimetry provides information on the pore size distribution in the mesopore range, as well as the pore volume and specific surface area of the aerogels.[2, 105] Together, these methods offer a comprehensive characterization of the aerogel morphology.

The characteristics of the incorporated Ca(II) sources were investigated using chemical elemental analysis, X-ray diffraction (XRD), and elemental mapping with TEM. To determine the amount of incorporated Ca(II) sources, the aerogel backbones were first digested in a harsh chemical environment, and the Ca(II) content was then measured by inductively coupled plasma optical emission spectrometry (ICP-OES). XRD measurements were performed on both the raw Ca(II) sources and the incorporated ones to gain information on their crystalline structure.

Small-angle neutron scattering (SANS) is a quantitative and non-destructive method for structural analysis in the nanometer range. The fundamentals of this method are described in Section 3.6. SANS measurements were carried out on dry and water-filled samples. By comparing the scattering curves of the dry and wet samples, the wetting induced potential morphological changes were studied. Contrast variation measurements were performed to investigate the homogeneity of the Ca(II)-free hybrid backbone using a mixture of H_2O and D_2O in varying ratios to fill the pores. These contrast variation measurements were also conducted on Ca(II)-containing samples to study the contribution of the Ca(II) sources to the scattering curves.

In aqueous media, ions are adsorbed onto the surface of solid particles, forming a diffuse electrostatic double layer. Localized, non-mobile ions are

found at the surface, while ions with the opposite charge accumulate near the surface. The density of these ions decreases as the distance from the surface increases, and the ions become more mobile farther from the surface. Under the influence of an electrostatic force field or mechanical force, the diffuse double layer separates. The potential difference between the slipping plane and the interior of the medium is known as the electrokinetic or ζ-potential.[1] The ζ-potential also serves as an indicator of colloid stability. In our case, this colloid property influences the interactions between the suspended aerogel particles and cells. To study this effect, the ζ-potential of the aerogel particles was measured in the pH range from 3 to 8.

4.3.2. Infrared spectroscopy (FT-IR)

The infrared spectra of the BSPXY aerogels were measured with a Perkin Elmer Spectrum Two FT-IR Spectrometer using a universal ATR head (Single Reflection Diamond – L1600607). The measurements were performed on powdered samples that were pressed onto the diamond surface. The IR spectra of the samples were recorded using 8 scans in the range of 550 – 4000 cm^{-1}.

4.3.3. Solid-state NMR spectroscopy (ssNMR)

Solid-state NMR spectroscopy (ssNMR) measurements were performed by Dr. Andraž Krajnc of the Slovenian National Institute of Chemistry.

A 600 MHz Varian spectrometer equipped with a 3.2 mm HX magic-angle spinning (MAS) probe was used to collect the ssNMR spectra. All experiments were conducted under a MAS frequency of 20 kHz. The specific Larmor excitation frequencies for the observed nuclei, namely ^{1}H, ^{11}B, and ^{29}Si, were 599.335 MHz, 192.293 MHz, and 119.059 MHz, respectively. The ^{1}H spectrum was acquired using a 2.8 μs pulse, followed by a 5.6 μs echo and

a recycle delay of 5 s. For the ^{11}B and ^{29}Si spectra, direct detection was employed. A single pulse with a width of 1.0 μs was used for ^{11}B, accompanied by a recycle delay of 2 s. Similarly, a 2.65 μs pulse width was applied for ^{29}Si, with a recycle delay of 60 s. A ^{1}H-^{29}Si cross-polarization magic-angle spinning (CPMAS) experiment was performed using a 3.0 μs single pulse to excite the ^{1}H nuclei, followed by a 5.0 ms contact time for polarization transfer to the ^{29}Si nuclei. The recycle delay for this experiment was set at 1.5 s. Finally, a two-dimensional ^{1}H-^{11}B cross-polarization heteronuclear correlation (CP-HETCOR) experiment was performed. A 2.0 μs pulse was used to excite the protons, immediately followed by a 1.0 ms contact time to transfer polarization to the ^{11}B nuclei. Along the indirect dimension (^{1}H), 20 increments and 1760 scans were employed, with a recycle delay of 1.5 s for each iteration.

4.3.4. Scanning electron microscopy (SEM)

The morphology of the aerogels was studied by low voltage scanning electron microscopy (LV SEM). A Thermo Fisher Scientific Scios 2 instrument with low accelerating voltage and low electron beam current was used to eliminate the charging effect of aerogel samples.[106] The measurement conditions made it possible to take images of the fresh fracture surfaces of the aerogels in their pristine states. Only a vacuum-resistant carbon tape was used to fix the aerogels, but no further sample preparation was performed.

4.3.5. Transmission electron microscopy (TEM)

The microstructure was studied by transmission electron microscopy (TEM) including high resolution TEM (HR-TEM) using a CS corrected Thermo Fisher Themis TEM instrument (Thermo Fisher Scientific, Waltham, MA, USA). The analysis was performed at 200 kV accelerating voltage with a point resolution of 0.08 nm. Energy dispersive X-ray spectroscopy (EDS)

elemental maps were recorded in scanning transmission electron microscopy (STEM) mode to study the incorporation and distribution of the Ca(II) source within the aerogel backbone.

4.3.6. N_2 adsorption-desorption porosimetry

N_2 adsorption-desorption isotherms were recorded in a Quantachrome Nova 2000e instrument at 77 K. Powdered aerogel samples (20–30 mg) were used to ensure reliable measurements. First, the samples were degassed under vacuum at 90 °C for 24 h before the measurements. Based on the measured isotherms, the apparent specific surface area, the pore size distribution, and the pore volume of the aerogels were calculated using NovaWin 11.0 software. The p/p_0 = 0.05 – 0.30 range was used as input data for the multi-point BET method for calculating the apparent surface area. The pore size distribution and the pore volume were determined by the NL-DFT method using the instrument controlling software and a built-in kernel developed for silicas with cylindrical pores.

4.3.7. Elemental analysis

Elemental analysis was performed to determine the Ca(II) content of the aerogels. First, the digestion of the aerogel was carried out as following. A mixture of 5.00 mL of 69 w/w% HNO_3 and 1.00 mL of 30% H_2O_2 solutions was added to 10.0 mg powdered sample. The reaction mixture was heated in a Milestone EHTOS UP high-power microwave digestion system to 200 °C in 15 min, and kept at high temperature for another 15 min. After cooling, the digested samples were brought to 25.0 mL final volume by ultrapure water. The gel residues were first removed by centrifugation then the supernatant was filtered through a 0.2 μm PVDF syringe filter to ensure separation.

The Ca(II) content was measured by ICP-OES technique using an Agilent 5100 Synchronous Vertical Dual View (SVDV) spectrometer. Five-point matrix fitted calibration was applied, diluted from a 10000 mg/L standard solution (Scharlau). The intensities were measured at 317.933 and 422.673 nm. Measurements of each sample were repeated three times. The measurement parameters were as follows: read time: 5 s; uptake delay: 15 s; rinse time: 30 s; stabilization time: 10 s, viewing height: 8 mm, the nebulizer gas flow rate: 0.70 L/min, plasma gas flow rate: 12.0 L/min. SVDV viewing mode was applied. The concentrations of at least 3 parallel samples were averaged.

4.3.8. X-ray diffraction (XRD)

The crystallinity of the incorporated Ca(II) sources were studied by X-ray diffraction (XRD) measurements. The diffraction patterns were collected under Cu-Kα radiation (Kα1= 1.54059 Å) using a Rigaku SmartLab 9.0 kW X-ray diffractometer (XRD). The measurements were carried out in Bragg-Brentano geometry, between 20 and 55 (2θ) with 5.0 degree/min scan rate.

4.3.9. Small-angle neutron scattering (SANS)

Neutron scattering measurements at small angles were realized using the Yellow Submarine pin-hole-type SANS instrument at the Budapest Neutron Centre.[107] The powdered, solid samples were introduced into 2.0 mm thick quartz cuvettes and no further sample treatment was used. To perform the wetting and contrast variation measurements, the samples were filled with H_2O:D_2O mixtures in the same cuvettes. The aqueous mixture completely covered the samples filled in the cuvettes, then they were gently sonicated in a bath type sonicator and stored for 24 h for equilibration. The amount of liquid used was sufficient to ensure that the pores and the spaces between the aerogel particles were completely filled, without leaving excess liquid that would cause

the particles to settle. First, the wet samples were measured to get information on the structural changes occurring during the interaction with water. In a second step, contrast variation method was used to highlight the possible inhomogeneities (PVA and Ca source) of the samples. For calibration, measurements were also taken for the empty beam, the transmission of the samples, the empty cuvette, and water (H_2O) with a 1 mm thickness in the cuvette.

By changing the wavelength of the incoming neutron beam and the sample-to-detector distance, a momentum transfer (Q) range of 0.0055 – 0.370 $Å^{-1}$ was covered (eq. 4.).

The data evaluation was performed using the BerSANS free software.[108] The measured 2D scattering intensities of the samples on the detector showed isotropic scattering in every case. The measured scattering intensity was corrected for sample transmission, empty cell scattering and detector sensitivity. Due to the ambiguity of determining the exact amount of material within the irradiated volume, the scattering curves are not calibrated in an absolute manner. Despite this, the scattering curves still provide valuable structural information on the aerogel samples.

The SANS curves were modelled by the Beaucage model, which is the combination of Guinier and power-law approximations.[100, 101] The first (eq. 16) or second level (eq. 17) Beaucage models were used to cover the entire experimental Q range depending on the morphologies of the different aerogels.

$$I(Q) \cong G_1 \exp\left(-\frac{Q^2 R_{g1}^2}{3}\right) + B_1 \left\{ \frac{\left[\operatorname{erf}\left(\frac{Q R_{g1}^2}{\sqrt{6}}\right)\right]^3}{Q} \right\}^{p_1} + \mathrm{C} \qquad (16)$$

$$I(\mathrm{Q}) \cong G_1 \exp\left(-\frac{Q^2 R_{g1}^2}{3}\right) + B_1 exp\left(-\frac{Q^2 R_{g2}^2}{3}\right)\left(\frac{\left[erf\left(\frac{QR_{g1}}{\sqrt{6}}\right)\right]^3}{Q}\right)^{p_1}$$

$$+ G_2 \exp\left(-\frac{Q^2 R_{g2}^2}{3}\right) + B_2\left(\frac{\left[erf\left(\frac{QR_{g2}}{\sqrt{6}}\right)\right]^3}{Q}\right)^{p_2} + C \qquad (17)$$

The mean size of the scattering objects was calculated from the gyration radius assuming spherical geometry using equation (10). Data fitting was performed using the non-linear Levenberg-Marquardt least-squares algorithm in the SasView 5.0.5 open-source software. The resulting fits showed a χ_r^2 between 1 and 2.5 in every case.

4.3.10. Particle size distribution of hydrated BSP130

An aqueous suspension (1.0 mg/mL) of powdered BSP130 sample, without pH adjustment, was prepared. The suspension was gently mixed for 20 minutes, followed by sonication for an additional 20 minutes. After treatment, images of the suspension were captured using a 1.3 MP USB microscope camera, and the particle size distribution was analyzed with ImageJ software (National Institutes of Health).

Initially, the images were converted to 8-bit format, and the signal-to-noise ratio was enhanced by applying stack deflickering to reduce transient brightness variations. Further processing included dynamic contrast adjustment, background homogenization through Fourier transform bandpass filtering, histogram equalization, and background subtraction to improve visibility. Particle contours were smoothed using the Gaussian blur function to ensure uniformity. Segmentation was performed using thresholding to

differentiate the foreground (particles) from the background, enabling quantitative analysis.

This procedure aimed to estimate the particle sizes of aerogel fragments formed during biological measurements, as the original particles disintegrate during these investigations.

4.3.11. ζ-potential

Aqueous suspensions (1.0 mg/ml) were prepared from the pristine aerogel samples using a Potter-Elvehjem tissue grinder to achieve small gel particles, which are beneficial for electrophoretic mobility measurements. The pH of the suspensions was adjusted by adding HCl or NaOH. The ζ-potentials of the suspensions were determined between pH = 3.0 and 8.0 using a MALVERN Zetasizer Nano ZS instrument. Conventional instrument setup and operation were used after the auto-adjustment of the measurement parameters. The ζ-potential values were calculated from the measured electrophoretic mobility by the instrument controlling software based on the Smoluchowski approximation.

4.4. Biological tests of the hybrid aerogels

Dr. Gábor Szemán-Nagy and his research team at the University of Debrecen conducted *in vitro* biological experiments on BSP49Y samples containing Ca(II) sources.[90] Dental pulp stem cells (DPSCs) were cultured in DMEM-F12 medium (iBiotech, Szigetszentmiklós, Hungary) supplemented with 10% fetal bovine serum (FBS) and 1% antibiotic-antimycotic mix (Penicillin–Streptomycin–Neomycin). Similarly, human bone osteosarcoma cells (MG-63) were cultured in DMEM medium (iBiotech) under identical supplement conditions. Both cell types were incubated at 37°C with 5.0% atmospheric carbon dioxide. For different experimental setups, cells were

grown to either 20% or 100% confluence. To achieve 20% confluence, cells were plated at 15,000 cells/cm^2 in glass-bottom dishes and incubated overnight. Scratch assays were performed once the cultures reached full confluence (100%).

Time-lapse video microscopy experiments were carried out using a modified SANYO MCO18-AC CO_2 incubator (Wood Dale, IL, USA), equipped to accommodate up to four microscopes. Olympus upright microscopes (Tokyo, Japan) were repurposed for inverted use, and revolver turrets were added to replace the original light source. Custom high-sensitivity imaging was achieved with Carl Zeiss (Jena, Germany) ×10 plan achromatic objectives (0.25 NA) and KPC EX-20H high-resolution cameras (KT&C, Seoul, Korea) featuring Sony ExView CCD sensors. Illumination was provided by 940 nm near-infrared LED diodes to minimize heat and phototoxicity, ensuring deeper light penetration and reduced dispersion. Images were collected every 5 seconds, with 10 frames averaged at each time point to reduce noise.

Captured image sequences were analyzed using ImageJ software similarly as described in Section 4.3.10.

4.5. Background information on the calcium alginate aerogel

In a recent study, a qualitative model was developed to describe the wetting mechanism of an archetypical calcium alginate aerogel formulation using a combination of complementary characterization techniques, including SANS. The study identified critical water contents where the physico-chemical properties of the hydrated aerogel change abruptly. However, the quantitative description of the structural changes were not condensed into a mathematical model.[5]

In Section 7 of the Results and Discussion chapter, we describe our new mathematical model used for quantitatively analyze the SANS patterns of the partially hydrated calcium alginate aerogel samples to obtain information on the hydration-induced structural changes that occurred during the wetting. The following sections describe the main characteristics of the investigated calcium alginate aerogel, along with the experimental details of its controlled hydration and wetting for the measurements.

4.5.1. The synthesis of the calcium alginate aerogel and its main structural properties

The synthesis of spherical calcium alginate beads was carried out using a jet-cutting method. First, a 1 w/w% Na-alginate (Sigma; catalogue no. 71238; β-D-mannuronate (M) and α-L-guluronate (G) mole fraction: 0.52:0.48) aqueous solution was prepared and then added dropwise into a 20 g/L $CaCl_2$ solution using a commercial JetCutter (Type S from geniaLab GmbH, Braunschweig, Germany). The volume of the $CaCl_2$ solution was significantly higher than that of the Na-alginate solution to ensure that all binding sites were occupied by Ca^{2+} ions, i.e., the ratio of carboxylate groups to Ca^{2+} ions was stoichiometric in the formulated gels. The gelling bath was moderately stirred to prevent aggregation of the forming spherical beads. After gelation, a multi-step solvent exchange was performed. Initially, the beads were placed in a 30-70 w/w% ethanol-water mixture. The ethanol content was then increased by 30 w/w% twice, followed by soaking the gels twice in absolute ethanol. Each solvent exchange step lasted for 24 hours. Finally, the alcogels were dried under supercritical conditions using CO_2. The resulted aerogel samples (ca. 0.2 mm in diameter) were stored in a desiccator filled with freshly dried silica gel (desiccant) to avoid contact with humidity.[5]

The structure of the dry aerogel was investigated using SEM and N_2 porosimetry measurements, as described earlier. The pore size distribution and total pore volume (within the measured pore range) were calculated using the BJH method, as no specific kernel for alginate was available for the NL-DFT method.

Figure 7 shows the SEM images and pore size distribution of the calcium alginate aerogel. The aerogel exhibits a fibrillar structure on the nanometer scale with mesopores primarily 42 nm in diameter, with a standard deviation of 11 nm. The structural parameters of the calcium alginate aerogel are presented in **Table 2**.[5]

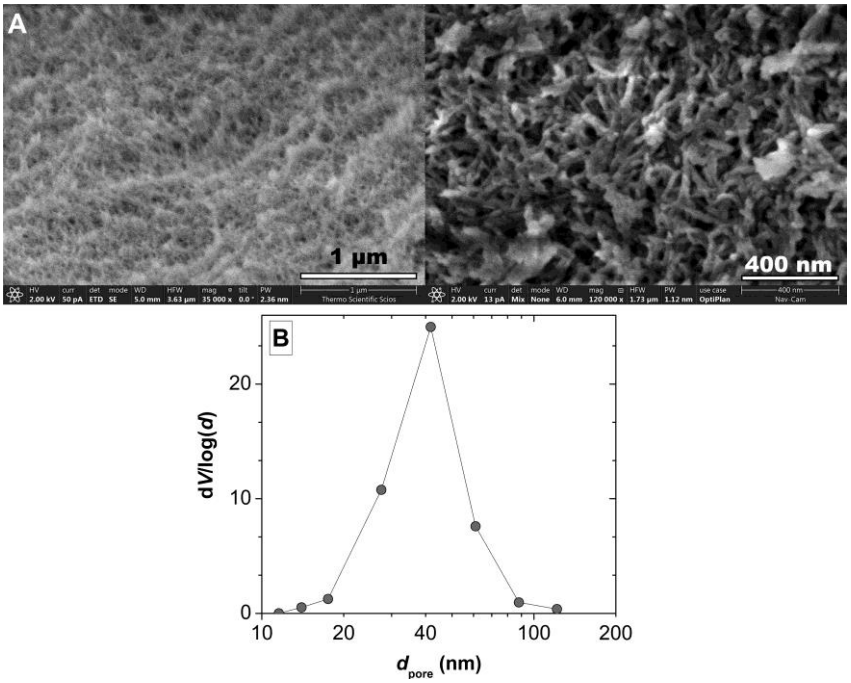

Figure 7. Panel A: Low voltage scanning electron microscopy (LV-SEM) images of the dry calcium alginate aerogel at different magnifications (**left:** 35K×; **right:** 120K×). **Panel B:** Pore size distribution of calcium alginate aerogel calculated from the desorption isotherm of the N_2 adsorption−desorption porosimetry data by using the BJH method.[5]

Table 2. Structural parameters of the calcium alginate aerogel by N_2 adsorption-desorption porosimetry data.[5]

Parameter	Value	Evaluation
Specific surface area (m^2/g)	544 ± 70	BET
Pore diameter (nm)	42 ± 11	BJH
Total pore volume (cm^3/g)	7.5 ± 0.2	BJH

4.5.2. Controlled hydration of the calcium alginate aerogel

Sample preparations were performed starting with a dry calcium alginate aerogel, gradually increasing its water content by adding drops of water up to 2.0 mg of water per 1.0 mg of the dry sample. The water content is defined as the grams of water added per gram of dry aerogel (g/g). After adding varying amounts of water to approximately 100 mg of aerogel, the samples were gently mixed and sonicated for 3 minutes in a sonicator bath. Each sample was prepared in its respective sample holder and sealed airtight for a 24-hour equilibration period before measurements.[5]

The SANS measurements were conducted at the Budapest Neutron Centre using the 'Yellow Submarine' instrument, the same instrumental setups as described in Section 4.3.9. The only difference is a slight change in the measured Q range (0.0065−0.40 $Å^{-1}$), due to the altered wavelength.

5. Structural characteristics of the borosilicate – PVA hybrid aerogels

5.1. Chemical composition

5.1.1. Infrared spectroscopy (FT-IR)

The FT-IR spectra of BSP490 and a pure silica aerogel, and the FT-IR spectra of BSPX0 and BSP89Y aerogels are shown on **Fig. 8.**

In general, the characteristic peaks of Si-O-Si, Si-OH, B-O, C-H and B-O-C bonds appear in the case of all BSPXY aerogels. The characteristic vibration of the OH group can be observed as a broad band between 3690-3000 cm^{-1}, which is specifically attributed to the SiO-H, BO-H and CO-H stretching vibrations.[103, 109, 110] The Si-O in-plane stretching vibration, which is characteristic for the Si-OH group, can be observed at around 960 cm^{-1}. A very intensive and broad band can be observed in the range of 1270-985 cm^{-1}, which is characteristic to the asymmetric Si-O-Si stretching vibrations. The symmetric stretching vibration of Si-O-Si occurs around 800 cm^{-1}.[103, 109]

The peak at around 665 cm^{-1} refers to the B-O bending vibration. [103, 111, 112] The bands in the range of 1200-1000 cm^{-1} are attributed to the antisymmetric [BO_3] and [BO_4] stretching vibrations that overlap with the Si-O-Si band.[111, 112] The peak at around 1282 cm^{-1} is characteristic for the stretching vibration of B-O-C bond, indicating complex formation between boric acid and PVA.[113, 114] The presence of Si-O-B bonds typically yield a peak at ca. 890 cm^{-1}, but it is not visible in the case of any of the hybrid aerogels.[89, 115]

The peaks in the range of 3000-2900 cm^{-1} are associated with the stretching vibrations of the C-H alkyl groups from PVA. [103, 110] The peaks in the range of 1700-1720 cm^{-1} and 1370-1380 cm^{-1} (appearing as a shoulder) can be attributed to the stretching vibration of the C=O bonds and the

deformation vibration of CH_3 groups, respectively. These peaks indicate the presence of acetate groups remaining in the incompletely hydrolyzed PVA molecules.[103, 110, 116] They are observed in the spectra of BSP13Y and BSP49Y aerogels, but not in the case of the BSP89Y aerogels (PVA 99% hydrolyzed). The peak around 1420 cm^{-1} is characteristic for the superposition of the deformation vibrations of the OH groups and the CH_2 groups of PVA.[103, 116] The peak at around 1335 cm^{-1} corresponds to the deformation vibration of CH groups.[4]

In the case of aerogels containing HAp, an additional peak appears at 604 cm^{-1}, which belongs to the PO_4^{3-} ν4 vibrational mode.[117, 118] Additional absorption bands appear in all cases in the range of 1660-1600 cm^{-1} due to presence of adsorbed water.[103, 119]

As a summary of the FT-IR spectroscopy results, the characteristic peaks corresponding to the chemical bonds of the individual components of the backbone are detectable. However, covalent bond formation between the individual components is only observed between boric acid and PVA, attributed to complex formation. Covalent bond formation between other components cannot be identified based on these measurements. To further investigate the interactions between these components, ssNMR was utilized.

FT-IR provides no information on the incorporation of $CaCl_2$; however, in the case of HAp, the presence of PO_4^{3-} is detectable. For β-$Ca_3(PO_4)_2$, the signal of PO_4^{3-} is also expected to appear, but the peak is less intense, making it difficult to detect. This difference in peak intensity can be explained by the large difference in the Ca(II) source content, as discussed later.

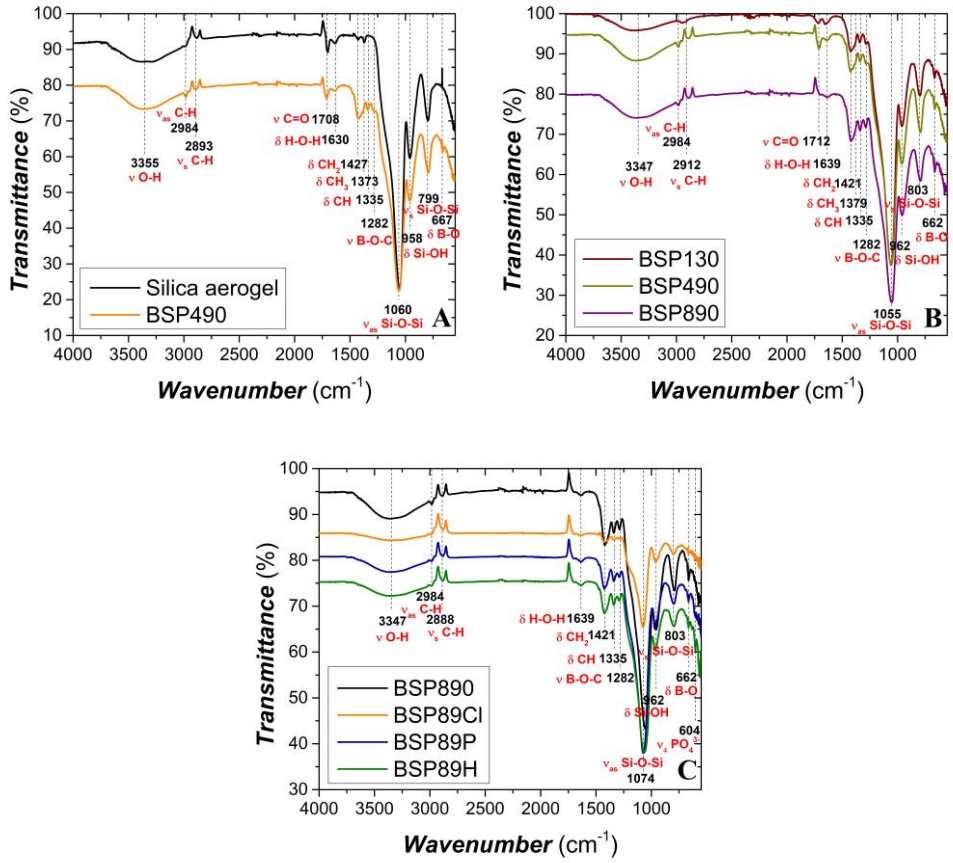

Figure 8. Infrared spectra (FT-IR) of hybrid borosilicate-PVA and silica aerogel samples. The specific aerogels are identified in the legends. **Panel A:** Comparison of pristine silica aerogel and the BSP490 aerogel. **Panel B**: The effect of different PVA sources. **Panel C:** The effect of different Ca(II) sources.

5.1.2. Solid-state NMR spectroscopy (ssNMR)

In order to understand the complicated structural characteristics of the hybrid aerogels at the molecular level, quantitative solid state ^{29}Si-, ^{11}B- and ^{1}H-NMR measurements were performed. Each measurement is discussed in detail in the following paragraphs.

The ^{29}Si MAS NMR and ^{1}H-^{29}Si CPMAS NMR spectra of the BSPXY aerogels are shown in **Fig. 9.** Three peaks were identified for all hybrid aerogels, corresponding to the Q_2 (~ -91.3 ppm), Q_3 (~ -100.6 ppm) and Q_4

sites (~ -110 ppm). The Q_x sites are defined based on the number of bridging oxygen atoms surrounding a silicon atom, with the general structure $Si(OSi\equiv)_x(OR)_{4-x}$, where R=H or alkyl group (in our case CH_2CH_3).[119] The chemical structures of the Q_x sites are shown in **Fig. 9.**

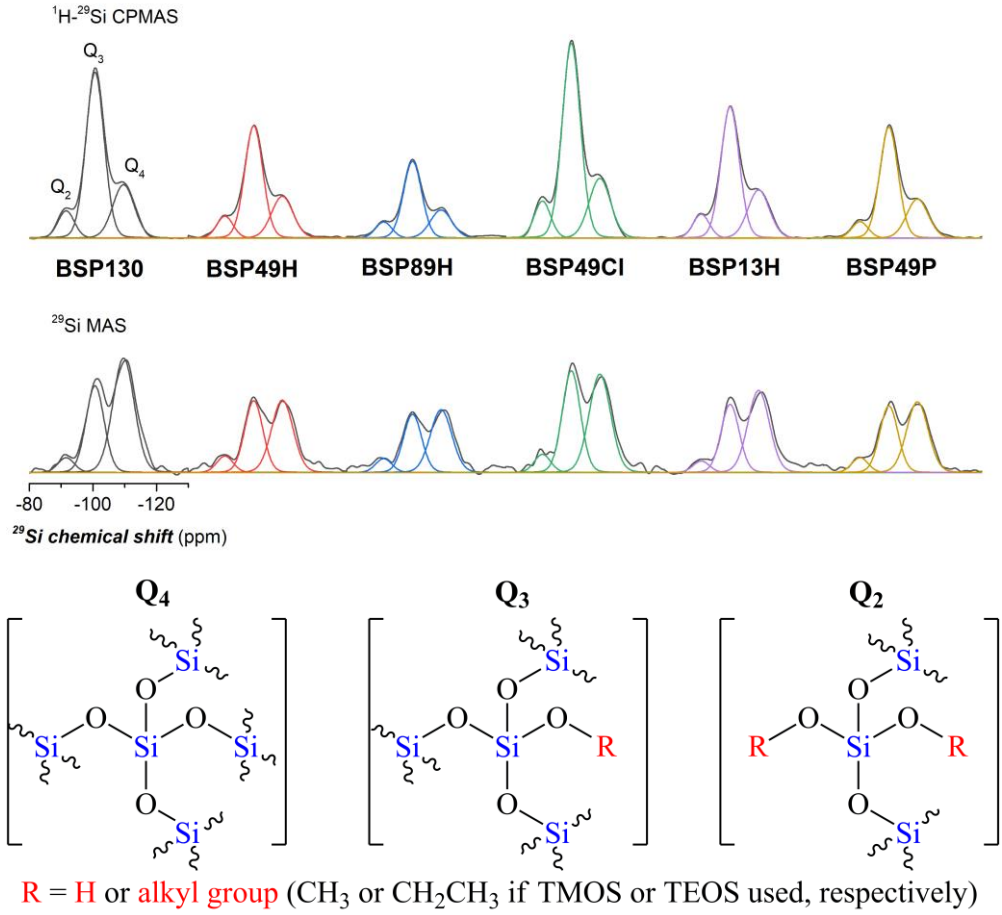

Figure 9. ^1H-^{29}Si CPMAS (**top**) and ^{29}Si MAS (**middle**) NMR spectra of BSPXY aerogels, and the chemical structures of Q_x sites (**bottom**).

Multiple peaks within the different Q_x sites are not observed, suggesting no significant variation in the chemical environment of these sites due to different R groups. According to the literature, the peaks observed at -91.3 ppm and -100.6 ppm for the Q_2 and Q_3 sites are characteristic of

$Si(OSi\equiv)_x(OH)_{4-x}$ groups.[120] The integrals of the individual peaks are calculated from ^{29}Si MAS NMR spectra and are proportional to the quantities of the corresponding structural elements. The sum of the Q_2 and Q_3 sites represents the number of Si atoms with at least one connected OH group, indicating the free OH content in the silica network. The three-dimensional (3D) network structure is corresponding to the sum of Q_3 and Q_4 sites, while the Q_2 site gives information on the two-dimensional (2D) structure. The ratios of the Q sites, and the presence of the free OH groups of the silica network in the BSPXY aerogels are shown in **Fig. 10.**

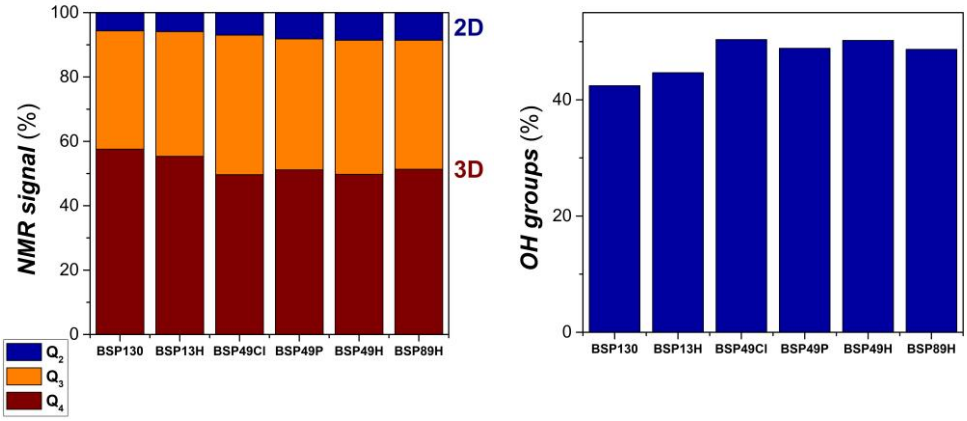

Figure 10. Left panel: 3D (Q_3 and Q_4 sites) and 2D (Q_2 site) ratio of the silica network along with the ratio of Q_2, Q_3 and Q_4 peak intensities. The Q_2, Q_3 and Q_4 sites are identified in the legends. **Right Panel:** The presence of the free OH groups of the silica network in the case of different BSPXY aerogels.

The largest proportion of the Q_4 sites and 3D structural elements is observed in the case of BSP13Y samples, which also means that these aerogels have the least free OH groups. The longer PVA chains cause a slight decrease in the Q_4 contribution, while the incorporation of different Ca(II) sources do not significantly alter the ratio of the 2D and 3D structural elements. However, it has to be mentioned that the Q_4 contribution is slightly lower in the case of BSP13H compared to BSP130. As a conclusion, the lowest molecular weight

PVA (13 kDa) allows a more complete condensation for the silica network compared to the higher molecular weight PVAs. In every case, the ratio of the sites with at least one -OH group is in the range of 40-45%.

An important question is whether covalent bonds form between the silica and the PVA components during the reactive gelation or not. An NMR peak would be expected at ca. 60 ppm in the spectra of the hybrid aerogels as an indication of Si-O-C bonds. In our case, this peak cannot be detected in any of the samples, which means that there is practically no covalent bonding between the silica network and the PVA.[119]

The ^{11}B-MAS spectra are shown in **Fig. 11.** Two peaks were detected in every case, and the ratio of these peaks is also given in **Fig. 11**. The first signal in the range of 10-18 ppm is assigned to the trigonal BO_3 moiety, while the other one at around 0 ppm is assigned to the tetrahedral BO_4 structural element.[89, 121, 122] The BO_3 peak is made up of several signals corresponding to cyclic and non-cyclic BO_3 structures. The peak around 18 ppm is characteristic for boron in rings, while the peaks at smaller chemical shift are characteristic for non-cyclic structures.[89, 121]

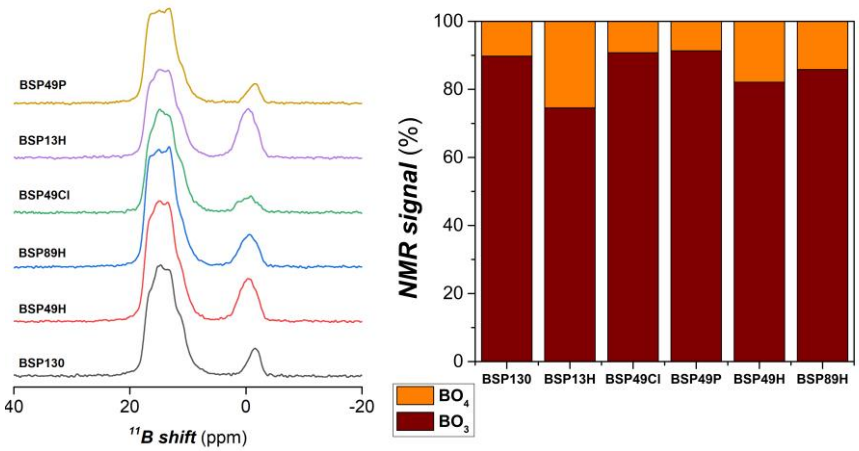

Figure 11. Left panel: The ^{11}B-MAS spectra of BSPXY aerogels. **Right panel:** The ratio of BO_3 and BO_4 intensities.

The integral of the BO_3 peaks is higher in every case than the integral of the BO_4 peak. The amount of the BO_4 units is the highest for BSP13H samples. According to the literature, the Ca^{2+} content can stabilize the BO_4 units in the gel structure during the reactive gelation.[89, 123] Based on the elemental analysis (detailed in Section 5.3.1.), the highest calcium concentration is in the BSPXH aerogels. Comparing the BSPXH samples, the intensity of the BO_4 peak slightly decreases as the molar mass of the PVA increases. This phenomenon can be interpreted as the fact that the longer PVA chains partly cover the hydroxyapatite particles and thus prevent the binding of Ca^{2+} ions on the BO_4 structural units.

The appearance of BO_4 groups may also result from boric acid forming complexes with PVA, reinforcing the likelihood of B–O–C bond formation.[124] However, BO_4 groups are also observed in borosilicate glasses without PVA or Ca^{2+}, indicating that the formation of BO_4 structures can arise from multiple factors.[125]

According to the literature, a ^{11}B-MAS peak around 13 ppm would indicate the presence of B-O-Si bonds. However, not even the IR spectra show a peak around 890 cm^{-1}, which could confirm the presence of such a bond.[89, 115] The apparent absence of these types of bonds can be explained by the fact that the formation of B-O-Si bonds is not favorable at room temperature, and they are sensitive to hydrolysis.[126, 127]

The ^{1}H-NMR spectra and the ^{1}H–^{11}B HETCOR 2D NMR spectrum are shown in **Fig. 12.**

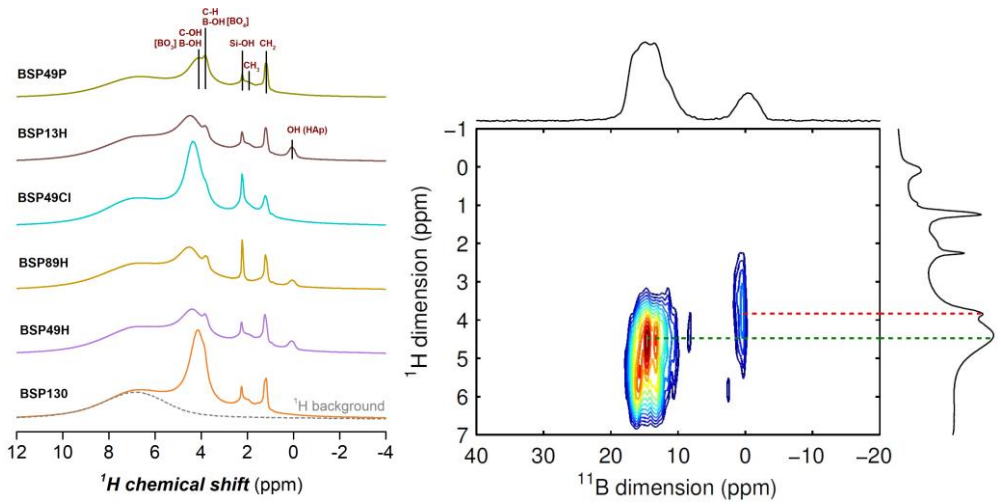

Figure 12. Left panel: ^{1}H-MAS spectra of BSPXY aerogels. **Right panel:** ^{1}H-^{11}B HETCOR 2D NMR spectrum for BSP49H.

The broad signal around 7 ppm is attributed to the adsorbed water on the surface of BSPXY aerogels.[119] The peak at 2.2 ppm is attributed to the Si-OH group.[119] According to the ^{1}H–^{11}B 2D NMR spectrum, the peaks at 4.2 and 3.8 ppm correspond to the B-OH groups of BO_3 and BO_4, respectively. The signals of C-OH and CH groups overlap with the B-OH peaks at 3.8 and 4.2 ppm. The peak at 1.4 ppm is assigned to the CH_2 group of the PVA, while the signal at 2.0 ppm is assigned to the CH_3 group of residual acetate.[128] An additional peak is observed for the BSPXH samples at 0 ppm, which is characteristic for the OH group of hydroxyapatite.[129]

To summarize the NMR results; the BSPXY aerogels show the characteristic features of a physical mixture of amorphous SiO_2 and B_2O_3 networks. According to the NMR data, covalent bonding cannot be detected between the SiO_2 and B_2O_3 parts. However, B–O–C bond formation due to the complexation of boric acid with PVA may occur. Evidence was provided that varying the molar mass of the PVA and changing the Ca(II) source do alter the structure of the hybrid aerogel backbone, but only to a slight extent.

5.2. Morphology

5.2.1. Scanning electron microscopy (SEM)

Representative SEM images of pristine BSP49Y and BSP89Y aerogels are shown in **Fig. 13.** The primary morphological characteristics of the hybrid aerogels in the absence of Ca(II) sources can be seen in the images of the BSPX0 samples. The fundamental morphological features of typical silica aerogels can be recognized in them.[56, 130, 131] The network shows an open and interconnected porous system made of primary spherical nanoparticles with a diameter of less than 10 nm. The pore sizes defined by the pearl-string like connection of the primary spherical nanoparticles are in the mesoporous region (<50 nm). The incorporation of the PVA into the gel backbone does not significantly alter the characteristic morphological features of the backbone. Even varying the molar mass of the PVA does not cause significant changes in the structure.

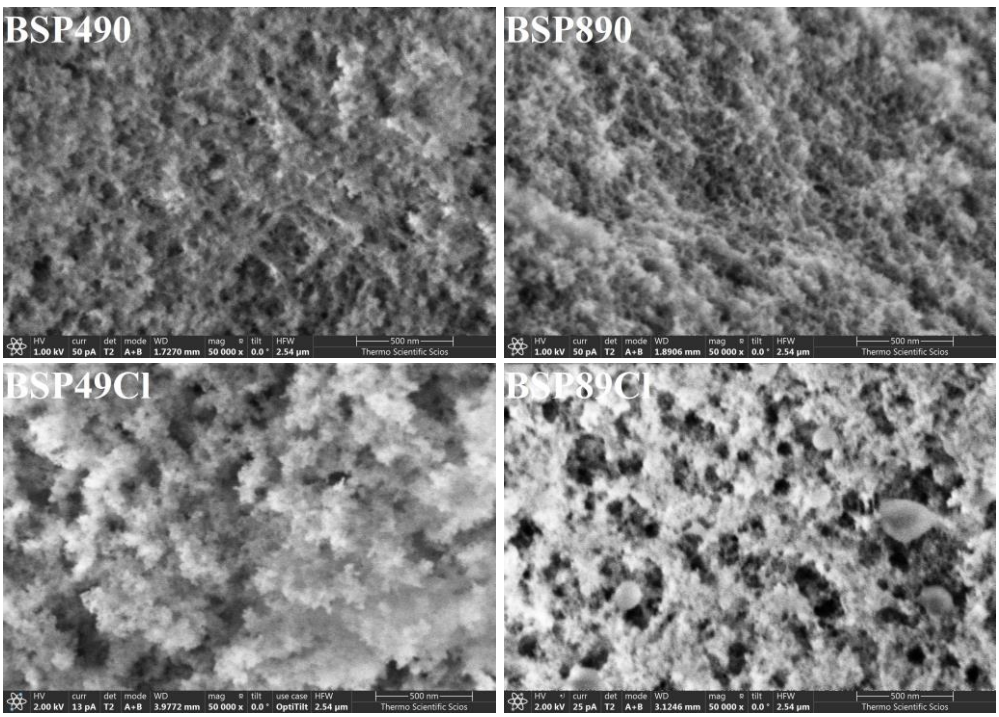

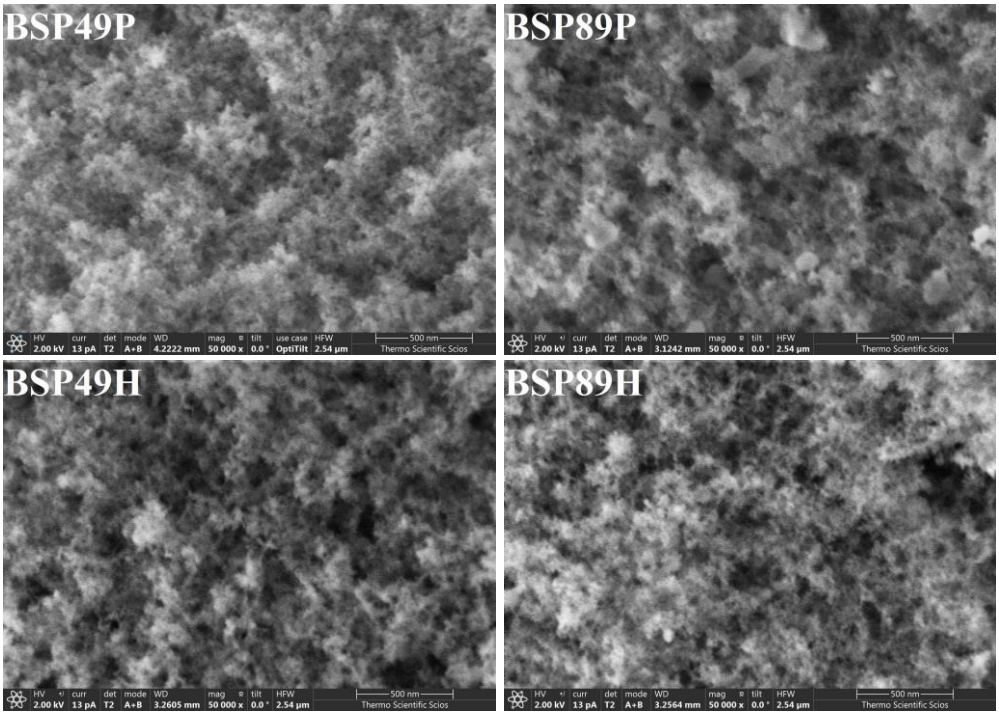

Figure 13. Low voltage scanning electron microscopy (LV-SEM) images of pristine aerogels in 50k × magnification**. Left column**: BSP49Y aerogels. **Right column:** BSP89Y aerogels.

The morphological changes associated with the incorporation of Ca(II) sources cannot be clearly identified from the SEM images. However, it is evident that the addition of $CaCl_2$ leads to the formation of larger aggregates compared to the other Ca(II) sources. These observations are valid for all BSPXY aerogels. Furthermore, aggregated polymer granules can be observed in the SEM images of BSP89Cl and BSP89P samples. These granules cannot be observed in the SEM images of other BSP89Y aerogels, but their existence cannot be ruled out. The formation of these polymer granules can be explained by the inadequate dissolution of the polymer.

Additionally, SEM images of the pristine β-$Ca_3(PO_4)_2$ and HAp compounds were taken, as shown in **Fig. 14.** These images clearly illustrate the morphological differences of the calcium compounds, along with the size distributions of the particles.

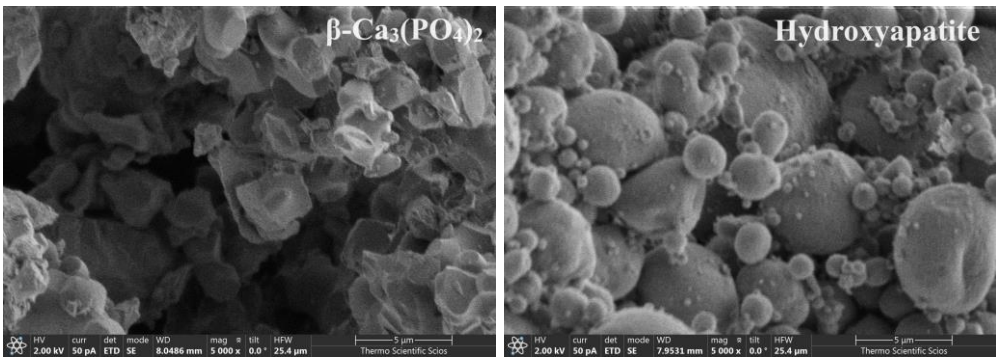

Figure 14. Low voltage scanning electron microscopy (LV-SEM) images of β-$Ca_3(PO_4)_2$ (**left**) and HAp (**right**) compounds in 5k × magnification**.**

5.2.2. Transmission electron microscopy (TEM)

The TEM images and the elemental maps of the BSP49Y aerogels are shown in **Fig. 15.** The backbone of the gel is built up by interconnected spherical particles that form a mainly mesoporous structure. The presence of calcium-rich parts in the EDS elemental maps confirm the integration of the Ca(II) sources to the aerogel backbones. The size of these calcium-rich parts are identical to the size of the Ca(II) compounds.

In BSP49Cl, the calcium-rich regions are in the nanometer range, whereas, for the other two samples, they are primarily in the micrometer range. This difference arises because $CaCl_2$ dissolves in the reaction mixture, altering its ionic strength. The solvated Ca^{2+} ions can act as gelation agents, promoting the formation of larger aggregates (as observed in the SEM images). During the gelation process, $CaCl_2$ is partially incorporated into the gel backbone, though the exact nature of this reaction warrants further investigation. However, since $CaCl_2$ is soluble in ethanol, which is used during the solvent exchange process, only a small fraction of the Ca(II) content remains in the final aerogel (detailed in Section 5.3.1). The incorporated Ca(II) likely exists in ionic form within the gel backbone, with some crystallizing as nanosized

particles into the pores, corresponding to calcium-rich regions. Additionally, the distribution of Cl differs from that of Ca in the gel backbone. This suggests that $CaCl_2$ is incorporated in a form other than its original state, potentially as CaO or $Ca(OH)_2$. However, proving this hypothesis would require further investigation.

In contrast, β-$Ca_3(PO_4)_2$ and HAp do not dissolve in the reaction mixtures and retain their original structures upon incorporation into the gel backbone.

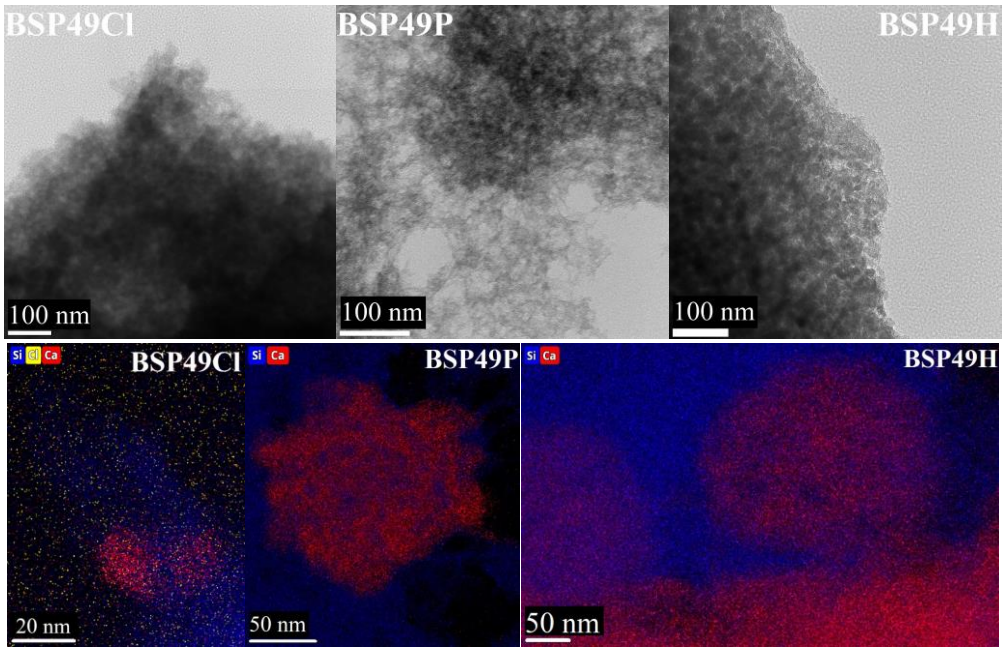

Figure 15. Upper panel: TEM images of the BSP49Y aerogels. **Lower panel:** Elemental maps of the BSP49Y aerogels.

5.2.3. N_2 adsorption-desorption porosimetry

The experimental isotherms and the calculated pore size distribution curves of the BSPXY aerogels are shown in **Fig. 16.** All samples exhibit IVa-type isotherms with H3 hysteresis loops. This type of isotherm is typical for

mainly mesoporous materials, which also contain macropores as described in the latest IUPAC technical report on the good practice of gas physisorption.[105]

Although all samples exhibit the same type of isotherm, the incorporation of different PVAs and Ca(II) sources alter the mesoporous systems of the aerogels, which is well reflected in the change of the pore size distribution and the total pore volume. The calculated morphological parameters are listed in **Table 3.**

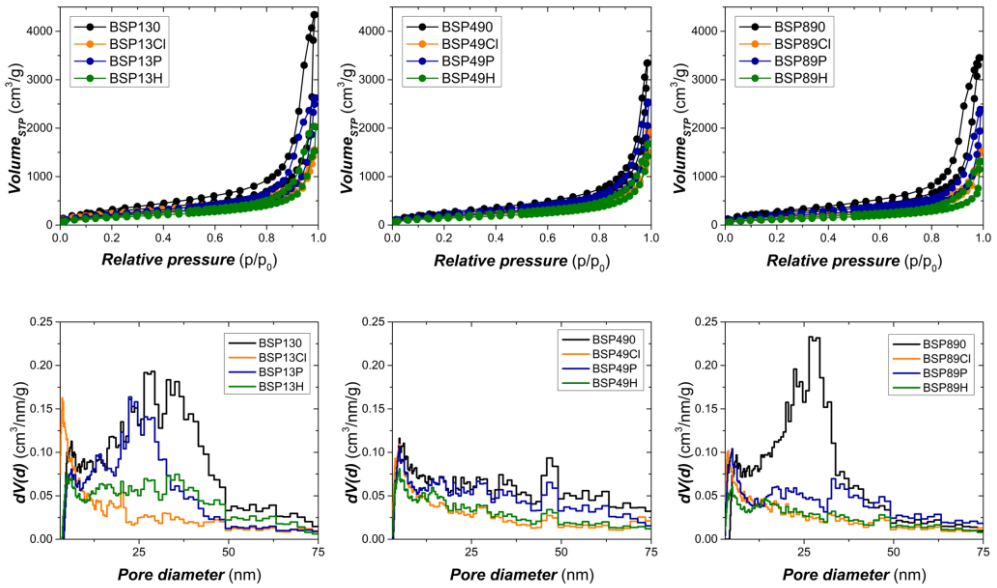

Figure 16. Nitrogen adsorption-desorption isotherms and pore size distribution curves of BSPXY aerogels. **First column:** BSP13Y aerogels. **Second column:** BSP49Y aerogels. **Third column:** BSP89Y aerogels.

The pore size distribution of BSP130 and BSP890 are similar, with characteristic pore diameters of 28 nm and 26 nm, respectively. The pore size distribution of BSP490 is also wide, but a decreasing trend in the distribution is observed, indicating that smaller pores contribute significantly to the pore structure. An increase in the molecular weight of PVA slightly reduces the surface area and pore volume of the aerogels. However, no clear trend is

observed as a function of increasing molecular weight, likely due to variations in the extent of PVA hydrolysis. Nevertheless, based on SEM and TEM images, no significant changes in morphology are detected.

The pore size distribution of the aerogels is also altered by the incorporation of Ca(II) sources, particularly in the case of the BSP13Y and BSP89Y aerogels. In general, all three Ca(II) sources cause the reduction of the surface area and pore volume of the aerogels compared to the Ca(II)-free samples with the same molar weight PVA. The apparent surface area decreases the most with HAp incorporation, and the least with β-$Ca_3(PO_4)_2$ incorporation. Conversely, the pore volume decreases most significantly with the incorporation of $CaCl_2$ and HAp, in a roughly similar manner, and the least with β-$Ca_3(PO_4)_2$.

Table 3. Morphological parameters of the pristine BSPXY aerogels calculated from the N_2-sorption porosimetry measurements.

Code name	Apparent surface area (m^2/g)	Characteristic pore diameter (nm)	Pore volume (cm^3/g)
BSP130	1038	28	6.1
BSP13Cl	763	4	2.0
BSP13P	747	22	3.7
BSP13H	579	5	3.0
BSP490	880	5	4.2
BSP49Cl	604	5	2.0
BSP49P	726	5	3.3
BSP49H	517	5	2.1
BSP890	949	26	5.0
BSP89Cl	593	4	1.8
BSP89P	665	5	2.9
BSP89H	417	5	1.7

These changes are attributed to differences in the incorporation levels and particle sizes of the various calcium compounds. On the one hand, the presence of calcium compounds slightly modifies the hydrolysis and polycondensation reactions, leading to minor nanostructural differences in the hybrid backbone. In the case of $CaCl_2$, it dissolves in the reaction mixture, which alters the ionic strength, leading to morphological changes such as the formation of larger aggregates, as observed in the SEM images. In contrast, HAp and β-$Ca_3(PO_4)_2$ retain their original forms during synthesis (see Sections 5.2.1. and 5.2.2.). Additionally, the incorporation of β-$Ca_3(PO_4)_2$ and hydroxyapatite leads to the partial blockage of the meso- and micropores, affecting the apparent pore size distributions. The difference between the HAp and the β-$Ca_3(PO_4)_2$ incorporated samples is explained by their varying particle size distributions (see Sections 5.2.1. and 5.2.2.) and differences in the amounts incorporated, as explained in the next section.

5.3. Ca(II)-content

5.3.1. Elemental analysis

The results of the elemental analysis of the BSP49Y, BSP13Cl and BSP89Cl aerogels are detailed in **Table 4**. The theoretically expected and measured Ca(II) contents are in good agreement in the case of BSP49P and BSP49H samples. However, the calcium content of BSP49Cl is significantly smaller than expected. The explanation is the same as described earlier. $CaCl_2$ dissolved in the reaction mixture, but only a small portion crystallized and integrated into the hybrid backbone. As expected, a similar trend was observed for all BSPXCl aerogels; the measured Ca(II) amounts are much smaller than expected.

Table 4. Ca(II) contents of BSP49Y and BSPXCl aerogels.

	BSP49Cl	**BSP49P**	**BSP49H**	**BSP13Cl**	**BSP89Cl**
Expected Ca(II) content (w/w%)	~7	~7	~10	~7	~7
Measured Ca(II) content (w/w)%	0.8 ± 0.1	7.5 ± 0.4	11.5 ± 0.5	1.08 ± 0.04	0.79 ± 0.02
Measured Ca(II) source content (w/w)%	2.1 ± 0.2	19.4 ± 0.9	28.8 ± 1.3	3.0 ± 0.1	2.2 ± 0.1

5.3.2. X-ray diffraction (XRD)

Fig. 17 shows the XRD spectra of the BSP49Y aerogels alongside those of the pristine calcium compounds. Their characteristic peaks were identified using the ICDD-PDF data.

The pattern of BSP49P and BSP49H aerogels display characteristic peaks corresponding to the respective calcium compounds, while BSP49Cl does not exhibit XRD peaks. β-$Ca_3(PO_4)_2$ and HAp retained their original crystal structures during the synthesis of the aerogels; while $CaCl_2$ dissolved in the reaction mixture. The absence of characteristic peaks in the spectra of BSP49Cl suggests that $CaCl_2$ was incorporated into the gel in a form other than its original crystalline state, as discussed in Section 5.2.2.

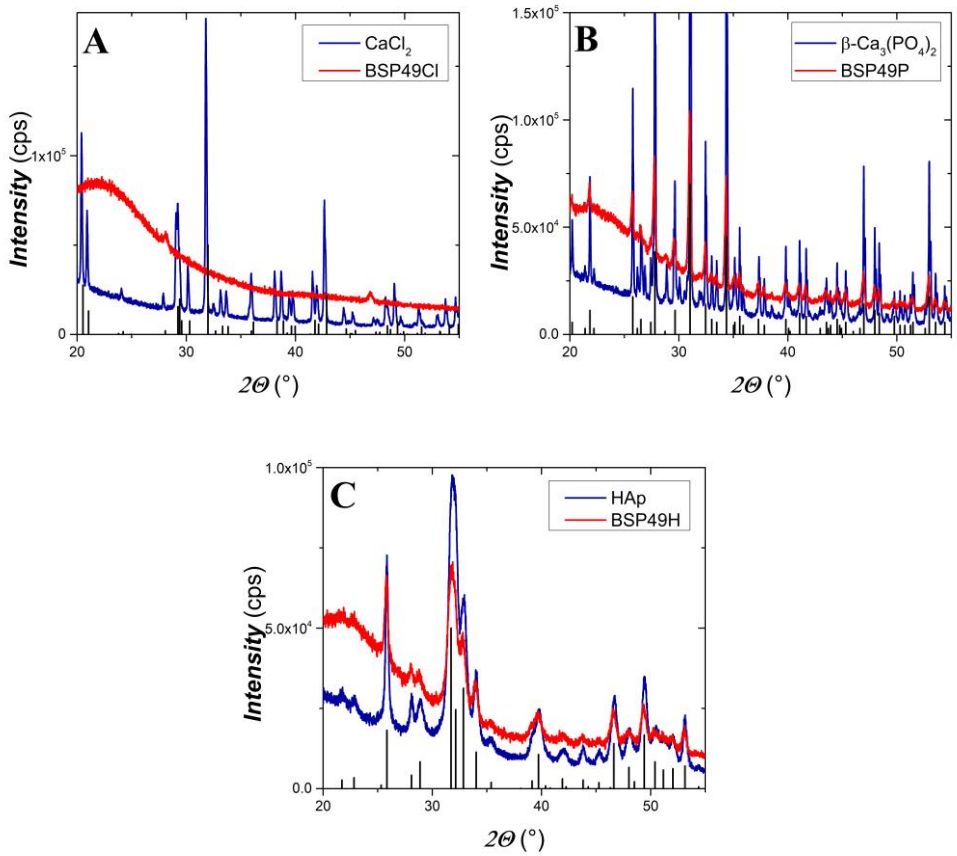

Figure 17. XRD spectra of the different Ca(II) sources and those of the corresponding BSP49Y aerogels: $CaCl_2$ (ICDD-PDF Card No.: 01-070-0385) and BSP49Cl (**A**); β-$Ca_3(PO_4)_2$ (ICDD-PDF Card No.: 00-009-0169) and BSP49P (**B**); HAp (ICDD-PDF Card No.: 01-074-9780) and BSP49H (**C**)

5.4. Small-angle neutron scattering (SANS)

5.4.1. Dry samples

The small-angle neutron scattering curves of the BSPXY aerogels are shown in **Fig. 18.** The scattering curves of the BSPX0, BSPXCl and BSPXP aerogels can adequately be fitted by the second level Beaucage model, which confirms the presence of hierarchical structural levels in these functionalized hybrid aerogels. However, the shapes of the scattering curves of the BSPXH

aerogels are different than the others, and those can be fitted by the first level Beaucage model. The detailed explanation of this difference is discussed as a part of the results of the contrast variation measurements in the following section.

The calculated sizes of the scattering objects and the *p* values (power exponents) of the BSPX0, BSPXCl and BSPXP samples at each level are shown in **Fig. 19.** The sizes of the scattering objects (*D*) were calculated from the determined radius of gyration (R_g) using equation (10).

The scattering objects of the BSPX0 aerogels at the lower structural level show an average diameter of 18-23 nm and are considered to be the pores. These sizes are fully consistent with the N_2 porosimetry results (cf. **Fig. 16**). The scattering objects at the higher structural level display a mean size of 71-80 nm, and are assigned to the loose particle agglomerates observed in the SEM images.

The information on the fractal structures of the scattering objects at the different structural levels is encoded in the power exponents. The *p* values vary between 2.4 and 2.9 at the lower structural level, while at the higher structural level, they range from 3.8 to 4.4. In the first case, these power exponents indicate a mass fractal structure of the pore system, while in the latter case, they provide information on the surface of the scattering object. Power exponents in the range of 3.8 to 4 imply a rough surface, while a power exponent equal to 4 indicates a smooth surface. The *p*-values above 4 suggest a gradual scattering length density transition on the interface of large particle agglomerates.[99, 132]

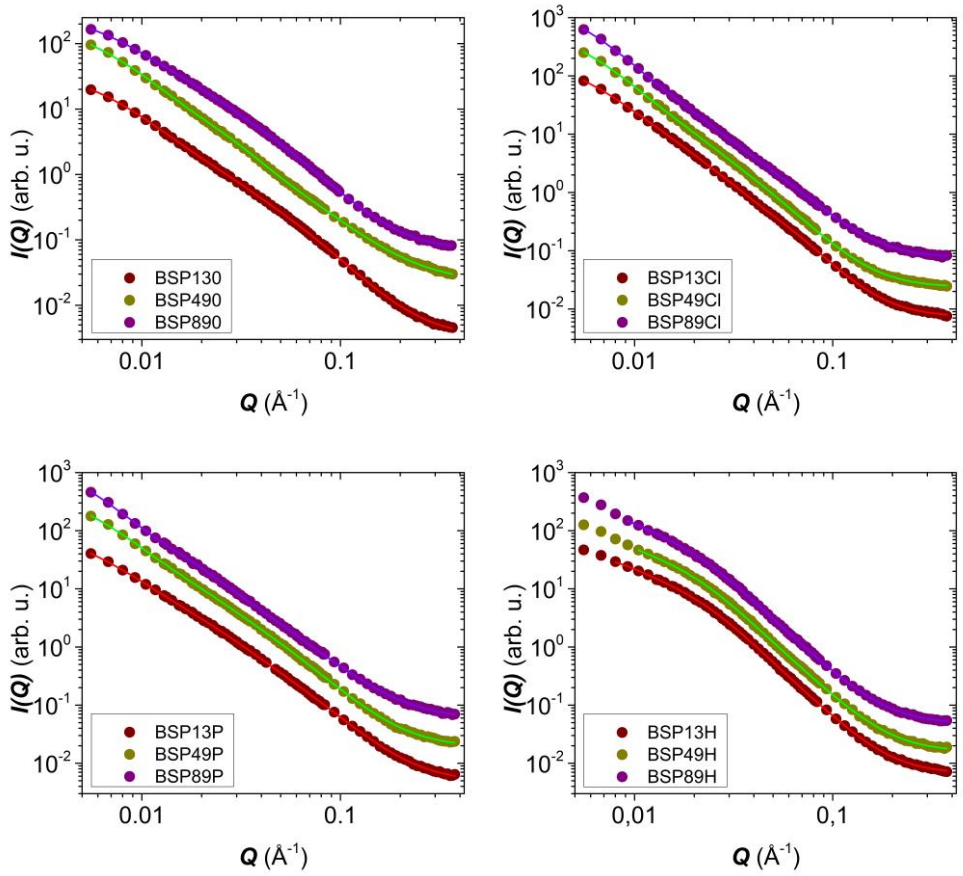

Figure 18. SANS curves of the pristine aerogels, as given in the legend. **Dots:** experimental data. **Lines:** results of fitting. The curves are arbitrarily shifted vertically for clarity.

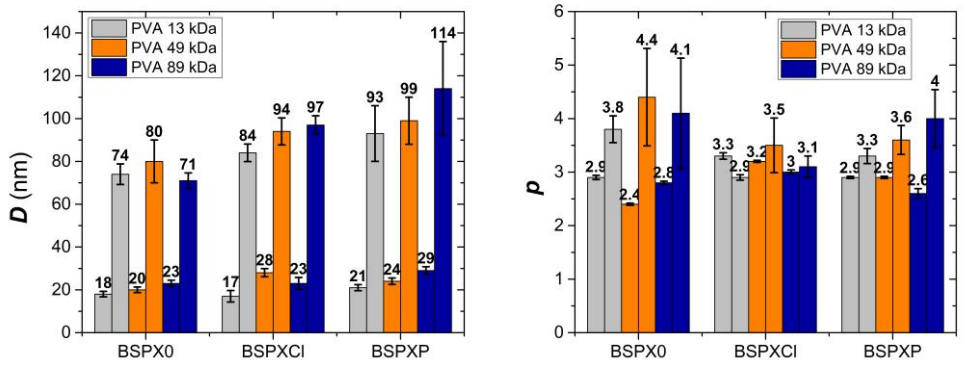

Figure 19. The estimated scattering object sizes (**left**) and power exponents (**right**) of the BSPXY (Y=0/Cl/P) aerogels at the first and second structural levels.

In the case of BSPXCl and BSPXP aerogels, the *D* values at both structural levels are significantly affected by the variation of the molar mass of PVA. However, the presence of the incorporated calcium sources complicates the interpretation. Contrast variation SANS measurements were performed to clarify the contribution of these calcium sources to the nanostructure of the functionalized hybrid aerogels, as discussed in the following section.

Nevertheless, the power exponents at the lower structural level are typical of mass fractals, while at the higher structural level, they indicate a rough surface between the scattering objects. Surface fractals are observed at both structural levels for the BSPXCl aerogels due to the comprehensive aggregation of the primary particles in the backbone, as observed in the SEM images.

5.4.2. Wetting of BSP130

SANS measurements were conducted on wetted BSP130 aerogels to investigate potential hydration-induced morphological changes.[133] The pores of the sample were filled with D_2O in one experiment and with a mixture containing 8V/V% D_2O and 92V/V% H_2O in another. The mixture of 8V/V% D_2O and 92V/V% H_2O has a zero SLD value, equivalent to that of air, and is commonly referred to as a zero-SLD probe.[134, 135]

Special care was taken to ensure complete filling of the pores with liquid, avoiding any trapped air. Thus, the measured intensity solely arises from the scattering-length density (SLD) difference between the aerogel backbone and the probe liquids used in these experiments.

In this way, if any trapped bubbles remained inside the pore network, they would not cause any additional scattering contribution to the total scattering. However, the incoherent scattering of H_2O is notably higher than that of D_2O, complicating the interpretation of scattering curves at higher *Q*

ranges. To address this, an additional background correction was applied by subtracting the incoherent scattering of the probe liquid for both wetted samples to obtain structural information in that *Q* range.

The original and background corrected SANS curves of the dry and the wetted BSP130 samples are shown in **Fig. 20.**

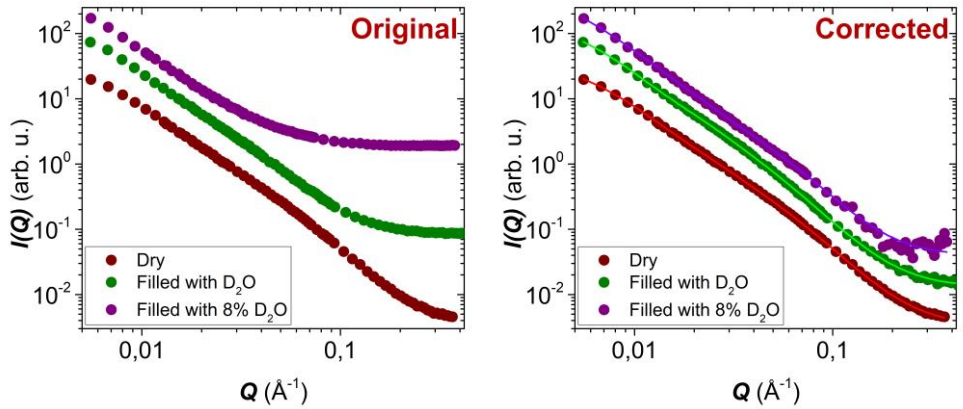

Figure 20. SANS scattering curves of the pristine and wetted (filled with D_2O or 8% D_2O-92% H_2O mixture) BSP130 aerogels. **Left panel:** Original scattering curves. **Right panel:** Background corrected scattering curves with fits. **Dots:** experimental data. **Lines:** results of fitting. The curves are arbitrarily shifted vertically for clarity.

The shape of the background corrected scattering curves of the wetted BSP130 aerogel is very similar to that of the dry one. The scattering curves were fitted by second level Beaucage model, and the estimated structural parameters are collected in **Table 5**.

The estimated structural parameters, along with the shapes of the scattering curves, suggest that the morphological properties of the aerogel are only slightly altered by the wetting. At the lower structural scale, the nanoscale architecture practically remains in its original form; the greater uncertainty in the measurement results is a consequence of the incoherent background scattering of the liquid. However, at the higher structural scale, the morphologies of the aggregates are partially changed, as indicated by the

decreasing power exponent. This change indicates that the interfaces of the aggregates become rougher. Nevertheless, the scattering curves prove that the hybrid aerogel retains its original morphology in aqueous conditions.

Table 5. Scattering object sizes and *p* exponents of the dry and the wetted BSP130 aerogel.

Sample	**Mean object size (nm)** ***high Q region***	***p* exponent** ***high Q region***	**Mean object size (nm)** ***low Q region***	***p* exponent** ***low Q region***
Dry	18 ± 1	2.9 ± 0.1	74 ± 5	3.8 ± 0.3
Filled with D_2O	22 ± 3	2.9 ± 0.1	82 ± 3	3.6 ± 0.4
Filled with zero-SLD water mixture	18 ± 5	3.0 ± 0.2	98 ± 15	3.1 ± 0.2

5.4.3. Contrast variation measurements

Contrast variation SANS measurements were conducted to delve further into the nanoscale architecture of the three-component aerogel systems (borosilicate, PVA, and Ca(II)-source).[136, 137] First, the hybrid aerogel without a calcium source was studied. A set of scattering experiments was performed on the BSP130 sample, filling its pore network with H_2O:D_2O mixtures with systematically changing the liquid composition.[51] After subtracting the incoherent background scattering, the corrected intensities were plotted as a function of the D_2O ratio at three different *Q* values, as shown in **Fig. 21.**

The scattering intensities exhibit a parabolic change as a function of the D_2O ratio, with a minimum at around 50 (V/V)% D_2O composition at all three *Q* values.

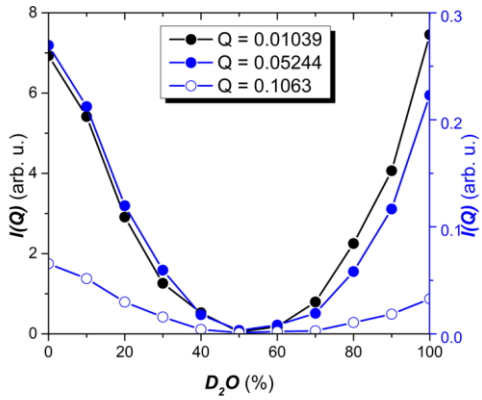

Figure 21. The background corrected scattering intensities as a function of the composition of the H_2O:D_2O mixture in the BSP130 aerogel sample plotted at three different *Q* values (*Q* = 0.01039; 0.05244 and 0.1063 Å).

The theoretical H_2O:D_2O ratio with SLD value equivalent to that of the hybrid backbone was calculated for reference.[138] The hybrid backbone consists of silicon dioxide (SiO_2), boron oxide (B_2O_3), and PVA (C_2H_4O monomer units) in a molar ratio of 2.15:1:1.68 (see **Table 1**). The average skeletal density of PVAs is approximately 1.25 g/cm^3 (based on their safety data sheets), and the average skeletal density of borosilicate glasses is approximately 2.23 g/cm^3.[139] Assuming a molecular-level mixture of the above components, an approximate skeletal density of 2.00 g/cm^3 is estimated. The SLD of the BSP network can be calculated as follows:

$$SLD = \frac{\sum_{i=1}^{n} b_i}{V_m} \qquad (18)$$

b_i is the coherent scattering length of i^{th} of n atoms in a molecule, while V_m is the molecular volume calculated as

$$V_m = \frac{M}{\rho N_A} \qquad (19)$$

M is the molar mass of the BSP network (its composition is estimated from the molar ratios in **Table 1**), ρ is the estimated skeletal density of the BSP network, and N_A is the Avogadro constant. The sum of the scattering lengths in equation (18) is calculated using the estimated molecular composition, and the scattering lengths from the reference.[140] The calculated SLD of the BSP network is thus $3.038 \cdot 10^{-6}$ Å^{-2}, which is equivalent to that of a liquid mixture containing 51.8 (V/V)% D_2O. This theoretical liquid composition is in excellent agreement with the experimental composition exhibiting the minimum scattering intensity inside the hybrid aerogel. This indicates that the inorganic and organic parts do not form separate phases on the nanometer scale in the hybrid aerogel backbone, and do not contribute independently to the measured scattering.

The aerogels containing calcium sources were investigated further using the contrast matching approach. The pores of the BSP13Y aerogels were filled with a 52 (V/V)% D_2O – 48 (V/V)% H_2O mixture to match the contrast of the hybrid backbone (**Fig. 22**).

The contrast-matched scattering curves exhibit a power-law character, except for the BSP13H aerogel. This suggests that the scattering from the Ca(II) sources in the case of BSP13Cl and BSP13P cannot be detected within the measured Q range. The most probable explanation is that the size of the β-$Ca_3(PO_4)_2$ particles is likely too large, and the quantity of Ca(II) particles of BSP13Cl in the backbone is insufficient to contribute to the scattering in this way (based on Sections 5.2.2. and 5.3.).

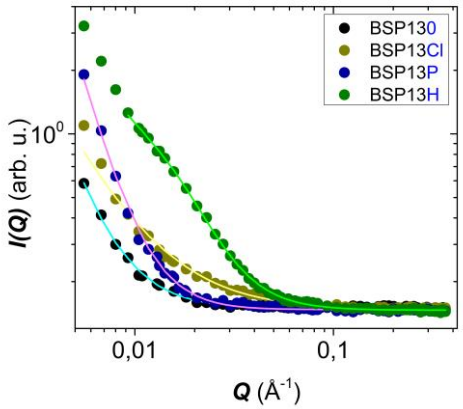

Figure 22. SANS curves of the BSP13Y aerogels filled with 52(V/V)% D_2O – 48(V/V)% H_2O mixture. **Dots:** experimental data. **Lines:** results of fitting.

The scattering curve of the contrast-matched BSP13H sample is fitted using the first level Beaucage model to determine the values of the gyration radius and the *p* exponent. The mean size of the incorporated HAp particles is approximately 61 nm calculated from the radius of gyration using spherical geometry, and the *p* exponent exhibits surface fractal characteristics.

To rule out the possibility of any hydration-induced morphological changes in the BSPXH aerogels, the wetting of the BSP49H aerogel was studied in detail.[133] Similarly to BSP130, the incoherent scattering of the probe liquid was subtracted from the scattering curves of the wetted samples to obtain structural information in the higher *Q* range and to enable comparison of the scattering curves between the wetted and pristine samples. The scattering curves of the pristine BSP49H aerogel, along with samples filled with D_2O and zero-SLD water mixture (background corrected), are shown in **Fig. 23A.**

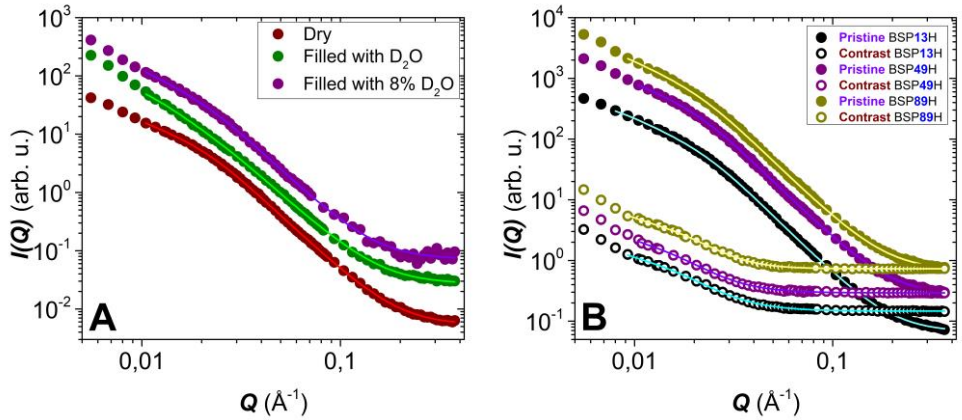

Figure 23. Panel A: SANS scattering curves of the pristine and wetted (filled with D_2O or 8% D_2O-92% H_2O mixture) BSP49H aerogels. The scattering curves of the wetted samples are background corrected. **Panel B:** SANS scattering curves of pristine and contrast-matched BSPXH aerogels. **Dots:** experimental data. **Lines:** results of fitting. The curves are arbitrarily shifted vertically for clarity.

The shapes of the scattering curves of the dry and the zero-SLD wetted BSP49H samples are similar, while that of the D_2O-filled sample is slightly different. The scattering curves were fitted using the first level Beaucage model, and the estimated structural parameters are collected in **Table 6.** The structural parameters of the sample remain the same when wetted with zero-SLD as in the dry state, while minor differences are observed in the case of the D_2O-wetted sample. Nevertheless, it can safely be concluded that the Ca(II)-doped hybrid aerogel preserves its original morphology in aqueous solutions.

Table 6. Scattering object sizes and *p* exponents of the dry and the wetted BSP49H aerogel

Sample	**Mean object size (nm)**	***p* exponent**
Dry	52 ± 1	3.2 ± 0.1
Filled with D_2O	49 ± 2	3.0 ± 0.1
Filled with zero-SLD water mixture	52 ± 1	3.2 ± 0.1

The scattering curves of all contrast-matched BSPXH aerogels filled with the 52 (V/V)% D_2O – 48 (V/V)% H_2O mixture, together with the scattering curves of their pristine representatives are shown in **Fig. 23B.** The scattering curves of the dry and the contrast-matched BSPXH samples exhibit similar trends no matter the molar mass of PVA used. The calculated structural parameters are collected in **Table 7.**

Table 7. Estimated size of the scattering objects and *p* exponents in the case of the pristine and the contrast matched BSPXH aerogels.

Code name	Pristine		Contrast matched	
	Size (nm)	*p* exponent	Size (nm)	*p* exponent
BSP13H	48 ± 0.5	3.2 ± 0.01	61 ± 2.6	2.8 ± 0.05
BSP49H	52 ± 0.7	3.2 ± 0.01	61 ± 4.6	3.0 ± 0.09
BSP89H	51 ± 0.7	3.2 ± 0.01	52 ± 3.1	3.5 ± 0.22

The sizes of the scattering objects in the dry samples are smaller than those in their contrast-matched representatives. The incorporation of HAp significantly alters the shape of the scattering curves of the hybrid aerogels. However, based on the SEM images and the N_2 porosimetry results, the fundamental morphological properties of the hybrid backbone remain unchanged when a Ca(II) source is incorporated into it. This apparent contradiction can be resolved by taking into account that the scattering curves of the BSPXH aerogels are composed of contributions from pores, agglomerates, and HAp particles, which makes it difficult to assign the estimated size to one individual scattering object. However, in the case of contrast-matched scattering curves, the calculated size gives the mean size of the HAp particles that are within the SANS size range. The smaller objects observed in the case of BSP89H can be attributed to the presence of backbone inhomogeneities, including aggregates observed in SEM images that contribute to the scattering even in contrast-matched conditions. The schematic

illustration of the information provided by the contrast variation SANS measurements is shown in **Fig. 24**.

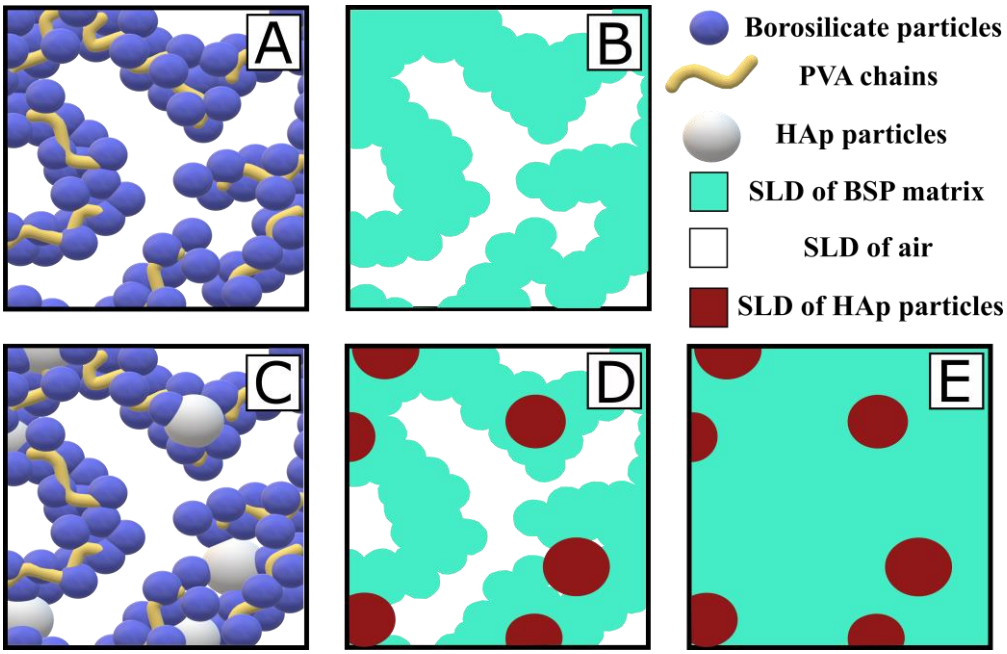

Figure 24. Panel A: Schematic illustration of the backbone of the BSPX0 samples. **Panel B:** Scattering density map of the BSPX0 samples. **Panel C:** Schematic illustration of the backbone of the BSPXH samples. **Panel D:** Scattering density map of the BSPXH samples. **Panel E:** Scattering density map of the BSPXH samples filled with a D_2O-H_2O mixture of equivalent SLD to the BSP network.

Because the scattering from the Ca(II) particles of BSP13Cl and the β-$Ca_3(PO_4)_2$ particles does not contribute significantly to the total scattering, the structural properties of these aerogels could be interpreted similarly to the case of the BSPX0 samples. However, the contribution of the incorporated calcium compounds cannot completely be neglected. The contrast-matched BSP13P shows a *p* exponent equal to 3.2 when fitted by a simple power-law model. This surface fractal behavior can be explained by the scattering from the β-$Ca_3(PO_4)_2$ particles, which provide an additional contribution in the low *Q* range, making that region difficult to interpret.

In the case of $CaCl_2$ addition, such contribution is not possible because the size and the amount of the Ca(II) particles are much smaller. The contrast-matched scattering curve of BSP13Cl shows higher intensity than that of BSP130, which could be explained by the partial incorporation of the Ca^{2+} ions into the hybrid backbone changing its SLD (as discussed in Section 5.2.2.). The amount of these ions is small, and their distribution in the backbone is not homogeneous according to elemental mapping (EDS) images, thus they can only slightly alter the SLD of the backbone. Nevertheless, further investigation is required to confirm these theories.

5.5. Particle size distribution of hydrated BSP130

Fig. 25 shows the particle size distribution of the hydrated BSP130 sample. The mean particle size is approximately 10 μm, with particles observed up to ~50 μm, along with smaller particles in the range of a few micrometers.

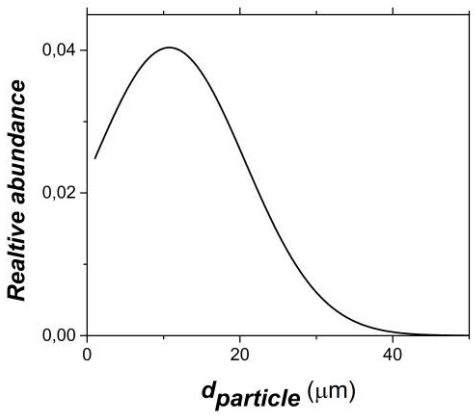

Figure 25. Particle size distribution of hydrated BSP130 samples, calculated from light microscope images of the suspended aerogel particles using ImageJ software.

5.6. ζ-potential

Fig. 26 illustrates the pH-dependent electrophoretic mobilities and the calculated ζ-potentials of the BSP49Y aerogels. The electrophoretic mobilities of the BSP49Y aerogel suspensions range from 0 to -2.2 μmcm/Vs, showing a decreasing trend with increasing pH. Although the particle size distribution of the suspensions was not measured, the particles are predominantly expected to be in the micrometer size range. The measured electrophoretic mobility likely corresponds to smaller particles closer to the nanometer scale. Due to the large particle sizes, the calculated ζ-potentials are not physicochemically precise but provide a useful reference for *in vitro* cell assays regarding the surface charges of hydrated aerogel particles.

The calculated ζ-potential of suspended BSP490 decreases from -8 to -27 mV with the increase of the pH. The deprotonation of Si-OH and B-OH groups is crucial in determining the surface charge of BSP490, which explains why it remains negative across the entire measured pH range, with the negative charge increasing as the pH rises. The incorporation of calcium compounds into the gel backbone results in higher, but still negative ζ-potentials. This effect may be explained by the presence of Ca^{2+} ions on the surface of the incorporated calcium compounds that alter the composition of the electric double layer of the suspended gel particles. The decreasing ζ-potential with the increasing pH can be explained by specific anion sorption onto the surface of the suspended particles. The overall trend in the ζ-potential changes of BSP49P and BSP49H aerogels as a function of pH is similar to that of the calcium-free sample. However, the change in the ζ-potential of the BSP49Cl aerogel shows a different tendency than the others, especially at a higher pH values. This can be explained by the fact that the Cl^- counter ion can be exchanged for OH^-, which is not possible with the other two calcium compounds. This ion exchange mechanism results in a balance of the negative charges. In the case

of the other two calcium sources, the specific adsorption of OH^- ions occurs on the surfaces of the particles, resulting in the accumulation of negative charges, which is reflected in the more negative ζ-potentials at higher pH values.

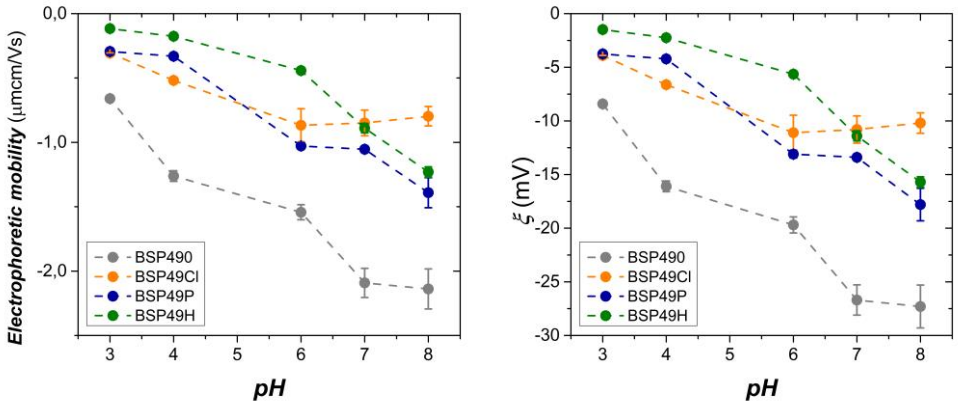

Figure 26. The measured electrophoretic mobilities (**left**) and the calculated ζ-potentials (**right**) of the BSP49Y aerogels as a function of pH in the range of 3.0 to 8.0.

6. Biological tests of the hybrid aerogels

The long-term collaborators of our research group, Dr. Gábor Szemán-Nagy and his team at the University of Debrecen conducted *in vitro* biological tests on BSP49Y samples that contain Ca(II) sources. The monolayer regeneration of scratched cell cultures and the growth of these cultures were investigated in the presence of suspended aerogel particles for 48 h. DPSC (Dental Pulp Stem Cells) and MG-63 cell cultures were utilized for these biological experiments. In both cases, the changes in the cell cultures were monitored using video microscopy, and quantitative analyses were conducted by digital image analysis. Representative time-lapse video microscopy image collates are shown in **Figure 27** for the DPSC cell culture scratch tests in the absence and in the presence of suspended aerogel particles. [90]

The presence of aerogel particles attracted both types of cells, causing cells to migrate and attach directly to them. This phenomenon increased the apparent damaged surface area at the beginning of the scratch tests and initially reduced the rate of monolayer formation and culture regeneration (**Fig 28**). This effect was more pronounced in the MG-63 cell culture. However, by the end of the experiments, the regeneration of the monolayer resulted in the full coverage of the particles, with homogeneous integration into the culture observed in both cases. In the case of monolayer growth assays, despite the initial delay, the generation time was comparable to that of untreated cultures by the end of the experiment. Furthermore, it was observed that increasing Ca(II) content facilitated a faster monolayer production at uniform particle concentrations (**Fig 29**).

Importantly, the experiments demonstrated that aerogels had an effect on the cells inducing their migration and attachment to the suspended particles with no signs of apoptosis, necrosis, or any detectable toxicity. Overall, these

findings strongly support both the biocompatibility and the beneficial biostimulating effect of hybrid aerogels when administered as aqueous suspensions, particularly in relation to cell types crucial for bone regeneration.

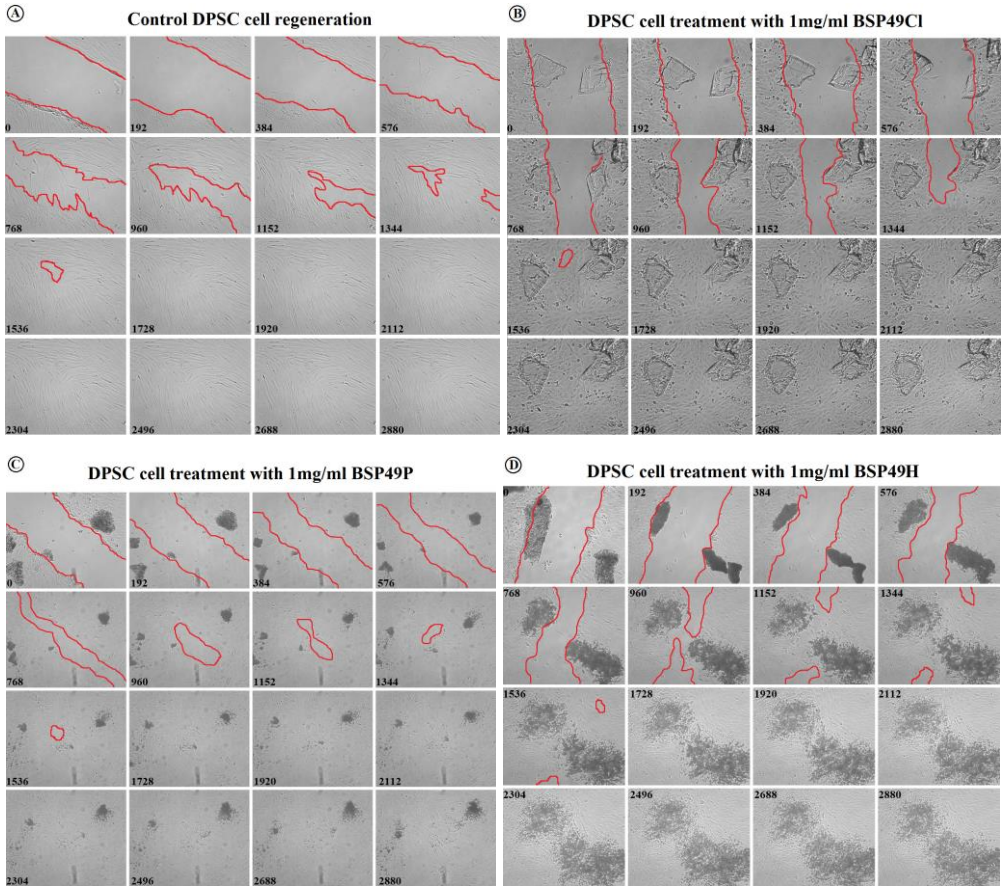

Figure 27. Regeneration of damaged DPSC cell monolayers. **Panel A:** Damaged DPSC cell monolayer without aerogel particles. **Panel B:** 1.0 mg/mL BSP49Cl treatment. **Panel C:** 1.0 mg/mL BSP49P treatment. **Panel D:** 1.0 mg/mL BSP49H treatment.[90]

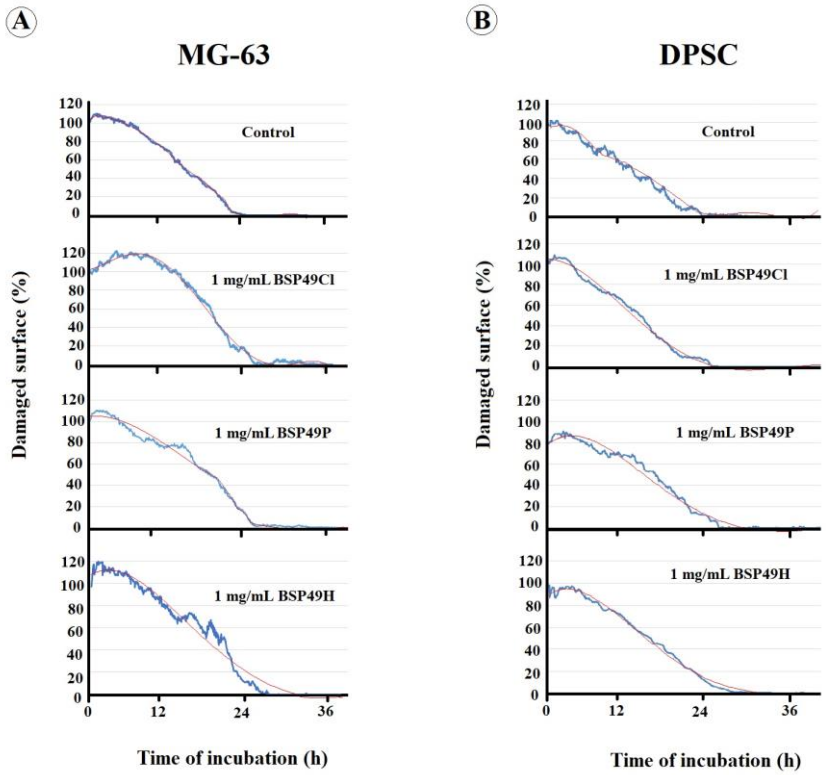

Figure 28. Regeneration of damaged MG-63 **(A)** and DPSC **(B)** cell monolayers in the absence (control) of aerogels, and in the presence of 1.0 mg/mL BSP49Cl, BSP49P and BSP49H aerogels, as given in the figures.[90]

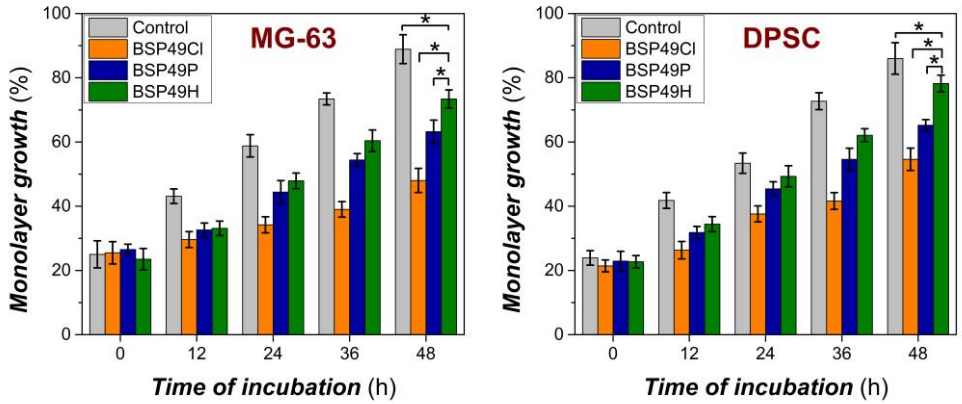

Figure 29. Formation of a monolayer starting from ca. 20% confluence in MG-63 **(left)** and DPSC **(right)** cell cultures in the absence (control) and in the presence of 1.0 mg/ ml BSP49Cl, BSP49P and BSP49H aerogels, as given in the figures. Quantification is based on the digital image analysis of time lapse video microscopy recordings. All experiments were run in triplicates. Statistical testing is based on the unpaired t-test with significance at $*p < 0.05$.[90]

7. Wetting mechanism of a typical Ca(II)-alginate aerogel according to SANS measurements

7.1. Motivation and preliminary results

During the various biomedical applications of aerogels, the porous particles directly interact with different body fluids. These interactions can lead to such changes in the structure that can affect the performance of the material. Studying these solid-liquid interactions is quite challenging, even if the interactions occur only with water molecules with no dissolved substances in the liquid medium.

The surface characteristics of aerogels are decisive to determine their features, because they have very high surface-to-volume ratios. If the surface has a hydrophilic character, then interactions with water molecules result in strong secondary bonds, which can lead to changes in the nanostructure, resulting in changes in the macroscopic properties.

In the case of borosilicate hybrid aerogels, no significant morphological changes were observed during their wetting despite their hydrophilic characteristics, as described in Sections 5.4.2 and 5.4.3. This is independent evidence that the original advantageous morphological properties of the BSPXY aerogels are retained during their biomedical applications.

However, in the case of (bio)polymer-based aerogels, such as polysaccharide aerogels, the wetting of their backbone often results in changes in their nanostructures.[5, 141-143]

One of the most intensively investigated biopolymer-based aerogel is the calcium alginate aerogel, which has promising uses in drug delivery and wound treatment.[47, 144, 145] Light microscopy images of an archetypical calcium alginate aerogel at different water contents are shown in **Fig. 30.**[5]

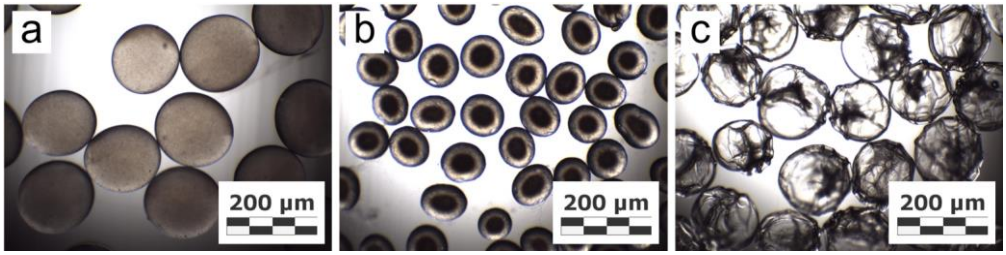

Figure 30. Microscopy images of Ca(II)-alginate aerogel beads in the dry state (**a**) and in the hydrated states at 0.32 g/g (**b**) and 2.0 g/g water content (**c**).[5]

In a preluding study, the hydration and wetting mechanism of an archetypical calcium alginate aerogel was explored using a combination of complementary characterization techniques. A qualitative model was developed, which successfully accounts for the liquid-state NMR (including relaxometry, cryoporometry, and diffusiometry), solid-state NMR, and SANS characterization results.[5] Upon gradual hydration of the aerogel, the following structural changes were identified.

Initially, at low water content, the water molecules are strongly bound to the hydroxyl and carboxyl groups of the calcium alginate macromolecules through hydrogen bonds in an orderly fashion, becoming part of the tertiary and quaternary structures of the alginate macromolecules. The binding sites for structural water saturate at approximately 0.4 g/g water content. Concurrently, water molecules form multilayers, creating the primary hydration sphere that is strongly associated with the alginate macromolecules. The appearance of structural water and the primary hydration sphere at different water contents is clearly observed in NMR relaxometry, as shown in **Fig. 31**. Due to the highly hydrophilic nature of calcium alginate, its primary hydration sphere is extensive, with most of the water being localized within this sphere in the aerogel. The gradual increase in the T_2 value of the primary hydration sphere's domain indicates that its thickness gradually increases with higher levels of hydration, showing that the primary hydration sphere fills continuously. Up to

a water content of 0.4 g/g, hydration facilitates the macromolecules' conformational changes into an energetically favorable state, altering their tertiary and quaternary structures. Ultimately, this leads to the rearrangement of the primary fibrils into fibers, increasing the pore sizes.[5]

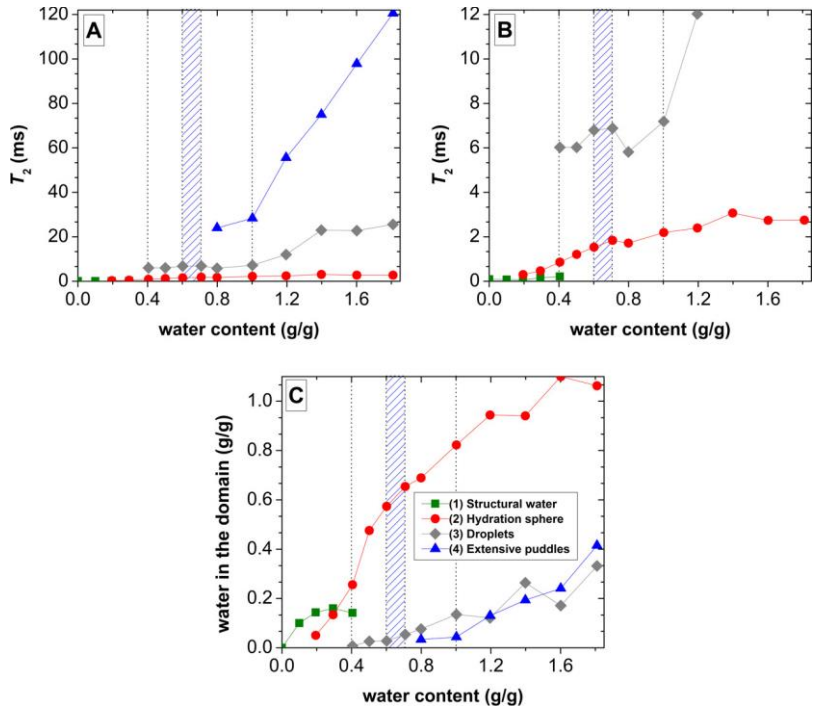

Figure 31. NMR relaxometry of hydrated calcium alginate aerogel. The domains are color-coded to reflect their appearance with increasing water content: (1) Green represents structural water, (2) Red denotes the primary hydration sphere, (3) Gray indicates droplets, and (4) Blue corresponds to extensive puddles. **Panels A** and **B** show the observed T_2 relaxation times for each domain as a function of water content. The data set is identical in both panels, with different y-axis scales. **Panel C** illustrates the water content of each domain relative to the overall hydration level, calculated from the relaxation amplitudes.[5]

Starting at approximately 0.4 g/g water content, a third relaxation domain appears, which is associated with water droplets at the focal points of the polymer. Additionally, a sharp peak in the solid-state ^{1}H MAS NMR spectrum indicates the presence of these droplets. According to NMR cryoporometry, the estimated size of these droplets ranges from 20-40 nm,

much smaller than the estimated pore size of about 76 nm from SANS measurements. The T_2 value of the droplets gradually increases with rising water content, indicating that their size expands continuously within the fibrillar backbone. Up to a water content of around 0.6 g/g, the hydration mechanism aligns with that of a well-defined porous material with a strongly hydrophilic backbone.

However, above 0.6 g/g water content, the SANS curves change significantly, and at about 0.8 g/g water content, a fourth relaxation domain appears with a relaxation time an order of magnitude slower than that of the third domain. This is associated with a quasi-bulk region of water. Additionally, the third relaxation domain shows a steep increase in T_2. These observations indicate a drastic structural change: the disintegration of the fibers into well-hydrated chains that entangle to form a quasi-homogeneous 3D network, which results in the collapse of the pore structure. The transformation of the aerogel into a hydrogel-like network is complete at approximately 1.0 g/g water content. Beyond this water content, no significant structural or morphological changes were observed. The hydrogel-like network simply becomes progressively less dense, as indicated by the marked increase in the T_2 of the fourth relaxation domain. The hydration-induced structural changes are visualized in **Fig. 32**.[5]

In the preluding study, the SANS scattering curves were evaluated using Beaucage's unified approach, from which radii of gyration (R_g) and power exponents (p) were determined. However, due to its lack of specificity to the particular structure under investigation, this approach could only offer limited insights into the hydrated porous structure.

In this study, a material-specific structural model is introduced to enable quantitative analysis of the SANS data and support precise information on the nanostructural changes induced by the hydration of the aerogel.[146] The

model was developed in a cooperation with Dr. Cédric J. Gommes, associate professor at the University of Liège. The data fitting was performed using a non-linear least-squares algorithm in the MATLAB software.

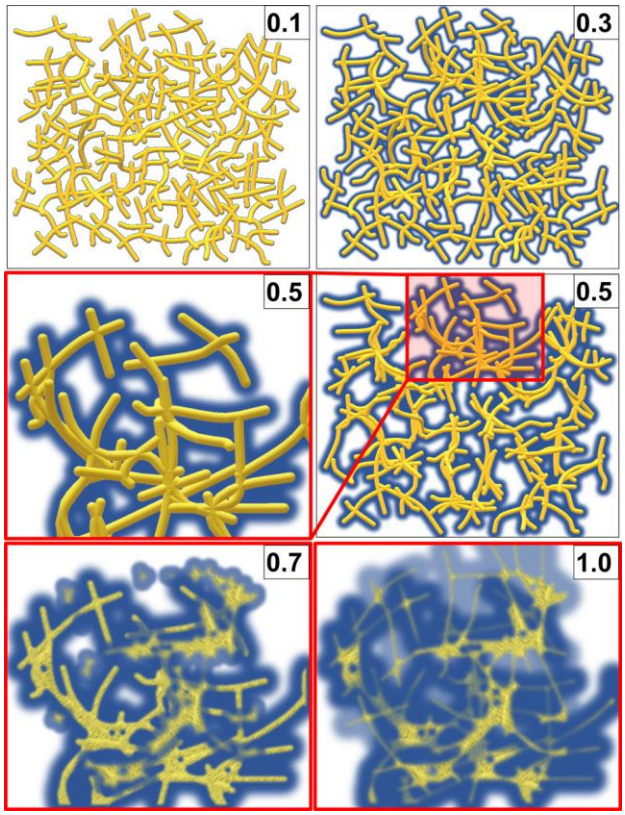

Figure 32. Graphical illustration of the hydration-induced structural changes that occur during the wetting of an archetypical calcium alginate aerogel. The corresponding water content in grams of water / grams of dry solid units is shown in the upper right corner of each panel. The red frames indicate magnified views. The well-defined porous structure of the aerogel remains intact up to approximately 0.6 g/g water content, while water droplets begin to form at the focal points of the aerogel network at around 0.4 g/g water content. The original alginate fibrils rearrange into fibers, which is clearly observed at 0.5 g/g water content. The transition to a hydrogel-like phase occurs at a critical water content of 0.6−0.7 g/g, where the well-hydrated alginate chains rearrange into a quasi-homogeneous 3D gel network.[5]

7.2. General wetting model

The SANS curves obtained at the various hydration levels of the calcium alginate aerogel are shown in **Fig. 33.** To ensure accuracy, the intensity corresponding to the highest *Q* value was considered as background and subtracted from each scattering pattern. For subsequent analysis, only points with an intensity more than 5% above this background were taken into account.

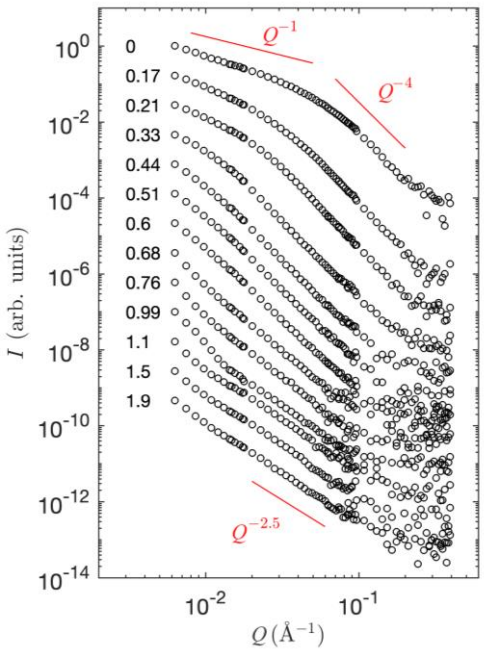

Figure 33. Small-angle neutron scattering (SANS) patterns that were measured on Ca(II)-alginate aerogel samples with increasing water content. The curves are arbitrarily shifted vertically for clarity. The labels indicate the water contents, measured in grams of water per gram of polymer. The red lines represent specific power laws relevant to the discussion.

The dry aerogel (uppermost curve) displays a two-stage scattering pattern: Q^{-1} power-law scattering at very low *Q*, followed by Porod-like Q^{-4} scattering at high *Q*. This indicates a mesoporous structure composed of elongated elements, characteristic of the nanostructured skeleton of Ca(II)-

alginate aerogels. The solid skeleton consists of overlapping dense polymer fibrils, each a few nanometers wide.[147] Upon hydration, this structure gradually diminishes.

On a macroscopic level, the most hydrated sample forms a hydrogel (see **Fig. 30c**). This transition is also observed on the nanometer scale in its SANS pattern (lowest curve) as it displays $Q^{-2.5}$ scattering. This exponent value is typical of polymeric structures in solution, particularly solvated gels.[148-150]

The comprehensive structural model we propose is shown in **Fig. 34.** Initially, in the dry state, the aerogel exhibits a mesoporous structure, with the solid skeleton composed of dense polymer fibrils (**Fig. 34a**). While the dry aerogel is known to comprise nanometer-sized fibrils, no specific shape is assumed for the skeleton at this stage.

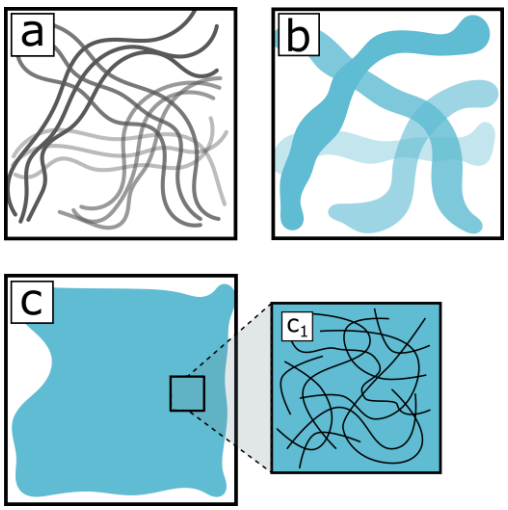

Figure 34. The overall structural model assumed for the SANS data analysis of Ca(II)-aerogels upon hydration. The structures within the dry aerogel (**a**) absorb water and subsequently undergo swelling and eventually merge (**b**). Finally, they attain macroscopic dimensions (**c**), and at a smaller molecular scale, the structure transitions from that of a dense polymer to a hydrogel (**c**$_1$).

Previous NMR studies indicate that water initially absorbs into the alginate chains and gradually hydrates the supramolecular chain assemblies, leading to a rearrangement of the tertiary and quaternary structures of the macromolecules.[5] However, these molecular processes cannot be observed using low-resolution methods such as SANS. Thus, it is hypothesized that water progressively infiltrates the skeleton, potentially causing swelling and the merging of swollen fibers into larger structures (**Fig. 34b**).

Upon complete saturation with water, these larger structures attain macroscopic dimensions (**Fig. 34c**). Throughout this process, the molecular-scale inner structure of the skeleton gradually transitions from a dry, dense polymer to a hydrogel (**Fig. 34c$_1$**).

In the following discussion, the volume fraction of the skeleton in the whole volume of the aerogel is denoted as ϕ_s, thereby representing the porosity (illustrated in white in **Fig. 34**) as $1 - \phi_s$. The term 'polymer' is used to describe the material because the model is more general than the specific alginate under examination. The volume fractions of water and polymer within the hydrated skeleton are denoted as φ_w and φ_p, respectively.

Since the model shown in **Fig. 34** assumes the absence of water and polymer outside the skeleton, their local relative proportions within the skeleton are identical to the macroscopic water content of the aerogel, as described by equation (20).

$$\varphi_w = \frac{V_w}{V_w + V_p} = \frac{\frac{V_w}{V_p}}{\frac{V_w}{V_p} + \frac{V_p}{V_p}} = \frac{V}{V + 1} \qquad (20)$$

V is the overall volume fraction of water over polymer in the macroscopic sample, and V_w (V_p) is the volume of water (polymer). This can be expressed in terms of mass fractions as

$$V = \frac{m_w/\rho_w}{m_p/\rho_p} = \frac{V_w}{V_p} \qquad (21)$$

where m_w (m_p) is the mass of water (polymer) and ρ_w (ρ_m) is its density.

Calculating the scattering patterns corresponding to the structures shown in **Fig. 34** presents two primary challenges. First, there is the hierarchical nature of the structure, encompassing both the large-scale structure of the swelling skeleton, and the small-scale gel-like inner structure of the skeleton. Second, there is the task of devising an appropriate model for the inner structure of the skeleton. That model must effectively interpolate all structures ranging from the dense polymer to the swollen hydrated polymer fibers in a realistic manner.

7.3. Two-scale structural model

The scattering arising from the two-scale structure of the aerogel can be computed utilizing a modeling approach established in previous research.[92, 151] In line with that methodology, the indicator function of the skeleton is introduced, denoted as $\mathrm{I}_s(\mathrm{x})$, which assigns the value 1 if a point x is within the skeleton and 0 otherwise. Similarly, the indicator function of the polymer, $\mathrm{I}_p(\mathrm{x})$, is defined. Using these, the space-dependent scattering-length density of the wet aerogel can be expressed as

$$b(x) = \mathrm{I}_s(\mathrm{x})\left[b_w + \left(b_p - b_w\right)\mathrm{I}_p(\mathrm{x})\right] \qquad (22)$$

Equation (22) represents the two structural scales, where b_w and b_p are the scattering-length densities of water and polymer, respectively. The indicator function of the polymer $\mathrm{I}_p(\mathrm{x})$ is defined assuming it occupies the entire volume of the sample, but the multiplication by $\mathrm{I}_s(\mathrm{x})$ restricts it to within the skeleton.

In a broad sense, the scattering cross-section is equivalent to the Fourier transform of the scattering-length correlation function[93, 95, 152], described as

$$I(Q) = \int_0^\infty \frac{\sin(Qr)}{Qr} \bar{C}_b(r) 4\pi r^2 dr \qquad (23)$$

,where the scattering-length correlation function is expressed as

$$\bar{C}_b(r) = \langle b(x)b(x+r)\rangle - \langle b(x)\rangle^2 \qquad (24)$$

In equation (24), the angle brackets represent the average value computed across all *x* values. The overline denotes a centered correlation function, where the asymptotic value $\langle b(x)\rangle^2$ is subtracted. For isotropic structures, the vectorial dependency on *r* simplifies to a dependency on the modulus $r = |r|$.

To distinguish between the influences of the polymer and skeleton structures on the correlation function $\bar{C}_b(r)$, it is important to define their covariances. The covariance of any phase *X* is represented as[153, 154]

$$C_X(r) = \langle \mathrm{I}_X(\mathrm{x})\mathrm{I}_X(\mathrm{x}+\mathrm{r})\rangle \qquad (25)$$

It is interpreted as the probability that two randomly selected points, situated at a distance *r* from each other, both belong to *X*. At small distances *r*, the covariance equals the volume fraction φ_X. Conversely, for distances much larger than a characteristic size of *X*, the covariance $C_X(r)$ tends towards φ_X^2.[155, 156] The 'centered' covariance is defined by subtracting the limit value, as

$$\bar{C}_X(r) = C_X(r) - \varphi_X^2 \qquad (26)$$

For large values of *r*, it approaches zero and maintains a value of

$$\bar{C}_X(0) = \varphi_X(1 - \varphi_X) \quad (27)$$

Based on these assumptions, the correlation function described in equation (24), using the expression for the two-scale scattering-length density in equation (22), can be defined as:

$$\bar{C}_b(r) = \left[b_w + \varphi_p\left(b_p - b_w\right)\right]^2 \bar{C}_s(r) + \phi_s\left[b_p - b_w\right]^2 \bar{C}_p(r) \quad (28)$$

The Fourier transform of equation (28) gives the general intensity function for the hierarchical structure, expressed as

$$I(Q) = \left[b_w + \varphi_p\left(b_p - b_w\right)\right]^2 I_s(Q) + \phi_s\left[b_p - b_w\right]^2 I_p(Q) \quad (29)$$

where $I_s(Q)$ and $I_p(Q)$ are the Fourier transforms of the skeleton and polymer centered covariances, respectively. The initial term addresses the scattering originating from the macroscopic structure, wherein the bracketed factor represents the average scattering-length density of the polymer- and water-containing skeleton, considered as a uniform phase. The subsequent term addresses the scattering arising from the internal structure of the skeleton, with the bracketed expression representing the contrast between water and polymer. This second factor appears to be multiplied by ϕ_s, as anticipated, given that the examined structure is confined only within the skeleton and thus extends over only that particular fraction of space. Equation (29) represents the general two-scale model, which does not specify any particular form for either the scattering of the skeleton or the polymer structure within it. The subsequent tasks involve determining specific expressions for the skeleton and polymer scattering.

7.4. Inner structure of the skeleton: the Boolean model of wet polymers

From a scattering perspective, the primary feature of the hydrated structures shown in **Fig. 33** is the dominance of a $Q^{-2.5}$ scattering pattern. Such an exponent, close to 2, is typical of polymers in solution and can theoretically be modeled using various form factors.[97, 99, 148, 150, 157] The main challenge is to reasonably extend these form factors into the concentrated solution regime, where the polymer concentrations are high enough that individual polymer coils touch and overlap. Applying a dilute polymer solution model at high concentrations would greatly overestimate the scattering by summing the scattering-length densities of overlapping coils. Conversely, incorporating a structure factor might mathematically keep the coils separate, preventing overlap, but this would be physically unrealistic for a hydrogel, which is highly cross-linked.[97] We propose a third approach based on Boolean models.[154, 155, 158]

The general principle of Boolean models involves randomly distributing a specific motif in space - referred to as 'grains' in materials science literature - and allowing them to overlap whenever they come into contact. Unlike the dilute-solution approach, when two grains overlap, they are not summed but are considered as a single entity. This approach has been used to model the scattering of porous materials by using spherical grains to represent either the solid phase or the pores (Swiss-cheese model) in another research.[159-161] In our case, we propose using a polymer coil as the grain.

Since overlapping is treated on an all-or-nothing basis, the overlapping regions effectively represent the cross-linking of the polymer. In this Boolean approach, two coils overlapping at a point are structurally equivalent to a four-branch star polymer. When a large number of coils overlap, this results in a dense, homogeneous polymer region without microstructure. The entire

process is illustrated in **Fig. 35**, using 2D random walks to represent the polymer coils.

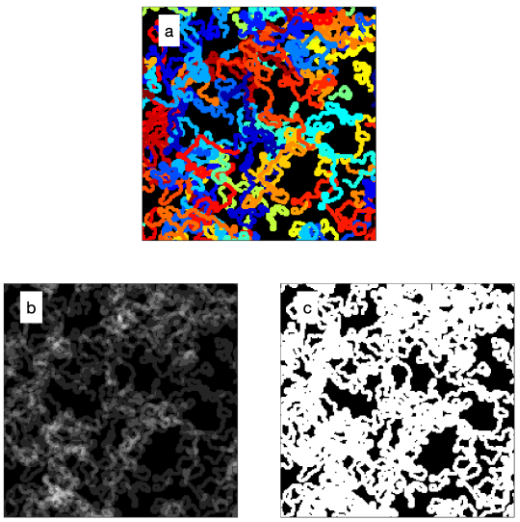

Figure 35. Two-dimensional illustrations of the Boolean model for a concentrated polymer solution or a hydrogel. **Panel a:** Individual polymer coils, each shown in a different color. **Panel b:** The incorrect scattering density map that results from summing the contributions of all coils (based on the dilute solution approximation). **Panel c:** The Boolean model constructed from the same coils.

The volume fraction of the polymer for the Boolean model can be expressed as[154, 159, 160]

$$\varphi_p = 1 - \exp\left[-\theta v_p\right] \qquad (30)$$

v_p is the volume of a single polymer coil and θ is the number of coils per unit volume. The key structural feature for small-angle scattering is the centered covariance $\bar{C}_p(r)$, which Fourier transform yields the intensity $I_p(Q)$ used in equation (29). Within the framework of a Boolean model, the centered covariance is determined as follows[154, 159, 160]

$$\bar{C}_p(r) = \left(1 - \varphi_p\right)^2 \left(exp\left[\theta K_p(r)\right] - 1\right) \quad (31)$$

$K_p(r)$ is the geometric covariogram of the grain, which is defined as the intersection volume of two identical grains translated by a distance *r* relative to each other. In small-angle scattering terminology, the Fourier transform of $K_p(r)$ represents the form factor of the individual polymer coils. It is normalized so that its value at $Q = 0$ equals v_p^2.

In the limit of low polymer concentrations, the Boolean model behaves identically to a dilute polymer solution, as expected. Specifically, equation (30) simplifies to $\varphi_p \cong \theta v_p$ for extremely small values of θ, which aligns with the scenario where coil overlap is negligible. Similarly, the covariance in equation (31) simplifies to $\bar{C}_p(r) \cong \theta K_p(r)$, resulting in the scattered intensity being proportional to both the polymer concentration and the form factor. However, at finite concentrations, polymer overlap becomes significant, leading to a nonlinear relationship between concentration θ and both the volume fraction φ_p and the covariance $\bar{C}_p(r)$. These nonlinearities are precisely described by equations (30) and (31).

A variety of form factors are discussed in the literature for modeling small-angle scattering by individual polymer coils.[97, 99, 148, 157] However, these expressions are challenging to use within the context of a Boolean model because they lack a simple real-space equivalent that can serve as a geometric covariogram $K_p(r)$ in equation (31).

Therefore, the following simple approach is considered. A power-law scattering function of the form $I \cong Q^{-D}$ in reciprocal space (where $D = 2$ for polymers) corresponds to a geometric covariogram $K_p \cong r^{D-3}$ in real space.[162, 163] Since this power-law behavior inevitably breaks down when *r* exceeds the size of the polymer coil or is smaller than its building blocks, two

cutoff lengths, a and b, are introduced, representing the upper and lower bounds, respectively, and assume a covariogram of the form:

$$K_p(r) = v_p \exp\left(-\frac{r}{a}\right)\left(1+\frac{r}{b}\right)^{D-3} \qquad (32)$$

In the specific case where $D = 2$ and $b \ll a$, this model aligns with the Lorentz approximation of a polymer form factor, where the radius of gyration is $R_g^2 = 3a^2$. For the general case with an arbitrary D, the radius of gyration can be determined by matching the Fourier transform of equation (32) with Guinier's law for small Q, resulting in the following value:

$$\frac{R_g^2}{a^2} = \frac{D(D+1)}{2} \qquad (33)$$

The volume of the polymer v_p is also determined by the upper and lower scales, a and b. The precise relationship is derived by equating the 3D integral of the covariogram $K_p(r)$ to v_p^2. The resulting expression is

$$\frac{v_p}{b^3} = 4\pi\Gamma[D]\left(\frac{a}{b}\right)^D \qquad (34)$$

where $\Gamma[]$ denotes the gamma function. It is important to note that the specific dependence of v_p on the polymer's overall size a and its building blocks b supports the interpretation of D as a fractal dimension.

The value of $I_p(Q)$, calculated as the Fourier transform of $\bar{C}_p(r)$ in equation (20), is plotted in **Fig. 36** for the specific parameters R_g = 300 Å, b = 1 Å, D = 2.5, and three different polymer fractions φ_p. The scattering intensity $I_p(Q)$ shows a plateau at low Q (less than approximately $1/R_g$), followed by a distinctive Q^{-D} scattering for intermediate Q values. The model theoretically converges to a Porod-like Q^{-4} scattering at Q values larger than about $1/b$.

However, from a physical perspective, this is unrealistic because the concept of a polymer phase with homogeneous scattering-length density breaks down at the molecular scale *b*. The presence of a Porod region for asymptotically large *Q* is a mathematical consequence of the linearity of equation (32) for asymptotically small *r*.

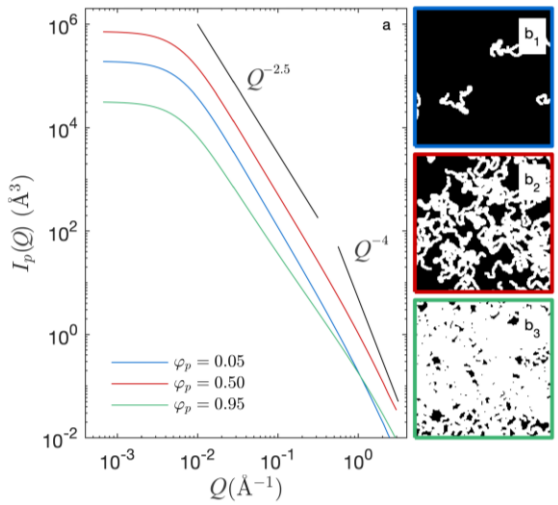

Figure 36. **Panel a**: The small-angle scattering cross section of the Boolean polymer model, calculated as the Fourier transform of equation (16) using the covariogram from equation (17), is shown for three different polymer volume fractions φ_p. **Panels b₁-b₃:** Two-dimensional sketches illustrate the varying degrees of coil overlap at the specified volume fractions. The model parameters include a radius of gyration R_g =300 Å and a lower cutoff size b = 1 Å.

For practical data analysis, these considerations are inconsequential because they involve *Q* values that are not typically measured in small-angle scattering experiments. A more significant and intriguing aspect of the scattering patterns in **Fig. 36** is their non-monotonic dependence on the polymer fraction (or concentration) φ_p. The scattering intensity is minimal for φ_p values near 0 or 1, and it reaches a maximum around $\varphi_p \cong 0.5$, which is expected behavior for any two-phase system.

7.5. Model for SANS data analysis

The general approach for calculating the scattering cross section of a two-scale system, which includes (i) a large-scale mesoporous structure and (ii) a small-scale substructure of the solid skeleton, is outlined in Section 7.3. A specific model describing the skeleton substructure as a high concentration polymer solution or hydrogel is detailed in Section 7.4. Here, these two models are combined to analyze the SANS data of the alginate aerogels shown in **Fig. 33.** In practice, the data are fitted using equation (29) in the following form:

$$I(Q) = A \times \left\{ \left[\varphi_w + \frac{b_p}{b_w - b_p} \right]^2 \frac{I_s(Q)}{\phi_s} + I_p(Q, \varphi_w) \right\} \quad (35)$$

A is a numerical factor accounting for the measurements on a relative scale (i.e., the unknown absolute intensity of the incoming beam and the volume of the irradiated sample). Additionally, *A* includes the contrast $\left(b_w - b_p\right)^2$ from equation (29), as well as the skeleton fraction ϕ_s.

Many of the parameters in equation (35) are known. A central parameter is φ_w, which influences both the wet polymer scattering $\left[I_p(Q, \varphi_w)\right]$ and the large-scale skeleton scattering through its contrast with the empty pores (the bracketed factor in the first term). The value of φ_w is determined from the macroscopic amount of water in the sample, as described in equation (20).

The scattering-length densities b_p and b_w are calculated from the sample composition.[5] The alginate aerogel under consideration, prepared according to specific procedures, has an overall composition corresponding to the molecular formula $C_{12}H_{14}CaO_{12}$, with only Ca^{2+} as counterions. Based on this composition and the density of alginate ($\rho = 2.02\ g/cm^3$)[50], its scattering-length density b_p is calculated. This value is compared with the scattering-

length density of heavy water b_w. Using these values, the contrast term in equation (35) is determined as follows:

$$\frac{b_p}{b_w - b_p} \cong 0.98 \qquad (36)$$

The positive value indicates that the scattering contrast of the skeleton increases as the water fraction φ_w increases.

Based on the composition of the alginate dimer and the polymer density, the volume of individual dimers can be estimated to be 332 Å^3.[5] Assuming an average of 500 dimers per polymer, this results in an average molecular volume of $v_p \cong 161\,000$ Å^3 for the alginate polymer.

Both rheological and scattering measurements indicate that alginate polymers in the dilute solution regime have radii of gyration ranging from 200 to 400 Å. Specifically, a R_g of 250 Å has been reported for alginate chains containing approximately 500 dimeric units.[164] Using these values of R_g and v_p, the parameters *a* and *b* of the Boolean polymer model are calculated using equations (33) and (34).

The remaining parameters for fitting in equation (35) are those that characterize the structure of the aerogel skeleton through $I_s(Q)$.

7.5.1. Skeleton by the cylinder model

From a scattering perspective, the main characteristics of the dry aerogel are Q^{-1} scattering in the low *Q* range and Q^{-4} scattering in the high *Q* range. This type of scattering is typical for fibrous structures, and to analyze it, a specific model for the skeleton is required. Considering the observed characteristic scattering pattern in the dry aerogel (**Fig. 33**) and its high

porosity (approximately 98%), the skeleton is modeled as a dilute suspension of elongated cylinders.

In the case where the cylinders are much longer than they are wide (for Ca(II)-alginate gels the length-to-width ratio is approximately 100:1[147]), the classical expression for the form factor simplifies as[97]

$$I_{cylinder}(Q) = \frac{\pi^2 R^2}{Q}\left[2\frac{J_1(QR)}{QR}\right]^2 \qquad (37)$$

In this expression, J_1 is the Bessel function of the first kind of order 1, and R is the radius. It is important to mention that in equation (37) the form factor is expressed per unit volume of the cylinder. Equation (37) shows oscillations that are absent in the data, which can be reduced by introducing polydispersity. Assuming a radius distribution $f_L(R)$, the form factor becomes:

$$I_{cylinder}(Q) = \frac{1}{\pi\langle R^2\rangle}\frac{4\pi^3}{Q^3}\int_0^\infty R^2 f_L(R)\,[J_1(QR)]^2 dR \qquad (38)$$

where

$$\langle R^2\rangle = \int_0^\infty f_L(R) R^2 dR \qquad (39)$$

is the second moment of the radius distribution. The division by $\pi\langle R^2\rangle$ in equation (38) is necessary to express the scattering per unit volume of the cylinders. Note that f_L represents a length-weighted distribution. In the following, a lognormal distribution is assumed as,

$$f_L(R) = \frac{1}{p\sqrt{2\pi R}}\,exp\left[-\frac{1}{2}\left(\frac{ln(R/R_m)}{p}\right)^2\right] \qquad (40)$$

where R_m is the median radius and p is a dimensionless polydispersity index. For further purposes, it is useful to note the following relationship between the moments of $f_L(R)$ and the parameters p and R_m,

$$\langle R^n \rangle = (R_m)^n exp[(np)^2/2] \quad (41)$$

Specifically, this relationship indicates that the polydispersity index is related to the radius variance via $\sigma_R^2/\langle R^2 \rangle = exp(p^2) - 1$. The monodisperse case corresponds to $p = 0$, and for $p = 0.83$, the standard deviation of the radius equals the mean radius.

Since the expressions for the scattering intensity were derived per unit volume of the cylinders, the skeleton scattering in equation (35) is modeled directly as

$$\frac{I_s(Q)}{\phi_s} = I_{cylinder}(Q) \quad (42)$$

However, it should be noted that upon the hydration of the alginate aerogel, the characteristic scattering patterns of the elongated cylinders gradually vanish. For water contents higher than about 0.6 g/g, the scattering patterns exhibit no plateau at low Q (see **Fig. 33.**). In these cases, the characteristic size of the skeleton is larger than the resolution of the SANS, and no specific shape can be attributed to it.

7.5.2. Skeleton by the Porod model

As the characteristic size of the skeleton is beyond the measurement range above a certain water content, only the scattered intensity from its surface can be observed. Therefore, it is sufficient to consider only Porod's asymptotic value of $I_s(Q)$, as

$$I_s(Q) \cong \frac{2\pi a_s}{Q^4} \quad (43)$$

where a_s is the specific area of the skeleton surface, independent of the skeleton morphology.[98, 165] In this scenario, equations (35) and (43) leave the mean chord length of the skeleton, l_s, as the only fitting parameter, defined by its volume-to-surface ratio, as follows:

$$l_s = \frac{4\phi_s}{a_s} \quad (44)$$

Using equations (43) and (44), the skeleton scattering in equation (35) is simplified as follows:

$$\frac{I_s(Q)}{\phi_s} = \frac{8\pi}{l_s Q^4} \quad (45)$$

The geometric significance of l_s can be understood by conceptually drawing a random infinite line through the sample and measuring the average length of its intercepts with the solid skeleton.[153, 156, 166]

7.6. Fit results and their interpretation

The SANS data of the dry aerogel, fitted using the cylinder model (equation 27), is shown in **Fig. 37a.** The fit was obtained for a median radius $R_m \cong 14$ Å and a polydispersity $p \cong 0.5$. A slight upward deviation of the data from the fit at low *Q* suggests a structure factor effect that was not accounted for, but the overall fit quality is good.

To further validate the fit, assuming that the overall surface of the aerogel is the sum of the surfaces of the individual fibrils, the specific surface area is calculated as

$$S = \frac{A}{m} = \frac{2\pi\langle R\rangle L}{\rho_p\langle R^2\rangle \pi L} = \frac{2\langle R\rangle}{\rho_p\langle R^2\rangle} \quad (46)$$

where ρ_p is the density of the solid alginate, and $\langle R\rangle$ and $\langle R^2\rangle$ are calculated through equation (41). The fitted parameters correspond to a specific surface area of 470 m^2/g, which is reasonably close to the BET surface area of 544 ± 70 m^2/g measured on the same sample.[5]

The same cylinder model was then used to describe the skeleton contribution in alginate samples with increasing water contents, with the polydispersity index p fixed at 0.5 and the median radius R_m as the only adjustable parameter. It is worth mentioning that when using the Porod's law for the skeleton contribution, there is also only one adjustable parameter, l_s.

The fits of the alginate aerogel SANS data, using either the cylinder or Porod model, are shown in **Fig. 37** as dashed and solid lines, respectively. Notable deviations from Porod scattering are observed at low Q for water contents below 0.6 g/g. This indicates that, at these lower water contents, the characteristic size of the skeleton is sufficiently small to scatter within the measured Q range. Within this range, only the cylinder model provides satisfactory fits.

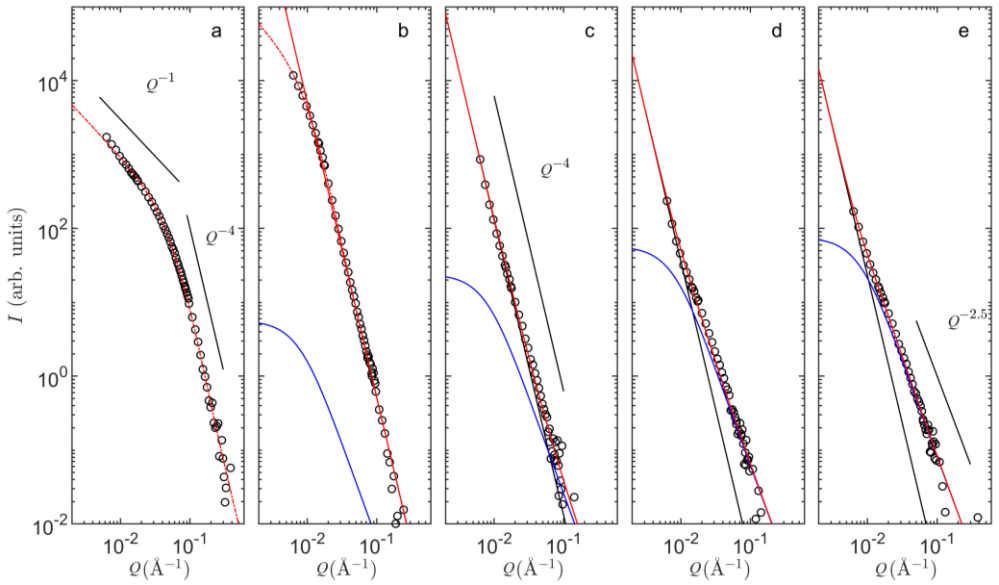

Figure 37. SANS data fits for alginate aerogel with increasing water content are as follows: (**a**) dry aerogel, (**b**) 0.33 g/g, (**c**) 0.68 g/g, (**d**) 1.1 g/g, and (**e**) 1.9 g/g. The solid lines represent the Porod model, while the dashed lines are for the cylinder model (the two models cannot be distinguished at higher water contents). The scattering contributions are displayed for the polymer solution (hydrogel) (**blue**) and the skeleton (**black**), along with their sum (**red**). The highlighted power laws play a significant role in the discussion.

The fitted values of the chord length l_s and the mean radius R_m are shown in **Fig. 38a**. The fitted values of R_m indicate a two-stage wetting process. For water contents below approximately 0.6 g/g, the volume of the individual fibers grow slightly, reaching a radius of 10 nm (see inset of **Fig. 38a**). At higher water contents, the growth becomes more significant with extensive aggregation, with fiber radii extending into the micrometer range. Only this latter stage can be analyzed using the Porod model. The fitted values of l_s are also in the micrometer range.

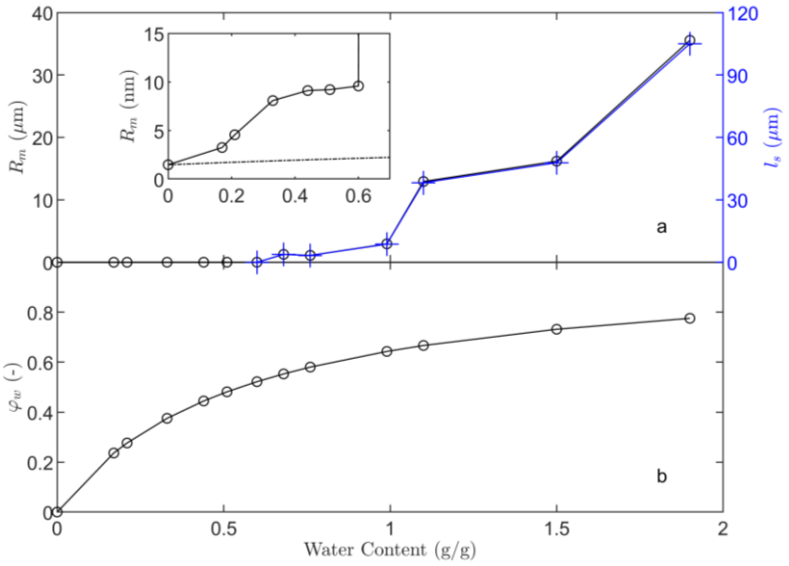

Figure 38. **Panel a:** Estimated parameters from fitting SANS patterns of alginate aerogel, shown as a function of water content: the mean skeleton chord length l_s (**blue, right axis**) and the median fiber radius R_m (**black, left axis**). The inset provides a magnified view of R_m, with the dashed line indicating the expected size due to fiber swelling alone. **Panel b:** The water fraction in the skeleton φ_w, calculated using equation (20) and applied in the fitting process.

It is useful to convert the fitted fiber parameters to an average chord length to compare the two fitting approaches in the high-water-content region. For an isolated object with volume V and area A, equation (44) gives $l_s = 4V/A$.[167, 168] Calculating the volume-to-area ratio for long cylinders, the average chord length from the fitted cylinder model is

$$l_s = \frac{2\langle R^2 \rangle}{\langle R \rangle} \quad (47)$$

With a polydispersity index of $p = 0.5$, equation (41) indicates that the average chord length of the cylinders is about three times the median radius R_m. This relationship is well-supported by the data in **Fig. 38a**, where the blue and black lines are nearly indistinguishable on the scale of the figure.

It may seem surprising to determine such large sizes using a SANS setup where the lowest Q corresponds to $2\pi/Q \cong 100\ nm$. However, l_s is

determined by analyzing the relative contributions of the skeleton Q^{-4} scattering and the polymer $Q^{-2.5}$ scattering, as clearly shown in **Figs. 37c to 37e.** It is important to emphasize that the size of the skeleton is deduced from the intensity of its Porod scattering (proportional to Q^{-4} and related to the skeleton's outer surface area), relative to the hydrogel-like scattering of its inner structure (proportional to $Q^{-2.5}$ and related to the skeleton's volume). For high water contents, the skeleton size is estimated as a volume-to-surface ratio, which is why it can be expressed as an average chord length, l_s.

The SANS data analysis reveals that the wetting of alginate aerogels occurs in two distinct stages. In the first stage, with water contents below approximately 0.6 g/g, the fibers of the skeleton undergo a tenfold thickening from the dry radius R_m of 14 Å to about 100 Å (see inset of **Fig. 38a**). The thickening expected from swelling alone, as water molecules penetrate and increase the skeleton's volume, can be estimated as

$$R_m \cong R_m^{(dry)}\sqrt{1+V} \quad (48)$$

assuming cylindrical shapes and using the same volume V as in equation (21), which represents the macroscopic water-to-polymer volume ratio. This specific dependence is shown as a dashed line in the inset of **Fig. 38a.** Since equation (48) significantly underestimates the observed thickening, it is evident that the fibrils in the dry aerogel not only swell but also aggregate into larger, yet still nanometer-sized structures.

Previous solid-state and liquid-phase NMR results provide additional molecular-scale insights that complement the mesoscale scenario derived from SANS data. Notably, for water contents below 0.4 g/g, it was found that water absorption into the alginate fibrils hydrates the supramolecular assembly of alginate chains and induces the rearrangement of their tertiary and quaternary structures.[5] Interestingly, the compressive strength of the calcium-alginate

aerogel significantly increases at these low hydration levels. Theoretical studies attribute this increase to the same fibril aggregation inferred from SANS.[142, 169] Additionally, the NMR relaxation time associated with the hydration sphere of the polymer chains begins to increase sharply above a water content of 0.4 g/g, indicating that the fibers start to swell and form a concentrated polymer solution.[5] As the water content increases further, SANS reveals a dramatic structural change around 0.6 g/g. When the water content rises from 0.5 to 0.7 g/g, the characteristic size of the skeleton increases by more than two orders of magnitude, from nanometers to micrometers (**Fig. 38a**). This hundredfold increase in skeleton size occurs with minimal change in its water content, with the volume fraction φ_w increasing by less than 10% as the water content increases from 0.5 to 0.7 g/g. Thus, the dramatic increase in l_s results from a major rearrangement and merging of the skeleton domains, significantly reducing their total outer surface area while their volume remains nearly unchanged.

The suddenness of this transition may be explained by a percolation phenomenon, where a slight increase in the size of the skeleton domains brings many into contact. Additionally, capillary forces increase with higher water content, placing the skeleton under strong compressive stress, making the nanostructure of a wet aerogel inherently unstable and prone to collapse. All these effects imminently lead to the formation of an extensive homogeneous hydrogel from the hydrated individual fibers.

8. Summary and outlook

During my doctoral research, two different types of aerogels with potential biomedical applications were investigated. The newly synthesized borosilicate-PVA hybrid aerogels have potential use in bone regeneration, while calcium-alginate aerogels are intended for wound treatment and drug delivery. The presented Ph.D. research focused on investigating the nanoscale structural characteristics of these aerogels that determine their applicability in the targeted fields.

The synthesis of the new borosilicate-PVA hybrid gels was performed by applying co-gelatin in the sol-gel method. Nanostructured monolithic functionalized aerogels were then prepared from these hydrogels by performing solvent exchange and drying in supercritical CO_2 (**Fig. 6.**). To investigate the effect of the PVA chain length on the structural characteristics, three types of PVAs with different molar masses were used. Additionally, different Ca(II) sources, including $CaCl_2$, β-$Ca_3(PO_4)_2$, and hydroxyapatite, were incorporated into the hybrid aerogels. The incorporation of these Ca(II) sources aimed to enhance the biological activity of the aerogels in practical bone regeneration applications.

The nanoscale features of the aerogels were carefully analyzed as a function of the molar mass of the PVA component and the type of Ca(II) source. Infrared and solid-state NMR spectroscopy revealed that covalent bonding occurs only between boric acid and PVA, with no primary chemical bonding between the other components (SiO_2, B_2O_3, PVA) in the gel backbone. Despite this, contrast variation SANS measurements demonstrated the formation of a structurally homogeneous hybrid on the sub-nanometer scale. Therefore, the developed synthesis method ensures that the hydrolysis of the inorganic precursors and their co-condensation with each other and with

the PVA macromolecules occur at similar reaction rates, leading to a homogeneous hybrid backbone.

Despite hybridizing the silica backbone with PVA, the fundamental morphological characteristics of typical silica aerogels are preserved, even with the incorporation of a Ca(II) source. The hybrid aerogels remain primarily mesoporous, although the pore size distribution is influenced by the molar mass of PVA and the Ca(II) content. Both β-$Ca_3(PO_4)_2$ and hydroxyapatite are fully incorporated into the hybrid backbone during synthesis, maintaining their original size and crystalline form. In contrast, the addition of $CaCl_2$ results in the formation of larger aggregates within the solid skeleton compared to the other cases and is incorporated in a form distinct from its original state.

Small-angle neutron scattering measurements confirmed that the morphological properties of the hybrid aerogels are maintained during wetting, even with the incorporation of hydroxyapatite. When suspended in aqueous media, the aerogels exhibit small negative ζ-potentials, which generally favor cell adhesion. In vitro time-lapse video microscopy experiments demonstrated the non-toxic nature of the hybrid gels. MG-63 osteosarcoma cells and dental pulp stem cells attached to the suspended aerogel particles when the cell monolayer was scratched, gradually incorporating the particles into the damaged region. Additionally, it was observed that an increasing Ca(II) content accelerated the monolayer formation when uniform particle concentrations were used. Due to this bioactivity, the nanostructured hybrid aerogel microparticles show promise in the form of a suspension for promoting bone regeneration. However, in vivo tests are needed for further development.

A previous study on the wetting of an archetypical calcium-alginate aerogel resulted in a qualitative model for the hydration of this material, but the quantitative understanding of the structural changes remained unclear.[5] Our goal was to create a structurally realistic mathematical model for quantitatively

analyzing small-angle scattering patterns during the progressive hydration of alginate aerogels, transitioning from a dry mesoporous solid to a fully hydrated gel composed of dissolved macromolecules. Our model accurately captures the main nanoscale structural and scattering characteristics of the wet aerogel samples. It is based on robust material properties, such as the BET surface area of the dry aerogel, the radius of gyration of the polymer chains, and the molecular volume of the hydrated alginate. Additionally, our model is simple enough to fit the complete SANS data set using a single adjustable parameter that clearly represents the size of the hydrated gel skeleton.

To achieve this goal, the hydration-induced structural changes were investigated at two structural levels. To gain insights into the inner structural changes, where the dry, dense polymer structure transforms into a hydrogel structure, a new model was developed. A Boolean model was used, in which the grains represent the alginate polymers, whose properties were determined using previously published data on alginate polymers. The second structural level describes the size change of the skeleton during wetting. For this purpose, two models were employed: the Porod approximation and the cylinder model. The cylinder model is applicable across the entire experimental range, while the Porod model is only suitable for higher water content, where only the surface scattering of the skeleton is observed. The two models yield nearly identical skeleton sizes in the higher water content region, supporting their applicability. Using this newly developed model, the two-stage wetting mechanism of the alginate aerogel is well described. In the first stage, the thickening of the radius of the primary fibrils from 14 Å to 100 Å is observed. In the second stage, a micrometer-sized skeleton is formed due to significant rearrangement and merging of the skeleton domains

The model we developed to analyze small-angle scattering patterns is more general than describing only the specific case of the alginate aerogel

studied here. However, demonstrating the model's applicability to describe the wetting of other aerogels requires new experimental measurements. Theoretically, this model could be useful for describing the wetting of aerogels with similar chemical structures and morphological properties to alginate aerogels. In particular, it could be applied to study the wetting of other polysaccharide aerogels with fibrous nanostructures, as their molecular interactions with water and the rearrangement of their polymer tertiary and quaternary structures result in similar morphological changes.

Interestingly, many structural changes observed during the wetting of aerogels are expected to occur in reverse order during the drying of solvated gels. This is particularly relevant to the supercritical solvent extraction process central to aerogel production. If such a study is undertaken, it will undoubtedly present new challenges in scattering data analysis. It is hoped that the present work will be helpful in this context as well.

9. Összefoglalás

Doktori kutatásom során két különböző típusú aerogélt vizsgáltam, amelyek felhasználása az orvosbiológia területén lehetségesek. Az újonnan előállított boroszilikát-PVA hibrid aerogélek a csontregeneráció területén, míg a kalcium-alginát aerogélek sebkezelésre, illetve gyógyszerhordozó-rendszerként alkalmazhatók. A PhD kutatásom ezen anyagok nanoszerkezeti jellemzőinek vizsgálatára irányult, amelyek meghatározzák a minták alkalmazhatóságát az adott célterületen.

Sikeresen szintetizáltam új boroszilikát-PVA hibrid géleket szol-gél eljárás segítségével, amelyeket aztán egy többlépéses oldószercsere eljárást követően szuperkritikus körülmények között szárítottam ki, így előállítva a hibrid aerogéleket (**6. ábra**). A szintézis során három különböző molekulatömeggel rendelkező PVA-t alkalmaztam annak érdekében, hogy vizsgálhassuk a PVA lánchosszának a szerkezetre gyakorolt hatását. Az aerogélek bioaktivitásának növelése érdekében különböző kalcium forrásokat ($CaCl_2$, β-$Ca_3(PO_4)_2$, és hidroxiapatit) is beépítettem a hibrid gélvázba.

Részletesen vizsgáltuk az előállított aerogélek nanoszerkezeti tulajdonságait, különös tekintettel a PVA lánchosszának, illetve a Ca(II) forrásnak a hatását. Az infravörös és szilárd-fázisú NMR spektroszkópiai mérések kimutatták, hogy kovalens kötés csak a bórsav és a PVA között jön létre, a többi komponens (SiO_2, B_2O_3, PVA) között viszont nincs elsődleges kémiai kötés. Ennek ellenére a kontrasztvariációs SANS mérések bizonyították a homogén hibrid szerkezet kialakulását a nanométeres mérettartományban. Ezek alapján elmondhatjuk, hogy az általunk kidogozott szintézismódszer biztosítja a valós hibrid szerkezet kialakulását, még annak ellenére is, hogy az egyes komponensek között nem alakul ki elsődleges kémiai kötés.

Az aerogélek a hibridizáció ellenére is megőrzik a szilika aerogélekre jellemző alapvető morfológiai tulajdonságaikat, még a Ca(II) forrás beépülése esetén is. A hibrid aerogélek elsősorban mezopórusosak maradnak, bár a pórusméret-eloszlást befolyásolja a PVA moláris tömege és a Ca(II) tartalom. A szintézis során mind a β-$Ca_3(PO_4)_2$, mind a hidroxiapatit teljes mértékben beépül a hibrid gélvázba, megőrizve eredeti méretüket és kristályszerkezetüket. Ezzel ellentétben a $CaCl_2$ alkalmazása a többi esethez képest nagyobb aggregátumok képződését eredményezi a gélvázban, valamint az eredeti állapotától eltérő formában épül be.

Kisszögű neutronszórási mérések igazolták, hogy a hibrid aerogélek megőrzik eredeti morfológiai tulajdonságaikat vizes közegben, még a hidroxiapatit beépítése esetén is. Különböző pH-jú közegekben vizsgálva a szuszpendált gél részecskéket kis negatív ζ-potenciálokat tudtunk mérni, amelyek a sejtadhézió szempontjából kedvezőek. *In vitro* videómikroszkópos kísérletek bizonyították a hibrid gélek nem-toxikus természetét, valamint a szuszpendált részecskék kedvező sejtadhéziós tulajdonságait. Továbbá megfigyelhető volt, hogy a növekvő Ca(II)-tartalom elősegítette a monoréteg képződését. Ezen eredmények alapján a nanostrukturált hibrid aerogél mikrorészecskék szuszpenzió formájában ígéretes jelöltek a csontregeneráció elősegítésére. Valós alkalmazásukhoz azonban további *in vivo* kísérletek szükségesek.

Egy korábbi tanulmányban kutatók sikeresen dolgoztak ki egy kvalitatív modellt egy archetipikus kalcium-alginát aerogél nedvesítése során bekövetkező szerkezeti változásokra, ugyanakkor a nedvesítés során bekövetkező változások kvantitatív leírása tisztázatlan maradt.[5] A célunk az volt, hogy egy fizikailag valósághű matematikai modellt dolgozzunk ki a kalcium-alginát aerogél nedvesítése során fellépő kisszögű neutronszórási mintázatok kvantitatív elemzésére. A modell kidolgozása során feltételeztük,

hogy az aerogél szerkezete a nedvesítés során egy száraz mezopórusos anyagból fokozatosan átalakul egy hiratált makromolekulákból álló duzzadt géllé. A modell figyelembe veszi a váz méretbeli változása mellett annak belső szerkezeti változását is a nedvesítés során. A modell kidolgozásához a minta olyan anyagi tulajdonságait is felhasználtuk, mint a száraz aerogél BET fajlagos felülete, valamint az „oldott" makromolekula girációs sugara és térfogata. Ezek ismeretében sikerült egy olyan egyszerű modellt kidolgoznunk, amely segítségével a teljes SANS mérési sorozat egyetlen paraméter, a hidratált váz méretének változtatásával illeszthető.

A hidratáció által kiváltott szerkezeti változásokat két strukturális szinten vizsgáltuk. Annak érdekében, hogy betekintést nyerjünk a belső szerkezeti változásokba, ahol a száraz, sűrű polimer hálózat átalakul egy hidrogélszerű szerkezetté, egy új modellt dolgoztunk ki. A Boole-modell alkalmazása során az alginát polimereket használtuk motívumokként, amelyek anyagi tulajdonságait korábban publikált adatok alapján határoztuk meg. A második szerkezeti szint a váz méretváltozását írja le a nedvesítés során. Erre a célra két modellt alkalmaztunk: a Porod-közelítést és a hengermodellt. A hengermodell a teljes kísérleti tartományban alkalmazható, míg a Porod-modell csak nagyobb víztartalom esetén alkalmas, ahol csak a váz felületéről származó szórás figyelhető meg. A két modellel közel azonos vázméretet tudtunk meghatározni a nagyobb víztartalmú régióban, ami megerősíti a két modell alkalmazhatóságát. Ezzel az újonnan megalkotott, két strukturális szinten történő változásokat figyelembe vevő modellel jól leírható az alginát aerogél kétlépcsős nedvesítési mechanizmusa. Az első szakaszban a polimer szálak sugara 14 Å-ről 100 Å-re nő, míg a második szakaszban az egyes váz domének jelentősen átrendeződnek és összeolvadnak, amelynek következtében mikrométeres objektumok keletkeznek.

Az általunk kidolgozott SANS modell nem csupán a vizsgált kalcium-alginát aerogél nedvesedése során bekövetkező változások leírására alkalmas, attól jóval általánosabb. Gyakorlati szempontból ennek bizonyításához más rendszerek SANS vizsgálata szükséges, ugyanakkor elméleti szempontból ez a modell hasznos lehet a hasonló kémiai szerkezettel és morfológiai tulajdonságokkal rendelkező, például más szálas szerkezetű poliszacharid aerogélek esetében. Ezen esetekben a polimer vízzel történő molekuláris kölcsönhatása, és az ezáltal okozott tercier és kvaterner szerkezeti átrendeződések hasonló morfológiai változásokat eredményezhetnek.

Feltételezve, hogy az aerogélek nedvesítése során megfigyelt szerkezeti változások a gélek szárítása során várhatóan fordítottan történik, az általunk kidolgozott modell ennek vizsgálatában is hasznos lehet. Ezen szerkezeti változások tanulmányozása különösen fontos, tekintve, hogy a szuperkritikus szárítás az aerogél-gyártás kulcseleme.

10. References

1. Patzkó, Á., *A kolloidika alapjai*. József Attila Tudományegyetem: Szeged, **1998**.

2. Aegerter, M. A.; Leventis, N.; Koebel, M.; Steiner III, S. A., *Springer Handbook of Aerogels*. Springer Nature: **2023**.

3. Gomollón-Bel, F., IUPAC Top Ten Emerging Technologies in Chemistry 2022. *Discover the innovations that will transform energy, health, and materials science, to tackle the most urgent societal challenges and catalyse sustainable development.* **2022,** *44* (4), 4-13. **10.1515/ci-2022-0402**

4. Pang, L.; Shen, Y.; Hu, H.; Zeng, X.; Huang, W.; Gao, H.; Wang, H.; Wang, D., Chemically and physically cross-linked polyvinyl alcohol-borosilicate gel hybrid scaffolds for bone regeneration. *Materials Science and Engineering: C* **2019,** *105*, 110076. **10.1016/j.msec.2019.110076**

5. Forgács, A.; Papp, V.; Paul, G.; Marchese, L.; Len, A.; Dudás, Z.; Fábián, I.; Gurikov, P.; Kalmár, J., Mechanism of Hydration and Hydration Induced Structural Changes of Calcium Alginate Aerogel. *ACS Applied Materials & Interfaces* **2021,** *13* (2), 2997-3010. **10.1021/acsami.0c17012**

6. Kistler, S. S., Coherent Expanded Aerogels and Jellies. *Nature* **1931,** *127* (3211), 741-741. **10.1038/127741a0**

7. Kistler, S. S., Coherent Expanded-Aerogels. *The Journal of Physical Chemistry* **1932,** *36* (1), 52-64. **10.1021/j150331a003**

8. Kirkbir, F.; Murata, H.; Meyers, D.; Chaudhuri, S. R., Drying of aerogels in different solvents between atmospheric and supercritical pressures. *Journal of Non-Crystalline Solids* **1998,** *225*, 14-18. **10.1016/S0022-3093(98)00003-9**

9. Lázár, I.; Fábián, I., A Continuous Extraction and Pumpless Supercritical CO2 Drying System for Laboratory-Scale Aerogel Production. *Gels* **2016,** *2* (4), 26. **10.3390/gels2040026**

10. van Bommel, M. J.; de Haan, A. B., Drying of silica aerogel with supercritical carbon dioxide. *Journal of Non-Crystalline Solids* **1995,** *186*, 78-82. **10.1016/0022-3093(95)00072-0**

11. Tewari, P.; Hunt, A.; Lofftus, K. In *Advances in production of transparent silica aerogels for window glazings*, Aerogels: Proceedings of the First International Symposium, Würzburg, Fed. Rep. of Germany September 23–25, 1985, Springer: 1986; pp 31-37.

12. Teichner, S. J.; Nicolaon, G. A.; Vicarini, M. A.; Gardes, G. E. E., Inorganic oxide aerogels. *Advances in Colloid and Interface Science* **1976,** *5* (3), 245-273. **10.1016/0001-8686(76)80004-8**

13. Cantin, M.; Casse, M.; Koch, L.; Jouan, R.; Mestreau, P.; Roussel, D.; Bonnin, F.; Moutel, J.; Teichner, S. J., Silica aerogels used as Cherenkov radiators. *Nuclear Instruments and Methods* **1974,** *118* (1), 177-182. **10.1016/0029-554X(74)90700-9**

14. Poelz, G.; Riethmüller, R., Preparation of silica aerogel for Cherenkov counters. *Nuclear Instruments and Methods in Physics Research* **1982,** *195* (3), 491-503. **10.1016/0029-554X(82)90010-6**

15. Pekala, R. W., Organic aerogels from the polycondensation of resorcinol with formaldehyde. *Journal of Materials Science* **1989,** *24* (9), 3221-3227. **10.1007/BF01139044**

16. Pekala, R. W.; Alviso, C. T., Carbon Aerogels and Xerogels. *MRS Online Proceedings Library* **1992,** *270* (1), 3-14. **10.1557/PROC-270-3**

17. Li, F.; Xie, L.; Sun, G.; Kong, Q.; Su, F.; Cao, Y.; Wei, J.; Ahmad, A.; Guo, X.; Chen, C.-M., Resorcinol-formaldehyde based carbon aerogel: Preparation, structure and applications in energy storage devices. *Microporous and Mesoporous Materials* **2019,** *279*, 293-315. **10.1016/j.micromeso.2018.12.007**

18. Smith, D. M.; Deshpande, R.; Jeffrey Brinker, C., Preparation of Low-Density Aerogels at Ambient Pressure. *MRS Online Proceedings Library* **1992,** *271* (1), 567-572. **10.1557/PROC-271-567**

19. Prakash, S. S.; Brinker, C. J.; Hurd, A. J., Silica aerogel films at ambient pressure. *Journal of Non-Crystalline Solids* **1995,** *190* (3), 264-275. **10.1016/0022-3093(95)00024-0**

20. Prakash, S. S.; Brinker, C. J.; Hurd, A. J.; Rao, S. M., Silica aerogel films prepared at ambient pressure by using surface derivatization to induce reversible drying shrinkage. *Nature* **1995,** *374* (6521), 439-443. **10.1038/374439a0**

21. Hüsing, N.; Schubert, U., Aerogels—Airy Materials: Chemistry, Structure, and Properties. *Angewandte Chemie International Edition* **1998,** *37* (1-2), 22-45. **10.1002/(SICI)1521-3773(19980202)37:1/2<22::AID-ANIE22>3.0.CO;2-I**

22. Pierre, A. C.; Pajonk, G. M., Chemistry of Aerogels and Their Applications. *Chemical Reviews* **2002,** *102* (11), 4243-4266. **10.1021/cr0101306**

23. Payanda Konuk, O.; Alsuhile, A. A. A. M.; Yousefzadeh, H.; Ulker, Z.; Bozbag, S. E.; García-González, C. A.; Smirnova, I.; Erkey, C., The effect of synthesis conditions and process parameters on aerogel properties. *Frontiers in Chemistry* **2023,** *11*. **10.3389/fchem.2023.1294520**

24. Parale, V. G.; Kim, T.; Choi, H.; Phadtare, V. D.; Dhavale, R. P.; Kanamori, K.; Park, H.-H., Mechanically Strengthened Aerogels through Multiscale, Multicompositional, and Multidimensional Approaches: A Review. *Advanced Materials* **2024,** *36* (18), 2307772. **10.1002/adma.202307772**

25. Pekala, R. W.; Alviso, C. T.; Kong, F. M.; Hulsey, S. S., Aerogels derived from multifunctional organic monomers. *Journal of Non-Crystalline Solids* **1992,** *145*, 90-98. **10.1016/S0022-3093(05)80436-3**

26. Dong, S.; Huang, G.; Su, M.; Huang, T., Environmentally Friendly Method: Development and Application to Carbon Aerogel as Sorbent for Solid-Phase Extraction. *ACS Applied Materials & Interfaces* **2015,** *7* (40), 22256-22263. **10.1021/acsami.5b05241**

27. Kabbour, H.; Baumann, T. F.; Satcher, J. H.; Saulnier, A.; Ahn, C. C., Toward New Candidates for Hydrogen Storage: High-Surface-Area Carbon Aerogels. *Chemistry of Materials* **2006,** *18* (26), 6085-6087. **10.1021/cm062329a**

28. Chidambareswarapattar, C.; McCarver, P. M.; Luo, H.; Lu, H.; Sotiriou-Leventis, C.; Leventis, N., Fractal Multiscale Nanoporous Polyurethanes: Flexible to Extremely Rigid Aerogels from Multifunctional Small Molecules. *Chemistry of Materials* **2013,** *25* (15), 3205-3224. **10.1021/cm401623h**

29. Leventis, N.; Sotiriou-Leventis, C.; Mohite, D. P.; Larimore, Z. J.; Mang, J. T.; Churu, G.; Lu, H., Polyimide Aerogels by Ring-Opening Metathesis Polymerization (ROMP). *Chemistry of Materials* **2011,** *23* (8), 2250-2261. **10.1021/cm200323e**

30. Malakooti, S.; Rostami, S.; Churu, H. G.; Luo, H.; Clark, J.; Casarez, F.; Rettenmaier, O.; Daryadel, S.; Minary-Jolandan, M.; Sotiriou-Leventis, C.; Leventis, N.; Lu, H., Scalable, hydrophobic and highly-stretchable poly(isocyanurate–urethane) aerogels. *RSC Advances* **2018,** *8* (38), 21214-21223. **10.1039/C8RA03085E**

31. Meador, M. A. B.; Alemán, C. R.; Hanson, K.; Ramirez, N.; Vivod, S. L.; Wilmoth, N.; McCorkle, L., Polyimide Aerogels with Amide Cross-Links: A Low Cost Alternative for Mechanically Strong Polymer Aerogels. *ACS Applied Materials & Interfaces* **2015,** *7* (2), 1240-1249. **10.1021/am507268c**

32. Meador, M. A. B.; Malow, E. J.; Silva, R.; Wright, S.; Quade, D.; Vivod, S. L.; Guo, H.; Guo, J.; Cakmak, M., Mechanically Strong, Flexible Polyimide Aerogels Cross-Linked with Aromatic Triamine. *ACS Applied Materials & Interfaces* **2012,** *4* (2), 536-544. **10.1021/am2014635**

33. Williams, J. C.; Meador, M. A. B.; McCorkle, L.; Mueller, C.; Wilmoth, N., Synthesis and Properties of Step-Growth Polyamide Aerogels Cross-linked with Triacid Chlorides. *Chemistry of Materials* **2014,** *26* (14), 4163-4171. **10.1021/cm5012313**

34. Ganesan, K.; Ratke, L., Facile preparation of monolithic κ-carrageenan aerogels. *Soft Matter* **2014,** *10* (18), 3218-3224. **10.1039/C3SM52862F**

35. Groult, S.; Budtova, T., Tuning structure and properties of pectin aerogels. *European Polymer Journal* **2018,** *108*, 250-261. **10.1016/j.eurpolymj.2018.08.048**

36. Martins, M.; Barros, A. A.; Quraishi, S.; Gurikov, P.; Raman, S. P.; Smirnova, I.; Duarte, A. R. C.; Reis, R. L., Preparation of macroporous alginate-based aerogels for biomedical applications. *The Journal of Supercritical Fluids* **2015,** *106*, 152-159. **10.1016/j.supflu.2015.05.010**

37. Tan, C.; Fung, B. M.; Newman, J. K.; Vu, C., Organic Aerogels with Very High Impact Strength. *Advanced Materials* **2001,** *13* (9), 644-646. **10.1002/1521-4095(200105)13:9<644::AID-ADMA644>3.0.CO;2-#**

38. Wei, S.; Ching, Y. C.; Chuah, C. H., Synthesis of chitosan aerogels as promising carriers for drug delivery: A review. *Carbohydrate Polymers* **2020,** *231*, 115744. **10.1016/j.carbpol.2019.115744**

39. Zhu, F., Starch based aerogels: Production, properties and applications. *Trends in Food Science & Technology* **2019,** *89*, 1-10. **10.1016/j.tifs.2019.05.001**

40. López-Iglesias, C.; Barros, J.; Ardao, I.; Gurikov, P.; Monteiro, F. J.; Smirnova, I.; Alvarez-Lorenzo, C.; García-González, C. A., Jet Cutting Technique for the Production of Chitosan Aerogel Microparticles Loaded with Vancomycin. *Polymers* **2020,** *12* (2), 273.

41. Betz, M.; García-González, C. A.; Subrahmanyam, R. P.; Smirnova, I.; Kulozik, U., Preparation of novel whey protein-based aerogels as drug carriers for life science applications. *The Journal of Supercritical Fluids* **2012,** *72*, 111-119. **10.1016/j.supflu.2012.08.019**

42. Marin, M. A.; Mallepally, R. R.; McHugh, M. A., Silk fibroin aerogels for drug delivery applications. *The Journal of Supercritical Fluids* **2014,** *91*, 84-89. **10.1016/j.supflu.2014.04.014**

43. Selmer, I.; Kleemann, C.; Kulozik, U.; Heinrich, S.; Smirnova, I., Development of egg white protein aerogels as new matrix material for microencapsulation in food. *The Journal of Supercritical Fluids* **2015,** *106*, 42-49. **10.1016/j.supflu.2015.05.023**

44. Wang, J.; Zhao, D.; Shang, K.; Wang, Y.-T.; Ye, D.-D.; Kang, A. H.; Liao, W.; Wang, Y.-Z., Ultrasoft gelatin aerogels for oil contaminant removal. *Journal of Materials Chemistry A* **2016,** *4* (24), 9381-9389. **10.1039/C6TA03146C**

45. Ching, S. H.; Bansal, N.; Bhandari, B., Alginate gel particles–A review of production techniques and physical properties. *Critical Reviews in Food Science and Nutrition* **2017,** *57* (6), 1133-1152. **10.1080/10408398.2014.965773**

46. Alnaief, M.; Alzaitoun, M. A.; García-González, C. A.; Smirnova, I., Preparation of biodegradable nanoporous microspherical aerogel based on alginate. *Carbohydrate Polymers* **2011,** *84* (3), 1011-1018. **10.1016/j.carbpol.2010.12.060**

47. Duong, T.; Vivero-Lopez, M.; Ardao, I.; Alvarez-Lorenzo, C.; Forgács, A.; Kalmár, J.; García-González, C. A., Alginate aerogels by spray gelation for enhanced pulmonary delivery and solubilization of beclomethasone dipropionate. *Chemical Engineering Journal* **2024,** *485*, 149849. **10.1016/j.cej.2024.149849**

48. Veres, P.; Kéri, M.; Bányai, I.; Lázár, I.; Fábián, I.; Domingo, C.; Kalmár, J., Mechanism of drug release from silica-gelatin aerogel—Relationship between matrix structure and release kinetics. *Colloids and Surfaces B: Biointerfaces* **2017,** *152*, 229-237. **10.1016/j.colsurfb.2017.01.019**

49. Zhao, S.; Malfait, W. J.; Demilecamps, A.; Zhang, Y.; Brunner, S.; Huber, L.; Tingaut, P.; Rigacci, A.; Budtova, T.; Koebel, M. M., Strong, Thermally Superinsulating Biopolymer–Silica Aerogel Hybrids by Cogelation of Silicic Acid with Pectin. *Angewandte Chemie International Edition* **2015,** *54* (48), 14282-14286. **10.1002/anie.201507328**

50. Paraskevopoulou, P.; Smirnova, I.; Athamneh, T.; Papastergiou, M.; Chriti, D.; Mali, G.; Čendak, T.; Raptopoulos, G.; Gurikov, P., Polyurea-crosslinked biopolymer aerogel beads. *RSC Advances* **2020,** *10* (67), 40843-40852. **10.1039/D0RA07337G**

51. Paraskevopoulou, P.; Raptopoulos, G.; Len, A.; Dudás, Z.; Fábián, I.; Kalmár, J., Fundamental Skeletal Nanostructure of Nanoporous Polymer-Cross-Linked Alginate Aerogels and Its Relevance To Environmental Remediation. *ACS Applied Nano Materials* **2021,** *4* (10), 10575-10583. **10.1021/acsanm.1c02072**

52. Everett, D. H., Manual of Symbols and Terminology for Physicochemical Quantities and Units, Appendix II: Definitions, Terminology and Symbols in Colloid and Surface Chemistry. **1972,** *31* (4), 577-638. **10.1351/pac197231040577**

53. Ratke, L.; Gurikov, P., *The chemistry and physics of aerogels: synthesis, processing, and properties*. Cambridge University Press: **2021**.

54. Meti, P.; Mahadik, D. B.; Lee, K.-Y.; Wang, Q.; Kanamori, K.; Gong, Y.-D.; Park, H.-H., Overview of organic–inorganic hybrid silica aerogels: Progress and perspectives. *Materials & Design* **2022,** *222*, 111091. **10.1016/j.matdes.2022.111091**

55. Veres, P.; López-Periago, A. M.; Lázár, I.; Saurina, J.; Domingo, C., Hybrid aerogel preparations as drug delivery matrices for low water-solubility drugs. *International Journal of Pharmaceutics* **2015,** *496* (2), 360-370. **10.1016/j.ijpharm.2015.10.045**

56. Kéri, M.; Forgács, A.; Papp, V.; Bányai, I.; Veres, P.; Len, A.; Dudás, Z.; Fábián, I.; Kalmár, J., Gelatin content governs hydration induced structural changes in silica-gelatin hybrid aerogels – Implications in drug delivery. *Acta Biomaterialia* **2020,** *105*, 131-145. **10.1016/j.actbio.2020.01.016**

57. Reyes-Peces, M. V.; Fernández-Montesinos, R.; Mesa-Díaz, M. D.; Vilches-Pérez, J. I.; Cárdenas-Leal, J. L.; de la Rosa-Fox, N.; Salido, M.; Piñero, M. Structure-Related Mechanical Properties and Bioactivity of Silica–Gelatin Hybrid Aerogels for Bone Regeneration *Gels* [Online], 2023. **10.3390/gels9010067**

58. Ilhan, F.; Fabrizio, E. F.; McCorkle, L.; Scheiman, D. A.; Dass, A.; Palczer, A.; Meador, M. B.; Johnston, J. C.; Leventis, N., Hydrophobic monolithic aerogels by nanocasting polystyrene on amine-modified silica. *Journal of Materials Chemistry* **2006,** *16* (29), 3046-3054. **10.1039/B604323B**

59. Maleki, H.; Durães, L.; García-González, C. A.; del Gaudio, P.; Portugal, A.; Mahmoudi, M., Synthesis and biomedical applications of aerogels: Possibilities and challenges. *Advances in Colloid and Interface Science* **2016,** *236*, 1-27. **10.1016/j.cis.2016.05.011**

60. Bernardes, B. G.; Baptista-Silva, S.; Illanes-Bordomás, C.; Magalhães, R.; Dias, J. R.; Alves, N. M. F.; Costa, R.; García-González, C. A.; Oliveira, A. L., Expanding the Potential of Self-Assembled Silk Fibroin as Aerogel Particles for Tissue Regeneration. *Pharmaceutics* **2023,** *15* (11), 2605.

61. Iglesias-Mejuto, A.; García-González, C. A., 3D-printed alginate-hydroxyapatite aerogel scaffolds for bone tissue engineering. *Materials Science and Engineering: C* **2021,** *131*, 112525. **10.1016/j.msec.2021.112525**

62. Iglesias-Mejuto, A.; García-González, C. A., 3D-Printed, Dual Crosslinked and Sterile Aerogel Scaffolds for Bone Tissue Engineering. *Polymers* **2022,** *14* (6), 1211.

63. Méndez, D. A.; Schroeter, B.; Martínez-Abad, A.; Fabra, M. J.; Gurikov, P.; López-Rubio, A., Pectin-based aerogel particles for drug delivery: Effect of pectin composition on aerogel structure and release properties. *Carbohydrate Polymers* **2023,** *306*, 120604. **10.1016/j.carbpol.2023.120604**

64. Lovskaya, D.; Bezchasnyuk, A.; Mochalova, M.; Tsygankov, P.; Lebedev, A.; Zorkina, Y.; Zubkov, E.; Ochneva, A.; Gurina, O.; Silantyev, A.; Majouga, A.; Menshutina, N., Preparation of Protein Aerogel Particles for the Development of Innovative Drug Delivery Systems. *Gels* **2022,** *8* (12), 765.

65. Athamneh, T.; Hajnal, A.; Al-Najjar, M. A. A.; Alshweiat, A.; Obaidat, R.; Awad, A. A.; Al-Alwany, R.; Keitel, J.; Wu, D.; Kieserling, H.; Rohn, S.; Keil, C.; Gurikov, P., In vivo tests of a novel wound dressing based on agar aerogel. *International Journal of Biological Macromolecules* **2023,** *239*, 124238. **10.1016/j.ijbiomac.2023.124238**

66. Veronovski, A.; Novak, Z.; Knez, Ž., Synthesis and Use of Organic Biodegradable Aerogels as Drug Carriers. *Journal of Biomaterials Science, Polymer Edition* **2012,** *23* (7), 873-886. **10.1163/092050611X566126**

67. García-González, C. A.; Sosnik, A.; Kalmár, J.; De Marco, I.; Erkey, C.; Concheiro, A.; Alvarez-Lorenzo, C., Aerogels in drug delivery: From design to application. *Journal of Controlled Release* **2021,** *332*, 40-63. **10.1016/j.jconrel.2021.02.012**

68. Groult, S.; Buwalda, S.; Budtova, T., Tuning bio-aerogel properties. Part 3: Exploring silica-pectin composite aerogels for drug delivery. *Biomaterials Advances* **2024,** *163*, 213954. **10.1016/j.bioadv.2024.213954**

69. Lohmann, H.; Grass, G.; Rangger, C.; Mathiak, G., Economic impact of cancellous bone grafting in trauma surgery. *Archives of Orthopaedic and Trauma Surgery* **2007,** *127* (5), 345-348. **10.1007/s00402-006-0277-4**

70. Sakkas, A.; Wilde, F.; Heufelder, M.; Winter, K.; Schramm, A., Autogenous bone grafts in oral implantology—is it still a "gold standard"? A consecutive review of 279 patients with 456 clinical procedures. *International Journal of Implant Dentistry* **2017,** *3* (1), 23. **10.1186/s40729-017-0084-4**

71. Chen, P.-Y.; McKittrick, J.; Meyers, M. A., Biological materials: Functional adaptations and bioinspired designs. *Progress in Materials Science* **2012,** *57* (8), 1492-1704. **10.1016/j.pmatsci.2012.03.001**

72. Qu, H.; Fu, H.; Han, Z.; Sun, Y., Biomaterials for bone tissue engineering scaffolds: a review. *RSC Advances* **2019,** *9* (45), 26252-26262. **10.1039/C9RA05214C**

73. Lázár, I.; Čelko, L.; Menelaou, M., Aerogel-Based Materials in Bone and Cartilage Tissue Engineering—A Review with Future Implications. *Gels* **2023,** *9* (9), 746. **10.3390/gels9090746**

74. Győri, E.; Fábián, I.; Lázár, I., Effect of the Chemical Composition of Simulated Body Fluids on Aerogel-Based Bioactive Composites. *Journal of Composites Science* **2017,** *1* (2), 15. **10.3390/jcs1020015**

75. Hegedűs, C.; Czibulya, Z.; Tóth, F.; Dezső, B.; Hegedűs, V.; Boda, R.; Horváth, D.; Csík, A.; Fábián, I.; Tóth-Győri, E.; Sajtos, Z.; Lázár, I., The Effect of Heat Treatment of β-Tricalcium Phosphate-Containing Silica-Based Bioactive Aerogels on the Cellular Metabolism and Proliferation of MG63 Cells. *Biomedicines* **2022,** *10* (3), 662. **10.3390/biomedicines10030662**

76. Hegedűs, V.; Kerényi, F.; Boda, R.; Horváth, D.; Lázár, I.; Tóth-Győri, E.; Dezső, B.; Hegedus, C., β-Tricalcium phosphate-silica aerogel as an alternative bioactive ceramic for the potential use in dentistry. *Advances in Applied Ceramics* **2020,** *119* (5-6), 364-371. **10.1080/17436753.2019.1625567**

77. Kuttor, A.; Szalóki, M.; Rente, T.; Kerényi, F.; Bakó, J.; Fábián, I.; Lázár, I.; Jenei, A.; Hegedüs, C., Preparation and application of highly porous aerogel-based bioactive materials in dentistry. *Frontiers of Materials Science* **2014,** *8* (1), 46-52. **10.1007/s11706-014-0231-2**

78. Lázár, I.; Bereczki, H. F.; Manó, S.; Daróczi, L.; Deák, G.; Fábián, I.; Csernátony, Z., Synthesis and study of new functionalized silica aerogel poly(methyl methacrylate) composites for biomedical use. *Polymer Composites* **2015,** *36* (2), 348-358. **10.1002/pc.22949**

79. Allo, B. A.; Costa, D. O.; Dixon, S. J.; Mequanint, K.; Rizkalla, A. S. Bioactive and Biodegradable Nanocomposites and Hybrid Biomaterials for Bone Regeneration *Journal of Functional Biomaterials* [Online], 2012, p. 432-463. **10.3390/jfb3020432**

80. Dorozhkin, S. V. Calcium Orthophosphate-Containing Biocomposites and Hybrid Biomaterials for Biomedical Applications *Journal of Functional Biomaterials* [Online], 2015, p. 708-832. **10.3390/jfb6030708**

81. Behravesh, E.; Yasko, A. W.; Engel, P. S.; Mikos, A. G., Synthetic Biodegradable Polymers for Orthopaedic Applications. *Clinical Orthopaedics and Related Research (1976-2007)* **1999,** *367*. **10.1097/00003086-199910001-00012**

82. Boyan, B. D.; Lohmann, C. H.; Somers, A.; Niederauer, G. G.; Wozney, J. M.; Dean, D. D.; Carnes Jr, D. L.; Schwartz, Z., Potential of porous poly-D,L-lactide-co-glycolide particles as a carrier for recombinant human bone morphogenetic protein-2 during osteoinduction in vivo. *Journal of Biomedical Materials Research* **1999,** *46* (1), 51-59. **10.1002/(SICI)1097-4636(199907)46:1<51::AID-JBM6>3.0.CO;2-I**

83. Petricca, S. E.; Marra, K. G.; Kumta, P. N., Chemical synthesis of poly(lactic-co-glycolic acid)/hydroxyapatite composites for orthopaedic applications. *Acta Biomaterialia* **2006,** *2* (3), 277-286. **10.1016/j.actbio.2005.12.004**

84. Athanasiou, K. A.; Schmitz, J. P.; Agrawal, C. M., The Effects of Porosity on in Vitro Degradation of Polylactic Acid–Polyglycolic Acid Implants Used in Repair of Articular Cartilage. *Tissue Engineering* **1998,** *4* (1), 53-63. **10.1089/ten.1998.4.53**

85. Husain, M. S. B.; Gupta, A.; Alashwal, B. Y.; Sharma, S., Synthesis of PVA/PVP based hydrogel for biomedical applications: a review. *Energy Sources, Part A: Recovery, Utilization, and Environmental Effects* **2018,** *40* (20), 2388-2393. **10.1080/15567036.2018.1495786**

86. Kumar, A.; Han, S. S., PVA-based hydrogels for tissue engineering: A review. *International Journal of Polymeric Materials and Polymeric Biomaterials* **2017,** *66* (4), 159-182. **10.1080/00914037.2016.1190930**

87. Muppalaneni, S.; Omidian, H., Polyvinyl alcohol in medicine and pharmacy: a perspective. *Journal of Developing Drugs* **2013,** *2* (3), 1-5. **10.4172/2329-6631.1000112**

88. Balasubramanian, P.; Grünewald, A.; Detsch, R.; Hupa, L.; Jokic, B.; Tallia, F.; Solanki, A. K.; Jones, J. R.; Boccaccini, A. R., Ion Release, Hydroxyapatite Conversion, and Cytotoxicity of Boron-Containing Bioactive Glass Scaffolds. *International Journal of Applied Glass Science* **2016,** *7* (2), 206-215. **10.1111/ijag.12206**

89. Coelho, S. A. R.; Almeida, J. C.; Unalan, I.; Detsch, R.; Miranda Salvado, I. M.; Boccaccini, A. R.; Fernandes, M. H. V., Cellular Response to Sol–Gel Hybrid Materials Releasing Boron and Calcium Ions. *ACS Biomaterials Science & Engineering* **2021,** *7* (2), 491-506. **10.1021/acsbiomaterials.0c01546**

90. Balogh, Z.; Len, A.; Baksa, V.; Krajnc, A.; Herman, P.; Szemán-Nagy, G.; Czigány, Z.; Fábián, I.; Kalmár, J.; Dudás, Z., Nanoscale Structural Characteristics and In Vitro Bioactivity of Borosilicate–Poly(vinyl alcohol) (PVA) Hybrid Aerogels for Bone Regeneration. *ACS Applied Nano Materials* **2024,** *7* (4), 4092-4102. **10.1021/acsanm.3c05668**

91. Gommes, C. J.; Goderis, B.; Pirard, J.-P.; Blacher, S., Branching, aggregation, and phase separation during the gelation of tetraethoxysilane. *Journal of Non-Crystalline Solids* **2007,** *353* (24), 2495-2499. **10.1016/j.jnoncrysol.2007.04.009**

92. Gommes, C. J.; Roberts, A. P., Structure development of resorcinol-formaldehyde gels: Microphase separation or colloid aggregation. *Physical Review E* **2008,** *77* (4), 041409. **10.1103/PhysRevE.77.041409**

93. Sivia, D. S., *Elementary scattering theory: for X-ray and neutron users*. Oxford University Press: **2011**.

94. Gommes, C. J.; Jaksch, S.; Frielinghaus, H., Small-angle scattering for beginners. *Journal of Applied Crystallography* **2021,** *54* (6), 1832-1843. **10.1107/S1600576721010293**

95. Glatter, O., *Scattering methods and their application in colloid and interface science*. Elsevier: **2018**.

96. Emmerling, A.; Fricke, J., Small angle scattering and the structure of aerogels. *Journal of Non-Crystalline Solids* **1992,** *145*, 113-120. **10.1016/S0022-3093(05)80439-9**

97. Pedersen, J. S., Analysis of small-angle scattering data from colloids and polymer solutions: modeling and least-squares fitting. *Advances in Colloid and Interface Science* **1997,** *70*, 171-210. **10.1016/S0001-8686(97)00312-6**

98. Debye, P.; Anderson, H. R., Jr.; Brumberger, H., Scattering by an Inhomogeneous Solid. II. The Correlation Function and Its Application. *Journal of Applied Physics* **1957,** *28* (6), 679-683. **10.1063/1.1722830**

99. Debye, P.; Bueche, A. M., Scattering by an Inhomogeneous Solid. *Journal of Applied Physics* **1949,** *20* (6), 518-525. **10.1063/1.1698419**

100. Beaucage, G., Approximations Leading to a Unified Exponential/Power-Law Approach to Small-Angle Scattering. *Journal of Applied Crystallography* **1995,** *28* (6), 717-728. **10.1107/S0021889895005292**

101. Beaucage, G., Small-Angle Scattering from Polymeric Mass Fractals of Arbitrary Mass-Fractal Dimension. *Journal of Applied Crystallography* **1996,** *29* (2), 134-146. **10.1107/S0021889895011605**

102. Tilgner, I. C.; Fischer, P.; Bohnen, F. M.; Rehage, H.; Maier, W. F., Effect of acidic, basic and fluoride-catalyzed sol-gel transitions on the preparation of sub-nanostructured silica. *Microporous Materials* **1995,** *5* (1), 77-90. **10.1016/0927-6513(95)00045-B**

103. Socrates, G., *Infrared and Raman characteristic group frequencies: tables and charts*. John Wiley & Sons: **2004**.

104. Reif, B.; Ashbrook, S. E.; Emsley, L.; Hong, M., Solid-state NMR spectroscopy. *Nature Reviews Methods Primers* **2021,** *1* (1), 2. **10.1038/s43586-020-00002-1**

105. Thommes, M.; Kaneko, K.; Neimark, A. V.; Olivier, J. P.; Rodriguez-Reinoso, F.; Rouquerol, J.; Sing, K. S. W., Physisorption of gases, with special reference to the evaluation of surface area and pore size distribution (IUPAC Technical Report). **2015,** *87* (9-10), 1051-1069. **10.1515/pac-2014-1117**

106. Juhász, L.; Moldován, K.; Gurikov, P.; Liebner, F.; Fábián, I.; Kalmár, J.; Cserháti, C., False Morphology of Aerogels Caused by Gold Coating for SEM Imaging. *Polymers* **2021,** *13* (4), 588. **10.3390/polym13040588**

107. Almásy, L., New Measurement Control Software on the Yellow Submarine SANS Instrument at the Budapest Neutron Centre. *Journal of Surface Investigation: X-ray, Synchrotron and Neutron Techniques* **2021,** *15* (3), 527-531. **10.1134/S1027451021030046**

108. Keiderling, U., The new 'BerSANS-PC' software for reduction and treatment of small angle neutron scattering data. *Applied Physics A* **2002,** *74* (1), s1455-s1457. **10.1007/s003390201561**

109. Al-Oweini, R.; El-Rassy, H., Synthesis and characterization by FTIR spectroscopy of silica aerogels prepared using several Si(OR)4 and R″Si(OR′)3 precursors. *Journal of Molecular Structure* **2009,** *919* (1), 140-145. **10.1016/j.molstruc.2008.08.025**

110. Mansur, H. S.; Sadahira, C. M.; Souza, A. N.; Mansur, A. A. P., FTIR spectroscopy characterization of poly (vinyl alcohol) hydrogel with different hydrolysis degree and chemically crosslinked with glutaraldehyde. *Materials Science and Engineering: C* **2008,** *28* (4), 539-548. **10.1016/j.msec.2007.10.088**

111. Shao, G.; Wu, X.; Kong, Y.; Cui, S.; Shen, X.; Jiao, C.; Jiao, J., Thermal shock behavior and infrared radiation property of integrative insulations consisting of MoSi2/borosilicate glass coating and fibrous ZrO2 ceramic substrate. *Surface and Coatings Technology* **2015,** *270*, 154-163. **10.1016/j.surfcoat.2015.03.008**

112. Wan, J.; Cheng, J.; Lu, P., The coordination state of B and Al of borosilicate glass by IR spectra. *Journal of Wuhan University of Technology-Mater. Sci. Ed.* **2008,** *23* (3), 419-421. **10.1007/s11595-007-3419-9**

113. Lim, M.; Kwon, H.; Kim, D.; Seo, J.; Han, H.; Khan, S. B., Highly-enhanced water resistant and oxygen barrier properties of cross-linked poly(vinyl alcohol) hybrid films for packaging applications. *Progress in Organic Coatings* **2015,** *85*, 68-75. **10.1016/j.porgcoat.2015.03.005**

114. Park, K.; Oh, Y.; Panda, P. K.; Seo, J., Effects of an acidic catalyst on the barrier and water resistance properties of crosslinked poly (vinyl alcohol) and boric acid films. *Progress in Organic Coatings* **2022,** *173*, 107186. **10.1016/j.porgcoat.2022.107186**

115. Sorarù, G. D.; Dallabona, N.; Gervais, C.; Babonneau, F., Organically Modified SiO2−B2O3 Gels Displaying a High Content of Borosiloxane (B−O−Si:) Bonds. *Chemistry of Materials* **1999,** *11* (4), 910-919. **10.1021/cm980353l**

116. Tadokoro, H., Infrared Studies of Polyvinyl Alcohol by Deuteration of its OH Groups. *Bulletin of the Chemical Society of Japan* **2006,** *32* (11), 1252-1257. **10.1246/bcsj.32.1252**

117. Chang, M. C.; Tanaka, J., FT-IR study for hydroxyapatite/collagen nanocomposite cross-linked by glutaraldehyde. *Biomaterials* **2002,** *23* (24), 4811-4818. **10.1016/S0142-9612(02)00232-6**

118. Wu, C.-C.; Huang, S.-T.; Tseng, T.-W.; Rao, Q.-L.; Lin, H.-C., FT-IR and XRD investigations on sintered fluoridated hydroxyapatite composites. *Journal of Molecular Structure* **2010,** *979* (1), 72-76. **10.1016/j.molstruc.2010.06.003**

119. El Rassy, H.; Pierre, A. C., NMR and IR spectroscopy of silica aerogels with different hydrophobic characteristics. *Journal of Non-Crystalline Solids* **2005,** *351* (19), 1603-1610. **10.1016/j.jnoncrysol.2005.03.048**

120. Sato, Y.; Hayami, R.; Gunji, T., Characterization of NMR, IR, and Raman spectra for siloxanes and silsesquioxanes: a mini review. *Journal of Sol-Gel Science and Technology* **2022,** *104* (1), 36-52. **10.1007/s10971-022-05920-y**

121. Du, L.-S.; Stebbins, J. F., Site Preference and Si/B Mixing in Mixed-Alkali Borosilicate Glasses: A High-Resolution 11B and 17O NMR Study. *Chemistry of Materials* **2003,** *15* (20), 3913-3921. **10.1021/cm034427r**

122. van Wüllen, L.; Müller-Warmuth, W.; Papageorgiou, D.; Pentinghaus, H. J., Characterization and structural developments of gel-derived borosilicate glasses: a multinuclear MAS-NMR study. *Journal of Non-Crystalline Solids* **1994,** *171* (1), 53-67. **10.1016/0022-3093(94)90032-9**

123. Wu, J.; Stebbins, J. F., Cation Field Strength Effects on Boron Coordination in Binary Borate Glasses. *Journal of the American Ceramic Society* **2014,** *97* (9), 2794-2801. **10.1111/jace.13100**

124. Sinton, S. W., Complexation chemistry of sodium borate with poly(vinyl alcohol) and small diols: a boron-11 NMR study. *Macromolecules* **1987,** *20* (10), 2430-2441. **10.1021/ma00176a018**

125. Grandjean, A.; Malki, M.; Montouillout, V.; Debruycker, F.; Massiot, D., Electrical conductivity and 11B NMR studies of sodium borosilicate glasses. *Journal of Non-Crystalline Solids* **2008,** *354* (15), 1664-1670. **10.1016/j.jnoncrysol.2007.10.007**

126. Irwin, A. D.; Holmgren, J. S.; Jonas, J., Solid state 29Si and 11B NMR studies of sol-gel derived borosilicates. *Journal of Non-Crystalline Solids* **1988,** *101* (2), 249-254. **10.1016/0022-3093(88)90160-3**

127. Irwin, A. D.; Holmgren, J. S.; Zerda, T. W.; Jonas, J., Spectroscopic investigations of borosiloxane bond formation in the sol-gel process. *Journal of Non-Crystalline Solids* **1987,** *89* (1), 191-205. **10.1016/S0022-3093(87)80332-0**

128. Korbag, I.; Mohamed Saleh, S., Studies on the formation of intermolecular interactions and structural characterization of polyvinyl alcohol/lignin film. *International Journal of Environmental Studies* **2016,** *73* (2), 226-235. **10.1080/00207233.2016.1143700**

129. Jäger, C.; Welzel, T.; Meyer-Zaika, W.; Epple, M., A solid-state NMR investigation of the structure of nanocrystalline hydroxyapatite. *Magnetic Resonance in Chemistry* **2006,** *44* (6), 573-580. **10.1002/mrc.1774**

130. Lázár, I.; Forgács, A.; Horváth, A.; Király, G.; Nagy, G.; Len, A.; Dudás, Z.; Papp, V.; Balogh, Z.; Moldován, K.; Juhász, L.; Cserháti, C.; Szántó, Z.; Fábián, I.; Kalmár, J., Mechanism of hydration of biocompatible silica-casein aerogels probed by NMR and SANS reveal backbone rigidity. *Applied Surface Science* **2020,** *531*, 147232. **10.1016/j.apsusc.2020.147232**

131. Niculescu, A.-G.; Tudorache, D.-I.; Bocioagă, M.; Mihaiescu, D. E.; Hadibarata, T.; Grumezescu, A. M., An Updated Overview of Silica Aerogel-Based Nanomaterials. *Nanomaterials* **2024,** *14* (5). **10.3390/nano14050469**

132. Porod, G., Die Röntgenkleinwinkelstreuung von dichtgepackten kolloiden Systemen. *Kolloid-Zeitschrift* **1952,** *125* (1), 51-57. **10.1007/BF01519615**

133. Ecsédi, B.; Forgács, A.; Balogh, Z.; Fábián, I.; Kalmár, J., Hydration and wetting mechanism of borosilicate – Polyvinyl alcohol (PVA) hybrid aerogels of potential bioactivity. *Journal of Molecular Liquids* **2024,** *401*, 124605. **10.1016/j.molliq.2024.124605**

134. Ludescher, L.; Morak, R.; Balzer, C.; Waag, A. M.; Braxmeier, S.; Putz, F.; Busch, S.; Gor, G. Y.; Neimark, A. V.; Hüsing, N.; Reichenauer, G.; Paris, O., In Situ Small-Angle Neutron Scattering Investigation of Adsorption-Induced Deformation in Silica with Hierarchical Porosity. *Langmuir* **2019,** *35* (35), 11590-11600. **10.1021/acs.langmuir.9b01375**

135. Morak, R.; Braxmeier, S.; Ludescher, L.; Putz, F.; Busch, S.; Husing, N.; Reichenauer, G.; Paris, O., Quantifying adsorption-induced deformation of nanoporous materials on different length scales. *Journal of Applied Crystallography* **2017,** *50* (5), 1404-1410. **10.1107/S1600576717012274**

136. Liu, D.; Song, K.; Chen, W.; Chen, J.; Sun, G.; Li, L., Review: Current progresses of small-angle neutron scattering on soft-matters investigation. *Nuclear Analysis* **2022,** *1* (2), 100011. **10.1016/j.nucana.2022.100011**

137. Merzbacher, C. I.; Barker, J. G.; Swider, K. E.; Ryan, J. V.; Bernstein, R. A.; Rolison, D. R., Characterization of multi-phase aerogels by contrast-matching SANS. *Journal of Non-Crystalline Solids* **1998,** *225*, 234-238. **10.1016/S0022-3093(98)00044-1**

138. Kienzle, P. Neutron activation and scattering calculator. 2020. https://www.ncnr.nist.gov/resources/activation/

139. Shelby, J. E., *Introduction to glass science and technology*. Royal society of chemistry: **2020**.

140. Sears, V. F., Neutron scattering lengths and cross sections. *Neutron News* **1992,** *3* (3), 26-37. **10.1080/10448639208218770**

141. Moldován, K.; Forgács, A.; Paul, G.; Marchese, L.; Len, A.; Dudás, Z.; Kéki, S.; Fábián, I.; Kalmár, J., Mechanism of Hydration Induced Stiffening and Subsequent Plasticization of Polyamide Aerogel. *Advanced Materials Interfaces* **2023,** *10* (17), 2300109. **10.1002/admi.202300109**

142. Rege, A.; Ratke, L.; Külcü, İ. D.; Gurikov, P., Stiffening of biopolymer aerogel networks upon wetting: A model-based study. *Journal of Non-Crystalline Solids* **2020,** *531*, 119859. **10.1016/j.jnoncrysol.2019.119859**

143. Santos-Rosales, V.; Alvarez-Rivera, G.; Hillgärtner, M.; Cifuentes, A.; Itskov, M.; García-González, C. A.; Rege, A., Stability Studies of Starch Aerogel Formulations for Biomedical Applications. *Biomacromolecules* **2020,** *21* (12), 5336-5344. **10.1021/acs.biomac.0c01414**

144. Raman, S. P.; Keil, C.; Dieringer, P.; Hübner, C.; Bueno, A.; Gurikov, P.; Nissen, J.; Holtkamp, M.; Karst, U.; Haase, H.; Smirnova, I., Alginate aerogels carrying calcium, zinc and silver cations for wound care: Fabrication and metal detection. *The Journal of Supercritical Fluids* **2019,** *153*, 104545. **10.1016/j.supflu.2019.104545**

145. Zhang, X.; Wang, X.; Fan, W.; Liu, Y.; Wang, Q.; Weng, L., Fabrication, Property and Application of Calcium Alginate Fiber: A Review. *Polymers* **2022,** *14* (15). **10.3390/polym14153227**

146. Balogh, Z.; Kalmar, J.; Gommes, C. J., Wetting of alginate aerogels, from mesoporous solids to hydrogels: a small-angle scattering analysis. *Journal of Applied Crystallography* **2024,** *57* (2), 369-379. **10.1107/S1600576724001705**

147. Depta, P. N.; Gurikov, P.; Schroeter, B.; Forgács, A.; Kalmár, J.; Paul, G.; Marchese, L.; Heinrich, S.; Dosta, M., DEM-Based Approach for the Modeling of Gelation and Its Application to Alginate. *Journal of Chemical Information and Modeling* **2022,** *62* (1), 49-70. **10.1021/acs.jcim.1c01076**

148. Burchard, W., Particle Scattering Factors of Some Branched Polymers. *Macromolecules* **1977,** *10*, 919-927. **10.1021/MA60059A008**

149. Shibayama, M., Small-angle neutron scattering on polymer gels: phase behavior, inhomogeneities and deformation mechanisms. *Polymer Journal* **2011,** *43* (1), 18-34. **10.1038/pj.2010.110**

150. Wei, Y.; Hore, M. J. A., Characterizing polymer structure with small-angle neutron scattering: A Tutorial. *Journal of Applied Physics* **2021,** *129* (17), 171101. **10.1063/5.0045841**

151. Gommes, C. J.; Prieto, G.; de Jongh, P. E., Small-Angle Scattering Analysis of Empty or Loaded Hierarchical Porous Materials. *The Journal of Physical Chemistry C* **2016,** *120* (3), 1488-1506. **10.1021/acs.jpcc.5b09556**

152. Feigin, L.; Svergun, D. I., *Structure analysis by small-angle X-ray and neutron scattering*. Springer: **1987**; Vol. 1.

153. Ohser, J.; Mücklich, F., *Statistical analysis of microstructures in materials science*. John Wiley & Sons: **2000**.

154. Serra, J., *Image analysis and mathematical morphology*. Academic Press, Inc.: **1983**.

155. Jeulin, D., *Morphological models of random structures*. Springer: **2021**.

156. Torquato, S.; Haslach Jr, H. W., Random heterogeneous materials: microstructure and macroscopic properties. *Appl. Mech. Rev.* **2002,** *55* (4), B62-B63.

157. Hammouda, B., Probing Nanoscale Structures - The SANS Toolbox. 2012.

158. Lantuéjoul, C., *Geostatistical simulation: models and algorithms*. Springer Science & Business Media: **2013**.

159. Gille, W., Scattering properties and structure functions of Boolean models. *Computers & Structures* **2011,** *89* (23), 2309-2315. **10.1016/j.compstruc.2011.08.004**

160. Gommes, C. J., Stochastic models of disordered mesoporous materials for small-angle scattering analysis and more. *Microporous and Mesoporous Materials* **2018,** *257*, 62-78. **10.1016/j.micromeso.2017.08.009**

161. Sorbier, L.; Moreaud, M.; Humbert, S., Small-angle X-ray scattering intensity of multiscale models of spheres. *Journal of Applied Crystallography* **2019,** *52* (6), 1348-1357. **10.1107/S1600576719013839**

162. Lighthill, M. J., *An introduction to Fourier analysis and generalised functions*. Cambridge University Press: **1958**.

163. Teixeira, J., Small-angle scattering by fractal systems. *Journal of Applied Crystallography* **1988,** *21* (6), 781-785. **10.1107/S0021889888000263**

164. Banerjee, A.; De, R.; Das, B., Hydrodynamic and conformational characterization of aqueous sodium alginate solutions with varying salinity. *Carbohydrate Polymers* **2022,** *277*, 118855. **10.1016/j.carbpol.2021.118855**

165. Ciccariello, S.; Goodisman, J.; Brumberger, H., On the Porod law. *Journal of Applied Crystallography* **1988,** *21* (2), 117-128. **10.1107/S0021889887010409**

166. Gommes, C. J.; Jiao, Y.; Roberts, A. P.; Jeulin, D., Chord-length distributions cannot generally be obtained from small-angle scattering. *Journal of Applied Crystallography* **2020,** *53* (1), 127-132. **10.1107/S1600576719016133**

167. Dirac, P., Approximate rate of neutron multiplication for a solid of arbitrary shape and uniform density. *Declassified British Report MS-D-5, Part I* **1943**.

168. Sjöstrand, N. G., What is the average chord length? *Annals of Nuclear Energy* **2002,** *29* (13), 1607-1608. **10.1016/S0306-4549(02)00003-8**

169. Külcü, İ. D.; Rege, A., Physics-informed constitutive modelling of hydrated biopolymer aerogel networks. *Soft Matter* **2021,** *17* (21), 5278-5283. **10.1039/D1SM00430A**

11. Publications and conferences

International publications related to the dissertation

I. Balogh, Z., Len, A., Baksa, V., Krajnc, A., Herman, P., Szemán-Nagy, G., Czigány, Zs., Fábián, I., Kalmár, J., Dudás, Z.
Nanoscale structural characteristics and in vitro bioactivity of borosilicate – polyvinyl alcohol (PVA) hybrid aerogels for bone regeneration
ACS Applied Nano Materials, 7(4), 4092-4102. (2024)
IF (2023): 5.3 (Q1)

II. Balogh, Z., Kalmár, J., Gommes, C. J.
Wetting of alginate aerogels, from mesoporous solids to hydrogels: a small-angle scattering analysis
Journal of Applied Crystallography, 57(2), 369-379. (2024)
IF (2023): 5.2 (Q1)

III. Ecsédi, B., Forgács, A., Balogh, Z., Fábián, I., Kalmár, J.
Hydration and wetting mechanism of borosilicate–Polyvinyl alcohol (PVA) hybrid aerogels of potential bioactivity
Journal of Molecular Liquids, 401, 124605. (2024)
IF (2023): 5.3 (Q1)

Other international publications

I. Herman, P., Moldován, K., Paul, G., Marchese, L., Balogh, Z., Len, A., Dudás, Z., Fábián, I., Kalmár, J.
Selective and reversible surface complexation of aqueous palladium (II) by polycarboxylate (pyromellitic acid) functionalized hybrid aerogel sorbent
Applied Surface Science, 613, 156026. (2023)
IF (2023): 6.3 (Q1)

II. Lihi, N., Balogh Z., Diószegi R., Forgács A., Moldován K., May V. N., Herman P., Fábián I., Kalmár J.
Functionalizing Aerogels with Tetraazamacrocyclic Copper (II) Complexes: Nanoenzymes with Superoxide Dismutase Activity
Applied Surface Science, 611, 155622. (2023)

IF (2023): 6.3 (Q1)

III. Forgács, A., Balogh, Z., Andrási, M., Len, A., Dudás, Z., May, N. V., Herman, P., Juhász, L., Fábián, I., Lihi, N., Kalmár, J.
Mechanistic explanation for differences between catalytic activities of dissolved and aerogel immobilized Cu (II) cyclen
Applied Surface Science, 579, 152210. (2022)
IF (2022): 6.7 (Q1)

IV. Lázár, I., Forgács, A., Horváth, A., Király, G., Nagy, G., Len, A., Dudás, Z., Papp, V., Balogh, Z., Moldován, K., Juhász, L., Cserháti, Cs., Szántó, Zs., Fábián, I., Kalmár, J.
Mechanism of hydration of biocompatible silica-casein aerogels probed by NMR and SANS reveal backbone rigidity
Applied Surface Science, 531, 147232. (2020)
IF (2020): 6.707 (D1)

Hungarian conference publication

I. Balogh, Z., Lázár, I., Kalmár, J., Fábián, I., Forgács, A.
Cu(II)-ciklén tartalmú aerogél katalizátor hatásmechanizmusa
I. FKF Szimpózium: Fiatal Kémikusok Fóruma (2019)

Conference lecture presentations related to the dissertation

I. Balogh, Z., Kalmár, J., Gommes, C. J.
Wetting of alginate aerogels, from mesoporous solids to hydrogels: a small-angle scattering analysis
2nd International Seminar on Modelling, Simulation and Machine Learning for the Rapid Development of Porous Materials Workshop
4-6. March 2024., Madrid, Spain

II. Balogh, Z., Kalmár J., Gommes C. J.
Ca(II)-alginát aerogél nedvesedési mechanizmusának tanulmányozása kisszögű neutronszórás alkalmazásával
Hatvani István Szakkollégium 2023. Őszi Tudományos Hallgatói Konferencia
1. December 2023., Debrecen, Hungary

III. Balogh, Z., Kalmár, J., Gommes C. J.
Egy tipikus kalcium-alginát aerogél nedvesedésének mechanizmusa kisszögű neutronszórás (SANS) mérések alapján
MTA Kolloidkémiai Munkabizottság Őszi ülése
30. October 2023., Budapest, Hungary

IV. Balogh, Z., Len, A., Kalmár, J., Dudás, Z.
Funkcionalizált és hibrid aerogélek kisszögű neutronszórásos (SANS) vizsgálata
Hatvani István Szakkollégium 2022. Őszi Tudományos Hallgatói Konferencia
8. December 2022., Debrecen, Hungary

V. Balogh, Z., Baksa, V., Len, A., Szemán-Nagy, G., Moldován, K., Herman, P., Fábián, I., Kalmár, J., Dudás, Z.
Synthesis and structural investigation of borosilicate-PVA hybrid aerogels for bone regeneration application
Budapest Neutron Centre seminar
24. November 2022., Budapest, Hungary

VI. Balogh, Z., Kalmár, J., Dudás, Z.
Csontpótlásra potenciálisan alkalmas boroszilikát aerogélek előállítása és szerkezeti vizsgálata
Hatvani István Szakkollégium 2022. Tavaszi Tudományos Hallgatói Konferencia
6. May 2022., Debrecen, Hungary

VII. Balogh, Z., Veres, E., Moldován, K., Baksa, V., Szemán-Nagy, G., Fábián, I., Len, A., Dudás, Z., Kalmár, J.
Boroszilikát aerogélek mint potenciális csontpótló anyagok
II. Fiatal Kémikusok Fóruma Szimpózium
16-18. June 2021., Online

Conference poster presentation related to the dissertation

I. Balogh, Z., Dudás , Z., Kalmár, J., Len, A.
Small angle neutron scattering (SANS) investigation of functionalized and hybrid silica aerogels
Workshop on Aerogels Characterization and Modelling
29-31. March 2023., Debrecen, Hungary